Alma Mater Studiorum
Università degli Studi di Bologna

Facoltà di Scienze Matematiche Fisiche e Naturali
Dottorato di Ricerca in Fisica, **XVII** Ciclo

Study of electron identification in the Emulsion Cloud Chambers of the OPERA experiment

Luigi Salvatore Esposito

Advisors:
Prof. **Giorgio Giacomelli**
Dr. **Gianni Mandrioli**
Dr. **Maximiliano Sioli**

PhD Coordinator:
Prof. **Roberto Soldati**

Bologna, 2005

Contents

Introduction

Neutrino physics is one of the most challenging topics in particle physics. There is convincing evidence for neutrino oscillations, hence neutrino masses and mixing, in particular the combined analysis of atmospheric neutrino experiments favors the hypothesis that the oscillation is purely $\nu_\mu \rightarrow \nu_\tau$.

The final proof for neutrino oscillations should be the detection of a ν_τ in a terrestrial artificial (almost) pure ν_μ beam (appearance experiment). The distinctive feature of charged current (CC) ν_τ interactions is the decay of the short-lived τ lepton with a "kink" or a "multiprong" topology at sub-millimeter distance from the primary interaction.

The OPERA experiment, in preparation at the Gran Sasso Underground Laboratory, aims at the direct observation of $\nu_\mu \rightarrow \nu_\tau$ oscillations in the CNGS (**C**ERN **N**eutrinos to **G**ran **S**asso) neutrino beam produced at CERN. Since the ν_e contamination in the CNGS beam is low, OPERA will also be able to study the sub-dominant $\nu_\mu \rightarrow \nu_e$ oscillation channel.

OPERA is a large scale *hybrid* apparatus divided in two supermodules, each equipped with electronic detectors, an iron spectrometer and a highly segmented 0.9 kton target section made of "Emulsion Cloud Chamber" (ECC) units. Each emulsion-lead unit, called *brick*, is composed of alternate nuclear emulsion films and Pb sheets. The production and the decay of the τ lepton is observed thanks to the excellent position resolution of nuclear emulsions (the highest spatial resolution tracking detector). The use of the ECC satisfies the need of a large mass, required in long-baseline neutrino experiments, and a high precision tracking capability to detect τ decays. The target trackers and the spectrometers provide the trigger and a "prediction" of the individual brick where the neutrino interaction happened. The candidate brick is then extracted and disassembled. The emulsion films are photographically processed and then scanned with automatic microscopes for an event-by-event topological classification (event location, search for decays)

and further measurements (particle identification and momentum measurement).

Very fast automatic scanning systems are needed to cope with the analysis of the large number of emulsion sheets associated to neutrino interactions. The development of a new scanning system has been carried out by two different R&D programs, in Japan and in Europe, where several groups have been working together for the development of the *European Scanning System*.

Tau leptons can decay into a hadron, a muon or an electron. The electron channel has a characteristic signature due to the electromagnetic shower produced by the electron. Kinematic cuts are necessary to minimize the background.

It is important to develop an algorithm to identify the electrons and measure their energy. The electron-pion separation can be achieved studying the different behavior of these particles in passing through an OPERA brick. At the energies of our interest ($1 \div 10$ GeV), an electron generates an electromagnetic shower, while, a charged pion loses energy essentially through ionization.

An experimental study of electron identification using ECC was performed with an electron-enriched π^- beam [1]. The scanning of the ECC was performed using the Japanese system. This study is based on the multiple Coulomb scattering of the particle before any shower starts.

This thesis work has been carried out in the OPERA Bologna group and deals with the electron identification in the ECC and is based on the shower development inside the brick. Moreover, an electron-pion separator based on a Neural Network is implemented.

A new experimental study was performed at DESY where few bricks were exposed to a pure electron beam in order to study the electron identification in a cleaner environment. To complement the result of this analysis another test beam experiment was performed at CERN where some bricks were exposed to an essentially pure pion beam [2].

In this thesis I shall briefly discuss neutrino oscillations in the first Chapter and the OPERA experiment in the second Chapter. Nuclear emulsions and the automatic scanning system performances are the subjects of the third Chapter. The characteristics of electromagnetic showers in a OPERA brick, the test beam experiment in DESY and the Monte Carlo simulation are described in the fourth Chapter. In the last Chapter the analysis and the results of electron identification are presented.

Chapter 1

Neutrino oscillations

The existence of neutrinos was proposed by W. Pauli in 1930 as an attempt to explain the continuous spectrum of β-decay and the problem of spin and statistics of nuclei : *"... I have hit upon a desperate remedy to save the exchange theorem*[1] *of statistics and the law of conservation of energy. Namely, the possibility that there could exist in the nuclei electrically neutral particles, that I wish to call neutrons, which have spin 1/2 and obey the exclusion principle and which further differ from light quanta in that they do not travel with the velocity of light. The mass of the neutrons should be of the same order of magnitude as the electron mass and in any event not larger than 0.01 proton masses..."* [3].

In 1932 Chadwick discovered the neutron and solved the problem of spin and statistics of the nuclei; but neutrons are heavy and could not correspond to the particle imagined by Pauli. In 1933-34 Fermi introduced the name *neutrino* in his four-fermion theory of β-decay.

Until the end of the forties, physicists tried to measure the recoil of the nucleus during its β-decay. All the measurements were compatible with the hypothesis of only one neutrino emitted with the electron. It became clear that a very abundant source of neutrinos and a very sensitive and large detector were needed to detect the neutrinos.

The experimental discovery of the neutrino is due to Cowan and Reines in 1956 [4]; the experiment consisted in a target made of around 400 liters of a mixture of water and cadmium chloride: the electron anti-neutrinos coming

[1]That reads: exclusion principle (Fermi statistics) and half-integer spin for an odd number of particles; Bose statistics and integer spin for an even number of particles.

from the nuclear reactor interact with protons of the target matter, giving a positron and a neutron (inverse β-decay): $\bar{\nu}_e + \mathrm{p} \rightarrow \mathrm{n} + e^+$.

Following their experimental discovery, neutrinos were first shown to always have negative helicity (*i.e.* the spin and momentum are aligned in opposite directions) by measuring the helicity of gamma-rays produced in the radioactive decay of Europium-152.

Later it was established that there were two different types of neutrino, one associated with the electron and one with the muon. A muon neutrino beam was made using the $\pi \rightarrow \mu\nu_\mu$ decays. The ν_μ interacted in a target producing muons and not electrons $\nu_\mu + \mathrm{p} \rightarrow \mu^- + \mathrm{n}$[5].

These experiments, along with many others, have experimentally established that ν_e and ν_μ are the neutral partners of the electron and muon, respectively, and helped to shape our understanding of weak interactions in the Standard Model (SM).

In e^+e^- collisions at SLAC was later found evidence for a third type of lepton, τ^-, to which was associated a third neutrino ν_τ.

During the sixties and seventies, electron and muon neutrinos of high energy were used to probe the composition of nucleons. The experiments gave evidence for quarks and established their properties.

In 1970, Glashow, Illiopoulos and Maiani made the hypothesis of the existence of a second quark family, which should correspond to the second family of leptons; this hypothesis was confirmed by experiments at the end of 1974.

In 1973 neutral currents (neutrino interaction with matter where neutrino is not transformed into another particle like muon or electron) were discovered at CERN and confirmed at Fermilab.

In 1977 the b quark, that is one quark of the third quark family, was discovered at Fermilab, almost at the same time that Martin Perl discovered the τ lepton at SLAC. The corresponding neutrino ν_τ was finally observed experimentally only in 2001 at Fermilab by the DONUT experiment [6].

A complete knowledge of weak interactions came after the discoveries of the W and the Z bosons in 1983; in 1989 the study of the Z boson width allowed to show that only three lepton families (and then three types of neutrinos) exist [7].

Precision confirmations of the validity of the SM at low and high energy were experimentally given in the 90's at LEP [8]. Even so, the high energy physics community started turning toward the search for physics beyond the

SM, in particular for a non zero neutrino mass.

1.1 The mass of neutrinos

The SM of particle physics is a mathematical description of the strong and electroweak interactions. In the absence of any direct evidence for their mass, neutrinos were introduced in the SM as truly massless fermions for which no gauge invariant renormalizable mass term can be constructed. In other words, in the SM there is no right handed neutrino field ν_R but only a left handed neutrino field ν_L, which couples to the W and Z bosons. Consequently, in the SM there is neither mixing nor CP violation in the lepton sector. Experimental evidence for neutrino masses or mixing or leptonic CP violation would be a signal for new physics.

To accommodate the ν mass in the same manner as quark and charged lepton masses, we have to add a ν_R to the SM. Then we may construct the *Dirac mass term*

$$\mathcal{L}_D = -m_D \bar{\nu}_L \nu_R + \text{h.c.}, \tag{1.1}$$

in which m_D is a mass parameter. This term, similar to the mass terms of quarks and charged leptons, conserves the lepton number L that distinguishes neutrinos and negatively-charged leptons on the one hand from anti-neutrinos and positively-charged leptons on the other. Moreover, the SM interactions conserve the leptonic number for each family, L_e, L_μ and L_τ. Each neutrino mass eigenstate ν_i differs from its antiparticle $\bar{\nu}_i$, the difference being that $L(\bar{\nu}_i) = -L(\nu_i)$. When $\bar{\nu}_i \neq \nu_i$, the neutrino is said to be a *Dirac neutrino*.

Since the neutrino is electrically neutral, a left-handed *Majorana mass term* can be constructed from a chirally left-handed neutrino field ν_L alone

$$\mathcal{L}_{m_L} = -\frac{m_L}{2}\overline{(\nu_L)^c}\nu_L + \text{h.c.}\ . \tag{1.2}$$

Once ν_R has been added to the description of neutrinos, also the right-handed *Majorana mass term*

$$\mathcal{L}_{m_R} = -\frac{m_R}{2}\overline{(\nu_R)^c}\nu_R + \text{h.c.}, \tag{1.3}$$

can be constructed out of ν_R and its charge conjugate, ν_R^c. In these terms, m_L and m_R are other two mass parameters. Since both ν_R and $\bar{\nu}_R^c$ absorb

ν and create $\bar{\nu}$, $\mathcal{L}_M$ mixes ν and $\bar{\nu}$. An electrically charged fermion cannot have a Majorana mass term, because such a term would convert it into an anti-fermion, in violation of electric charge conservation. Thus, a Majorana mass term does not conserve L. There is then no conserved lepton number to distinguish a neutrino mass eigenstate ν_i from its antiparticle. Hence, when Majorana mass terms are present, $\nu_i = \bar{\nu}_i$. We then refer to ν_i as a *Majorana neutrino*.

In the laboratory, neutrino masses have been searched for in two types of experiments:

- direct kinematic searches of neutrino mass;
- neutrinoless double-β decay experiments.

The following upper bounds have been obtained from direct measurements of neutrino masses

$$m_{\nu_e} \leq 2.3 \text{ eV} \quad (95\% \ C.L.), \tag{1.4}$$
$$m_{\nu_\mu} \leq 170 \text{ keV} \quad (90\% \ C.L.), \tag{1.5}$$
$$m_{\nu_\tau} \leq 18.2 \text{ MeV} \quad (95\% \ C.L.). \tag{1.6}$$

The upper bound for the ν_e mass was obtained from the measurement of the high energy part of the β-spectrum from ^{3}H-decay [9]. The upper bound for the ν_μ mass comes from measurements of the muon momentum in the decay $\pi^+ \to \mu\nu_\mu$ [10] and the upper bound for the ν_τ mass from measurements of the distribution of effective mass of five pions in the decay $\tau \to \nu_\tau + 5\pi$ [11]. In principle, a kinematic neutrino mass measurement yields information about the different mass eigenstates m_{ν_i}, since it performs a projection onto energy and mass. Usually, however, the different neutrino mass eigenstates cannot be resolved by the experiments. Therefore an average over neutrino mass eigenstates is obtained, which is specific to the flavor of the weak decay considered, and hence one is allowed to use m_{ν_e}, m_{ν_μ}, m_{ν_τ}.

Constraint on neutrino masses has been recently obtained from the analysis of the cosmic microwave background anisotropy, combined with the galaxy redshift survey [12]

$$\sum_i m_{\nu_i} \leq 0.7 \text{ eV}. \tag{1.7}$$

The interactions of neutrinos are well described by the SM. If we neglect any non-SM L-violating interactions, then the only sources of L violation are the neutrino Majorana mass terms. The neutrinoless double-β decay ($0\nu\beta\beta$) is an L-violating decay. This is the process $(A, Z) \rightarrow (A, Z + 2) + 2e^-$, in which a nucleus containing A nucleons, Z of which are protons, decays to a nucleus containing $Z + 2$ protons by emitting two electrons. Observation of this reaction would show that the neutrinos were indeed Majorana particles.

The neutrino mass drives this reaction, so the L violation is going to be very small because of the smallness of the ν mass. It can be shown that the amplitude for $0\nu\beta\beta$ is proportional to the quantity

$$\left| \sum_i m_i U_{ei}^2 \right| \equiv |\langle m_{\beta\beta} \rangle| \,, \tag{1.8}$$

commonly referred to as the "effective Majorana mass for neutrinoless double beta decay" [13].

There are several experimental approaches for searching $0\nu\beta\beta$ decay. At present, the most sensitive experiment is the Heidelberg-Moscow experiment [14] that reported an upper limit on the effective neutrino mass

$$m_{ee} \leq 0.35 \text{ eV} \quad (90\% \; C.L.) \tag{1.9}$$

In December 2001, a subgroup of the Heidelberg-Moscow collaboration published evidence for a $0\nu\beta\beta$ decay signal. This signal corresponds to a mass $\langle m_{\beta\beta} \rangle = 0.39$ eV with a significance of 2-3σ [15].

In the next Paragraph, the compelling evidences of neutrino oscillations are reported. However, it is worth to mention that other exotic possibilities, such as neutrino decay [16], decoherence [17] or Lorentz invariance [18] are still possible, at least as sub-dominant mechanisms.

1.2 The physics of flavor change

If neutrinos have masses, in the 3 flavor neutrino oscillation framework, there are three neutrino mass eigenstates, ν_1, ν_2, ν_3, that are the analogues of the charged-lepton mass eigenstates, e, μ, and τ. If neutrinos mix, the neutrino state coupled by the charged-current interaction to the W boson and a specific charged lepton is a flavor eigenstates, ν_e, ν_μ, ν_τ. Thus, the neutrino

state created in weak interaction coupling the W boson to a charged lepton can be written as

$$|\nu_\alpha\rangle = \sum_{i=1}^{3} U^*_{\alpha i} |\nu_i\rangle \tag{1.10}$$

where α can be e, μ or τ. U is the unitary leptonic mixing matrix and is usually referred to as the Pontecorvo-Maki-Nakagawa-Sakata matrix (PMNS), in recognition of the pioneering contributions of these scientists to the physics of mixing and oscillations [19, 20].

In this Chapter, we shall sometimes refer also to sterile neutrinos. It is enough to say that sterile neutrinos are hypothetical particles that are like neutrinos but do not have ordinary weak interactions. They can be added to the theory as the right-handed neutrinos missing from the SM, or they can have a completely different origin [21].

To understand neutrino flavor change, let us consider how a neutrino born as the ν_α of Eq. 1.10 evolves in time. First, we apply Schrödinger's equation to the ν_i component of ν_α in the rest frame of that component. This tells us that

$$|\nu_i(\eta_i)\rangle = e^{-im_i\eta_i} |\nu_i(0)\rangle \tag{1.11}$$

where m_i is the mass of ν_i, and η_i is the proper time in the neutrino rest frame.

In terms of the time t and position L in the laboratory frame, the Lorentz-invariant phase factor in Eq. 1.11 may be written

$$e^{-im_i\eta_i} = e^{-i(E_i t - p_i L)} \tag{1.12}$$

were E_i and p_i are, respectively, the energy and momentum of ν_i in the laboratory frame. In practice, the neutrino will be extremely relativistic and will propagate almost at the velocity of light. So, the phase factor of Eq. 1.12 can be evaluated with $t \simeq L$ and it becomes $e^{-i(E_i - p_i)L}$. If ν_α has been produced with a definite momentum p, all of its mass-eigenstate components have this common momentum. Then the ν_i component has $E_i = \sqrt{p^2 + m_i^2} \simeq p + m_i^2/2p$, assuming that all neutrino masses m_i are small compared to the neutrino momentum. The phase factor of Eq. 1.12 is then approximately $e^{-i(m_i^2/2p)L}$.

From this expression and Eq. 1.10, it follows that after a neutrino born

as a ν_α has propagated a distance L, its state vector has become

$$|\nu_\alpha\rangle \simeq \sum_i U^*_{\alpha i} e^{-i(m_i^2/2p)L} |\nu_i\rangle \tag{1.13}$$

Here, $E \approx p$ is the average energy of the various mass eigenstate components of the neutrino. Using the unitarity of U to invert Eq. 1.10 and inserting the result in Eq. 1.13, we find that

$$|\nu_\alpha\rangle \simeq \sum_\beta \left[\sum_i U^*_{\alpha i} e^{-i(m_i^2/2p)} L \right] |\nu_\beta\rangle \tag{1.14}$$

In traveling the distance L, ν_α has turned into a superposition of all the flavors. The probability that it has flavor β, $P(\nu_\alpha \to \nu_\beta)$, is $|\langle \nu_\beta | \nu_\alpha \rangle|$. From Eq. 1.14 and the unitarity of U, one has

$$\begin{aligned} P(\nu_\alpha \to \nu_\beta) &= \delta_{\alpha\beta} \\ &-4 \sum_{i<j} \Re(U^*_{\alpha i} U_{\beta i} U^*_{\alpha j} U_{\beta j}) \sin^2 \left[1.27 \Delta m^2_{ij} (L/E)\right] \\ &+2 \sum_{i<j} \Im(U^*_{\alpha i} U_{\beta i} U^*_{\alpha j} U_{\beta j}) \sin^2 \left[2.54 \Delta m^2_{ij} (L/E)\right] \end{aligned} \tag{1.15}$$

where $\Delta m^2_{ij} = m^2_i - m^2_j$ is in eV^2, L is in km, and E is in GeV and the previously omitted factors $\hbar$ and c are included.

The unitary matrix is usually parametrized in the following way

$$U = \begin{pmatrix} c_{12}c_{13} & s_{12}c_{13} & s_{13}e^{-i\delta} \\ -s_{12}c_{23} - c_{12}s_{23}s_{13}e^{i\delta} & c_{12}c_{23} - s_{12}s_{23}s_{13}e^{i\delta} & s_{23}c_{13} \\ s_{12}s_{23} - c_{12}s_{23}s_{13}e^{i\delta} & -c_{12}s_{23} - s_{12}c_{23}s_{13}e^{i\delta} & c_{23}c_{13} \end{pmatrix} \times \mathrm{diag}\left(e^{i\alpha_1/2}, e^{i\alpha_2/2}, 1\right) \tag{1.16}$$

where $c_{ij} \equiv \cos\theta_{ij}$ and $c_{ij} \equiv \sin\theta_{ij}$ and the three θ_{ij}'s are mixing angles. The quantities δ, α_1 and α_2 are CP-violating phases. The phases α_1 and α_2, known as Majorana phases, are the extra physically significant phases that U may contain when the neutrino mass eigenstates are Majorana particles.

Then these phases influence neutrinoless double beta decay. However, as we see from Eq. 1.15, α_1 and α_2 do not affect neutrino oscillation, regardless of whether neutrinos are Majorana particles.

In the special case where only two mass eigenstates, and the two corresponding flavor eigenstates, are relevant (for example, when only two mass eigenstates couple significantly to the charged lepton with which the neutrino being studied is produced) there is only a single splitting Δm^2 and one mixing angle θ. So the oscillation probability simplifies considerably, becoming

$$P(\nu_\alpha \to \nu_\beta) = \sin^2 2\theta \sin^2 \left(1.27\Delta m^2(\text{eV})\frac{L(\text{km})}{E(\text{GeV})}\right). \tag{1.17}$$

Many experiments have been analyzed using this expression. Assuming the three flavor neutrino oscillation framework and $\Delta m^2_{12} \ll \Delta m^2_{23} = \Delta m^2_{13} = \Delta m^2$, the oscillation probability can be expressed like:

$$P(\nu_\mu \to \nu_\tau) = \cos^4\theta_{13} \sin^2 2\theta_{23} \sin^2\left(1.27\Delta m^2 L/E\right) \tag{1.18}$$

$$P(\nu_\mu \to \nu_e) = \sin^4\theta_{23} \sin^2 2\theta_{13} \sin^2\left(1.27\Delta m^2 L/E\right) \tag{1.19}$$

$$P(\nu_\mu \to \nu_\mu) = 1 - P(\nu_\mu \to \nu_\tau) - P(\nu_\mu \to \nu_e) \tag{1.20}$$

where Δm^2 and θ_{23} control the dominant atmospheric oscillation $\nu_\mu \to \nu_\tau$ and the sub-leading $\nu_\mu \to \nu_e$ oscillation at the atmospheric scale is driven by the mixing angle θ_{13}.

1.3 Mikheyev-Smirnov-Wolfenstein effect

When neutrinos travel through matter, their coherent forward scattering from particles they encounter along the way can significantly modify their propagation [22]. As a result, the probability for changing flavor can be rather different than in vacuum [23]. Flavor change that occurs in matter, and that grows out of the interplay between flavor-nonchanging neutrino-matter interactions and neutrino mass and mixing, is known as the Mikheyev-Smirnov-Wolfenstein (MSW) effect.

To a good approximation, one can describe neutrino propagation through matter via a Schrödinger-like equation. In the framework of three neutrino flavor, this equation governs the evolution of a neutrino state vector with three components, m_{ν_e}, m_{ν_μ}, m_{ν_τ}. The effective Hamiltonian in the equation, a matrix $\mathcal{H}$ in neutrino flavor space, differs from its vacuum counterpart by the addition of interaction energies arising from the coherent forward neutrino scattering. For example, the $\nu_e - \nu_e$ element of $\mathcal{H}$ includes the interaction energy

$$V = \sqrt{2} G_F N_e, \tag{1.21}$$

arising from W-exchange-induced ν_e forward scattering from ambient electrons. Here, G_F is the Fermi constant, and N_e is the number of electrons per unit volume. In addition, the $\nu_e - \nu_e$, $\nu_\mu - \nu_\mu$, and $\nu_\tau - \nu_\tau$ elements of $\mathcal{H}$ all contain a common interaction energy growing out of Z-exchange-induced forward scattering. However, when one is not considering the possibility of transitions to sterile neutrino flavors, this common interaction energy merely adds to $\mathcal{H}$ a multiple of the identity matrix, and such an addition has no effect on flavor transitions.

The effect of matter is illustrated by the propagation of solar neutrinos through solar matter. When combined with information on atmospheric neutrino oscillations, the experimental bounds on short-distance ($L < 1$ km) oscillation of reactor $\bar{\nu}_e$ [24, 25] tell us that, if there are no sterile neutrinos, then only two neutrino mass eigenstates, ν_1 and ν_2, are significantly involved in the evolution of the solar neutrinos. Correspondingly, only two flavors are involved: the ν_e flavor with which every solar neutrino is born, and the effective flavor ν_x some linear combination of ν_μ and ν_τ which it may become.

1.4 Experimental evidences

All existing data on neutrino oscillations can be separately analyzed in an effective two neutrino framework, *i.e.* the data do not indicate any genuine three flavor effect. The reason for this is that there is a pronounced hierarchy of mass splittings $|\Delta m^2_{12}| \ll |\Delta m^2_{23}|$ and that the angle θ_{13} which couples the two oscillations is small. Therefore the presentation of the current knowledge on neutrino mixing parameters can be divided into three subsets:

- oscillations with $|\Delta m^2_{12}|$ and θ_{12} from solar neutrino experiments;

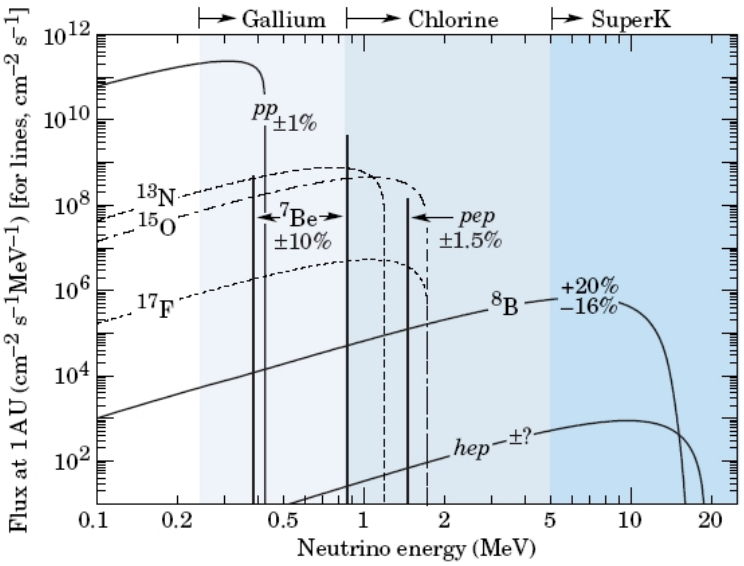

Figure 1.1: BP2000 [26] predictions of the energy spectra of the solar neutrinos produced in the pp-cycle reactions [27].

- oscillations with $|\Delta m^2_{23}|$ and θ_{23} from atmospheric neutrino experiments;
- limit on θ_{13} from reactor experiments.

1.4.1 Solar neutrino parameters: $\left|\Delta m^2_{12}\right|$ and θ_{12}

The Sun is an intense source of low-energy (< 0.42MeV) electron neutrinos based on the basic fusion reaction

$$\mathrm{pp} \rightarrow \mathrm{D}e^{+}\nu_e. \tag{1.22}$$

In addition, electron neutrinos with energies up 18 MeV are produced in side reactions, the most important of which involve the nuclei ^{7}Be and ^{8}B. The correspondent spectra are shown in Fig. 1.1.

The neutrinos created in the Sun have been detected on Earth by several experiments. Solar neutrinos were first detected by Davis, from 1968 onwards, in an experiment located in the Homestake mine in South Dakota, USA [28]. This is a radiochemical experiment that counted the ^{37}Ar atoms

produced by the reaction

$$\nu_e + {}^{37}\mathrm{Cl} \rightarrow e^- + {}^{37}\mathrm{Ar}, \tag{1.23}$$

which has a threshold of 0.81 MeV, above the endpoint of the pp energy spectrum.

A second group of experiments [29] used gallium as the target medium, exploiting the reaction

$$\nu_e + {}^{71}\mathrm{Ge} \rightarrow e^- + {}^{71}\mathrm{Ge}, \tag{1.24}$$

for which the energy threshold (0.23 MeV) is below the maximum energy of the pp neutrinos.

For years, solar neutrino experiments had been finding that the solar ν_e flux arriving at the Earth is below the one expected from neutrino production calculations according to the *Solar Standard Model* [30] and subsequently confirmed by several measurements [31].

Complementary results were obtained from water Cherenkov detectors. Kamiokande [32] and Super-Kamiokande [33] measured Cherenkov light from ν_e scattering

$$\nu_e + e^- \rightarrow \nu_e + e^-, \tag{1.25}$$

with an energy threshold in the region of 5÷10 MeV. These experiments are able to measure electron energy spectrum and neutrino direction in real time.

Finally, the Sudbury Neutrino Observatory (SNO) detects Cherenkov light in a heavy-water detector. It has shown compelling evidence that the missing ν_e have simply changed into neutrinos of other flavors. This experiment detects these neutrinos via the reactions

$$(\mathrm{CC}) \qquad \nu_e + \mathrm{d} \rightarrow e^- + \mathrm{p} + \mathrm{p}, \tag{1.26}$$

$$(NC) \qquad \nu_x + \mathrm{d} \rightarrow \mathrm{p} + \mathrm{n}, \tag{1.27}$$

$$(ES) \qquad \nu_x + e^- \rightarrow \nu_x + e^-. \tag{1.28}$$

The first of these reactions, charged-current deuteron breakup, can be initiated only by a ν_e and has a threshold of 1.4 MeV. Thus, it measures the flux $\Phi(\nu_e)$ of ν_e from ^{8}B decay in the Sun. The second reaction, neutral-current deuteron breakup, can be initiated with equal cross sections by neutrinos of all active flavors and has a threshold of 2.2 MeV. Thus, it measures

$\Phi(\nu_e) + \Phi(\nu_{\mu,\tau})$, where $\Phi(\nu_{\mu,\tau})$ is the flux of ν_μ and/or ν_τ from the Sun. Finally, the third reaction, neutrino electron elastic scattering, can be triggered by a neutrino of any active flavor, but the cross section for ν_e is 6.5 larger than for the other flavors. Thus, this reaction measures $[\Phi(\nu_e) + \Phi(\nu_{\mu,\tau})/6.5]$. Recently, SNO has reported the results of measurements made with increased sensitivity to the neutral-current deuteron breakup [34]. From its observed rates for the two deuteron breakup reactions, SNO finds

$$\frac{\Phi(\nu_e)}{\Phi(\nu_e) + \Phi(\nu_{\mu,\tau})} = 0.306 \pm 0.026(\text{stat}) \pm 0.024(\text{syst}). \tag{1.29}$$

Clearly, $\Phi(\nu_{\mu,\tau})$ is not zero. This non-vanishing $\Phi(\nu_{\mu,\tau})$ flux from the Sun is smoking-gun evidence that some of the ν_e produced in the solar core do indeed change flavor.

Change of neutrino flavor, whether in matter or vacuum, does not change the total neutrino flux. Thus, unless some of the solar ν_e are changing into sterile neutrinos, the total active high-energy flux measured by the NC reaction Eq. 1.28 should agree with the predicted total ^{8}B solar neutrino flux of the Solar Standard Model, $(5.05^{+1.01}_{-0.81}) \times 10^6 \text{cm}^{-2}\text{s}^{-1}$) [26]. By comparison, the total active flux measured by NC reaction is $[5.21 \pm 0.27(stat) \pm 0.38(\text{syst})] \times 10^6 \text{cm}^{-2}\text{s}^{-1}$, in good agreement. This agreement provides evidence that neutrino production in the Sun is correctly understood. Moreover, it strengthens the evidence that neutrinos really do change flavor and that the previously-reported deficits of solar ν_e flux are due to this change of flavor.

The strongly favored explanation of solar neutrino flavor change is the LMA-MSW effect. According to this effect, when neutrinos travel through matter, *e.g.* in the Sun, their coherent forward scattering from particles they encounter along the way can significantly modify their propagation [22].

The LMA-MSW interpretation of solar neutrino behavior implies that a substantial fraction of MeV reactor $\bar{\nu}_e$'s that travel more than a hundred kilometers should disappear into anti-neutrinos of other flavors.

KamLAND, a long-baseline experiment, studies reactor $\bar{\nu}_e$ that typically travel 180 km to reach the detector through the raction

$$\bar{\nu}_e + \text{p} \rightarrow e^+ + \text{n}, \tag{1.30}$$

It finds that the $\bar{\nu}_e$ flux is only $0.611 \pm 0.085(stat) \pm 0.041(syst)$ of what it would be if no $\bar{\nu}_e$ were vanishing [35].

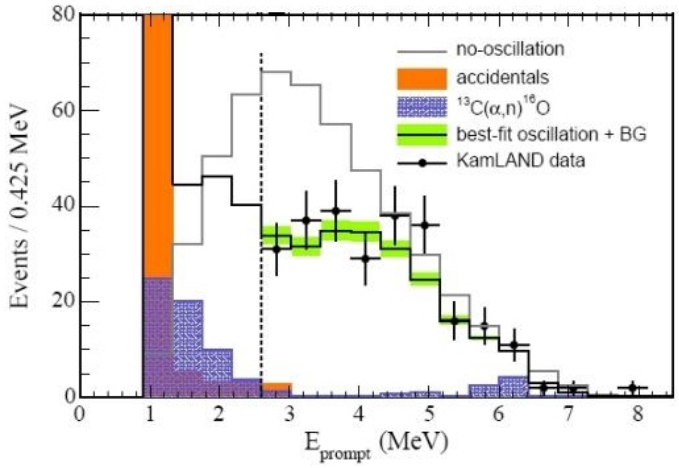

Figure 1.2: KamLAND experiment. Positron energy spectrum of $\bar{\nu}_e$ candidate events with associated background spectra. The dashed vertical line indicates the analysis cut used to remove the geological-neutrino and background-neutrino contributions.

The energy spectrum distribution of the data collected by KamLAND is given in Fig. 1.2 compared with the expected one in absence of oscillations. Fig. 1.3 shown the L/E distribution, where the data and the best-fit spectra are divided by the expected no-oscillation spectrum.

Both the KamLAND result and all the solar neutrino data can be described by the same neutrino parameters, in the LMA-MSW region. The best fit values for the oscillation parameters are

$$\begin{aligned} &\Delta m^2_{12} = 7.1 \times 10^{-5}\ \text{eV}^2 \\ &\theta_{12} = 32.5^0. \end{aligned} \tag{1.31}$$

1.4.2 Atmospheric neutrino parameters: $\left|\Delta m^2_{23}\right|$ and θ_{23}

The atmospheric neutrinos are produced in the Earth's atmosphere by primary cosmic ray interactions and decays and then they detected in underground detectors. The flux of cosmic rays that lead to neutrinos with energies above a few GeV is isotropic, so that these neutrinos are produced at the same rate all around the Earth. This implies that at any underground site,

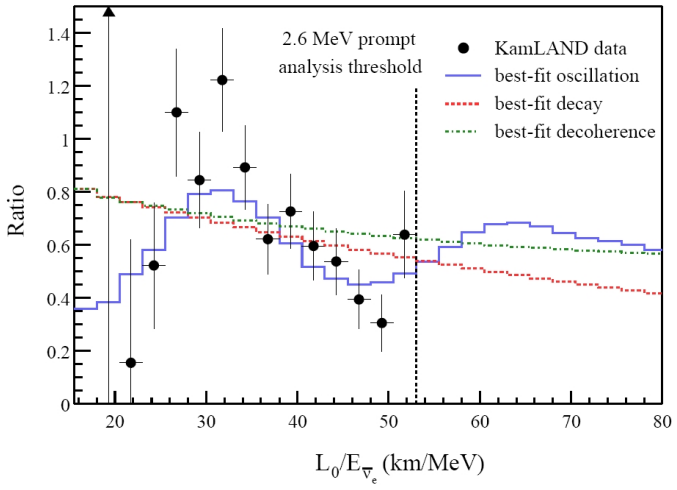

Figure 1.3: KamLAND experiment. Ratio of the observed $\bar{\nu}_e$ spectrum to the expectation for no oscillation versus L/E. The curves show the expectation for the best-fit oscillation, best-fit decay and best-fit decoherence models taking into account the individual time-dependent flux variations of all reactors and detector effects. The data points and models are plotted with $L = 180$ km, as if all anti-neutrinos detected in KamLAND were due to a single reactor at this distance.

the downward- and upward-going fluxes of neutrinos of a given flavor must be equal. That is, unless some mechanism changes the flux of neutrinos of the given flavor as they propagate, the flux coming down from zenith angle θ_Z must equal that coming up from angle $\pi - \theta_Z$.

The experiments MACRO [36], Super-Kamiokande [37] and Soudan 2 [38] indicate that the atmospheric neutrino anomaly can be explained by assuming oscillations in the $\nu_\mu \rightarrow \nu_\tau$ channel with maximal mixing and Δm^2_{23} of a few 10^{-3} eV^2. These results were obtained using different techniques and observing events in different energy ranges.

The simulation of atmospheric neutrino events requires physics generators based on atmospheric neutrino fluxes and neutrino cross sections. Despite the recent development in this field, the absolute normalization is still uncertain and this uncertainty increases with energy [39]. In the past unidimensional Monte Carlo codes were used [40], while, at present, three dimensional Monte Carlo predictions for neutrino fluxes, based on improved hadronic model

and new fit of the primary cosmic ray flux, are available [41]. All these Monte Carlo's provide the same shape of the angular distributions for ν_μ flux. The absolute value predicted by the new Monte Carlo's is ∼25% too low at high energies and ∼12% at low energies respect to experimental data. This difference is very probably due to the use of a new fit of the cosmic ray data. In order to minimize the impact of the atmospheric neutrino flux uncertainty on the oscillation parameter measurement, the experiments have chosen to use quantities known at the level of 5%, such as the distributions of zenith angles and ratios where most of the errors cancel, *e.g.* vertical-horizontal and low-high energy. In Super-Kamiokande the evidence for neutrino oscillations lies in the shape of the angular distribution and in the ratio of ν_μ/ν_e. In MACRO the evidence is mainly due to the shape of the high energy angular distribution.

The underground Super-Kamiokande detector finds that, for low energy atmospheric muon neutrinos,

$$\frac{\Phi^{Up}(-1.0 < \cos(\theta_Z) < -0.2)}{\Phi^{Down}(+0.2 < \cos(\theta_Z) < +1.0)} = 0.54 \pm 0.04, \tag{1.32}$$

in strong disagreement with equality of the upward and downward fluxes. Thus, some mechanism does change the ν_μ flux as the neutrinos travel to the detector. The most attractive candidate for this mechanism is the oscillation $\nu_\mu \rightarrow \nu_x$ of the muon neutrinos into neutrinos ν_x of another flavor. Since the upward-going muon neutrinos come from the atmosphere on the opposite side of the Earth, they travel much farther than the downward-going ones to reach the detector. Thus, they have more time to oscillate into the other flavor, which explains why $\Phi^{Up} < \Phi^{Down}$. The zenith angle distributions of the neutrino events are shown in Fig. 1.4. The data over non-oscillated Monte Carlo as a function of neutrino flight length L over neutrino energy E is shown in Fig. 1.5. A dip, which should correspond to the first oscillation minimum, is observed around $L/E = 500$ km/GeV.

The analysis of atmospheric neutrino events collected with the MACRO detector indicates a flux deficit that depends on energy and pathlength of neutrinos. In Fig. 1.6 the data are compared with the different oscillated and non-oscillated Monte Carlo calculations. It is clear from the figure that the new Monte Carlo predictions using the recent fit to the primary cosmic ray energy distribution yields a neutrino flux that is too low to account for the measurement of upward-going muons. The zenith angle provides a measure of

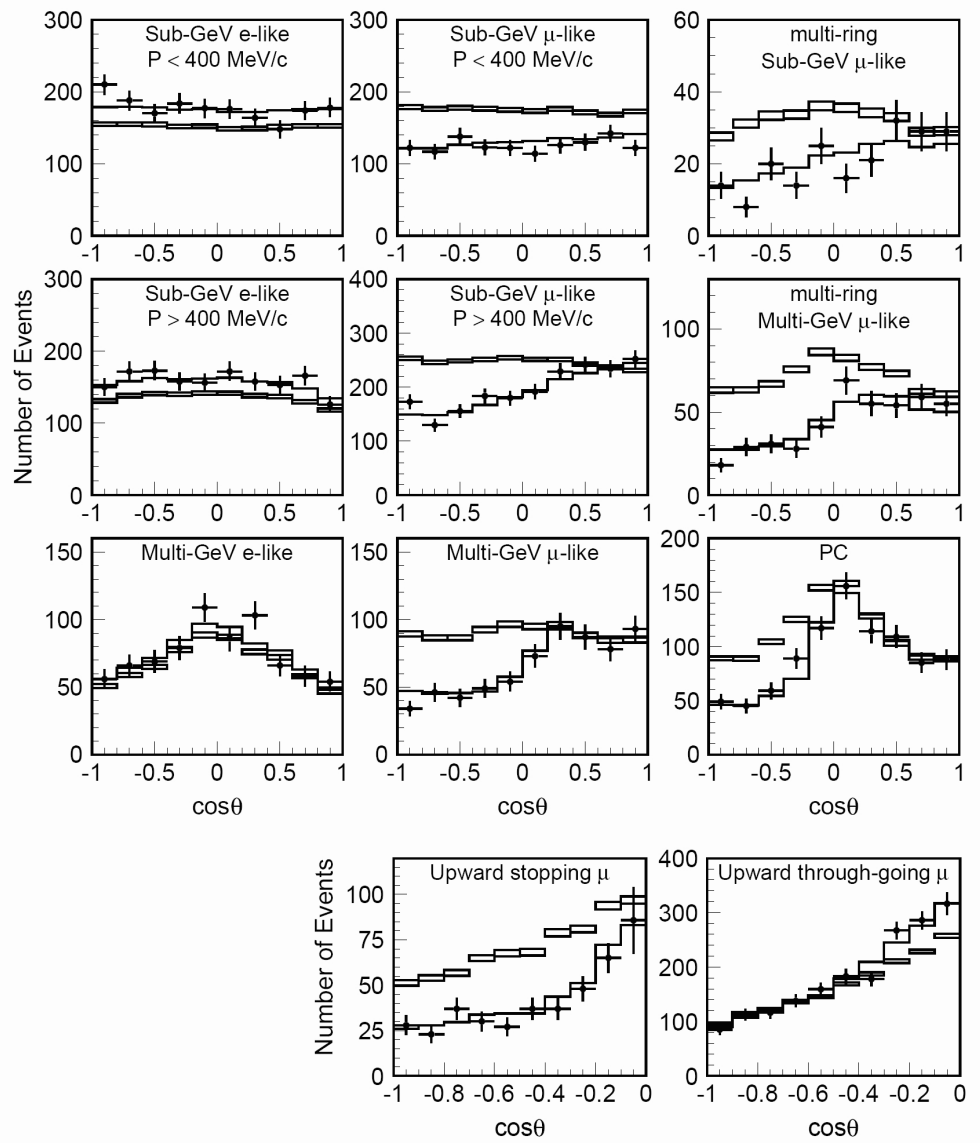

Figure 1.4: Super-Kamiokande experiment. Zenith angle distribution for the different event classes: fully-contained 1-ring events, multi-ring events, partially-contained events and upward-going muons. The points are the data, the box histograms are the non-oscillated Monte Carlo events and the lines are the best-fit for $\nu_\mu \to \nu_\tau$ oscillations with $\sin^2 2\theta_{23} = 1$ and $\Delta m^2_{23} = 2.1 \times 10^{-3}$ eV^2. The heights of the boxes shows the statistical errors of the Monte Carlo.

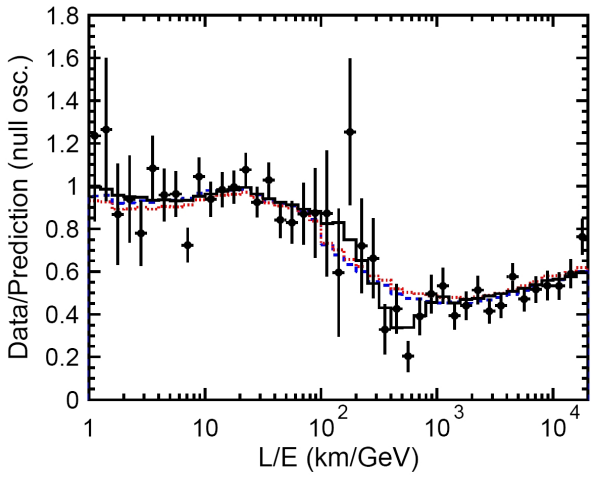

Figure 1.5: Super-Kamiokande experiment. Ratio of the data to the Monte Carlo events without neutrino oscillations (points) vs. L/E compared with with the best-fit expectation for 2-flavor ν oscillation expectation (solid line). Also shown are the best-fit expectation for neutrino decay (dashed line) and neutrino decoherence (dotted line).

the path-length traveled by the neutrino before it interacts, L, and together with a measure of the its energy by means of multiple Coulomb scattering in the detector rock absorbers with the streamer tubes system, allows to estimate the ratio L/E. The ratio data/Monte Carlo (in the hypothesis of no oscillations) as a function of the estimated L/E for the upward-going muon sample is shown in Fig. 1.7.

Thus, ν_x is a ν_τ, a sterile neutrino ν_s, or a mix of them. All the data by MACRO, Sudan 2 and Super-Kamiokande are well described by the hypothesis that the oscillation is purely $\nu_\mu \to \nu_\tau$ (the 90% C.L. upper limit on the fraction of ν_x that is sterile is 19% [42]). In a two-neutrino oscillation scenario, the oscillation parameters are, at 90% C.L., in the range

$$\begin{aligned} &1.5 \times 10^{-3}\ \text{eV}^2 < \Delta m^2_{23} = 3.4 \times 10^{-3}\ \text{eV}^2, \\ &\sin^2 2\theta_{23} > 0.9. \end{aligned} \tag{1.33}$$

This value implies that at least one neutrino mass eigenstate has a mass of the order of 40 meV.

The oscillation interpretation of the atmospheric neutrino data has received support from K2K (KEK to Kamioka), the first high energy long-

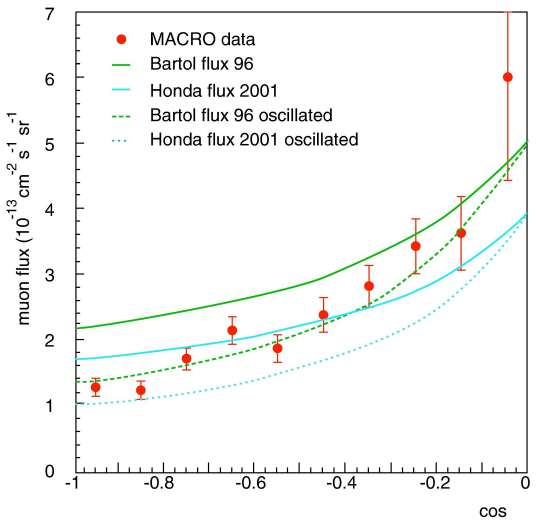

Figure 1.6: MACRO experiment. Comparison between the measured data (black points with error bars) of the upward-going muon flux and the old and new Monte Carlo predictions with and without ν-oscillations with the MACRO parameters. The best-fit oscillation parameters are $\Delta m^2_{23} = 2.3 \times 10^{-3}$ eV^2 and $\sin^2 2\theta_{23} = 1$.

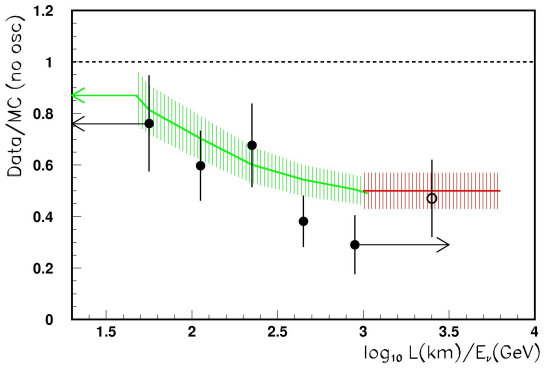

Figure 1.7: MACRO experiment. Ratio data/Monte Carlo (no oscillations) as a function of the estimated L/E for the upward-going muon sample (black points). The solid line is the Monte Carlo expectation assuming $\Delta m^2_{23} = 2.3 \times 10^{-3}$ eV^2 and $\sin^2 2\theta = 1$. The last point (empty circle) is obtained from the sample of upward-going muon generated in the detector.

baseline experiment in operation [43]. The ν beam is produced by the 12 GeV proton accelerator at KEK and is almost entirely ν_μ, as confirmed by data from the near detector at KEK, which measures the neutrino flux and energy spectrum immediately after production. The far detector is Super-Kamiokande, located 250 km away from KEK. The energy spectrum of the neutrino beam is similar to that of atmospheric neutrinos, and the L/E of this experiment is such that one expects to see an oscillation dominated by the atmospheric squared-mass splitting Δm^2_{23}.

Using data collected until February 2004, K2K observed 107 beam-induced neutrino interactions in Super-Kamiokande. In the absence of neutrino oscillations, the expected number of such events would be 151^{+12}_{-10}(syst). The K2K data are consistent with the atmospheric neutrino oscillations published by previous experiments, being the best fit oscillation parameters the following

$$\begin{array}{l} \Delta m^2_{23} = 2.8 \times 10^{-3}\ \mathrm{eV}^2 \\ \sin^2 2\theta_{23} = 1. \end{array} \tag{1.34}$$

K2K also reported evidence for the energy dependence of the oscillation effect. The distortion of neutrino spectrum is shown in Fig.1.8.

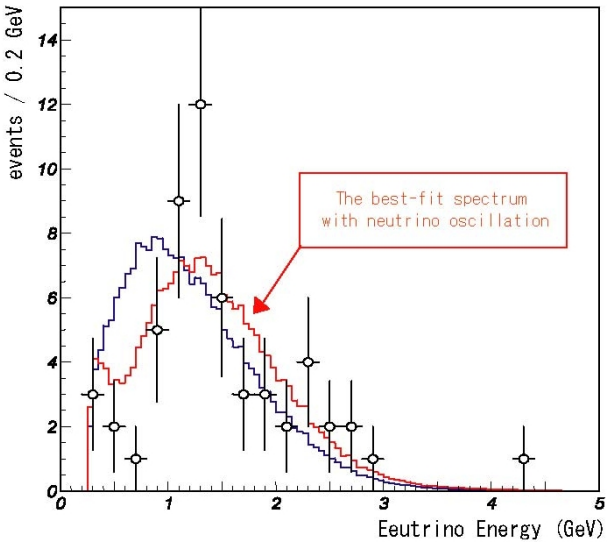

Figure 1.8: K2K experiment. Distortion of neutrino energy spectrum observed at Super-Kamiokande (data points), compared to the scaled KEK beam spectrum (histogram with black line), which represents expectation in the absence of neutrino oscillations. Also shown is the expected spectrum taking into account neutrino oscillation effects (histogram with red line), applying the K2K best-fit oscillation parameters ($\Delta m^2_{23} = 2.8 \times 10^{-3}$ eV^2 and $\theta_{23} = 45^0$).

1.4.3 Sub-dominant oscillations: limit on θ_{13} from reactor experiments

The null results of short-baseline reactor neutrino experiments imply limits on $P(\bar{\nu}_\mu \to \bar{\nu}_x)$, which, assuming CPT invariance, are also limits on $P(\nu_\mu \to \nu_x)$.

The CHOOZ [24] and Palo Verde [25] experiments detected reactor $\bar{\nu}_e$ via the inverse β-decay reaction

$$\bar{\nu}_e + \mathrm{D} \to \mathrm{p} + \mathrm{n} \tag{1.35}$$

They gave an important contribution to solving the problem of the atmospheric neutrino anomaly, by removing the possibility of explaining the atmospheric neutrino anomaly by $\nu_\mu \to \nu_e$ in Fig. 1.9 [24].

They constraint the sub-leading $\nu_\mu \to \nu_e$ to be small, ($\sin^2 2\theta_{13} \leq 0.10$).

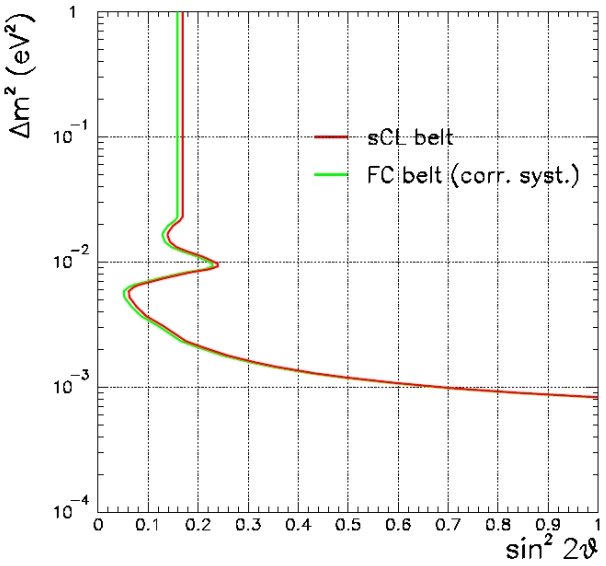

Figure 1.9: CHOOZ experiment. Exclusion plot at 90% C.L. for the oscillation parameters based on the differential energy spectrum; the FC contour, obtained with "correct systematics" treatment, is also shown.

Chapter 2

The OPERA experiment

The neutrino oscillation hypothesis as explanation of both the solar neutrino puzzle and the atmospheric neutrino anomaly has been confirmed by several experiments, as shown in the previous Chapter. Anyway, so far, the oscillation signal was obtained through the disappearance of the initial neutrinos, while the direct observation of the new neutrino is still missing.

OPERA (**O**scillation **P**roject with **E**mulsion-t**R**acking **A**pparatus) is a long baseline experiment proposed for the direct search of ν_τ's appearance in an almost pure ν_μ beam (the CNGS neutrino beam) [44]. It will be located at the Gran Sasso Underground Laboratory, in the middle of Italy, at a distance of 732 km from CERN, where a facility producing muon neutrinos is under construction (CNGS). The neutrino beam energy will be tuned above the τ lepton production threshold and in the oscillation parameter region indicated by the atmospheric neutrino experiments.

OPERA is looking for the direct observation of $\nu_\mu \leftrightarrow \nu_\tau$ appearance, which would constitute a milestone in the study of neutrino oscillations.

2.1 The CNGS beam line

The CNGS is a ν_μ beam produced with 400 GeV protons extracted from the SPS complex at CERN [45]. In a mode of operation where the SPS is shared with LHC, 4.5×10^{19} protons on target (pot) can be delivered in one year with a 200 days run. The protons hit a target made of graphite rods and the produced secondary particles pass through a magnetic focusing system designed to select $20 \div 50$ GeV π^+ and K^+. This makes the neutrino beam

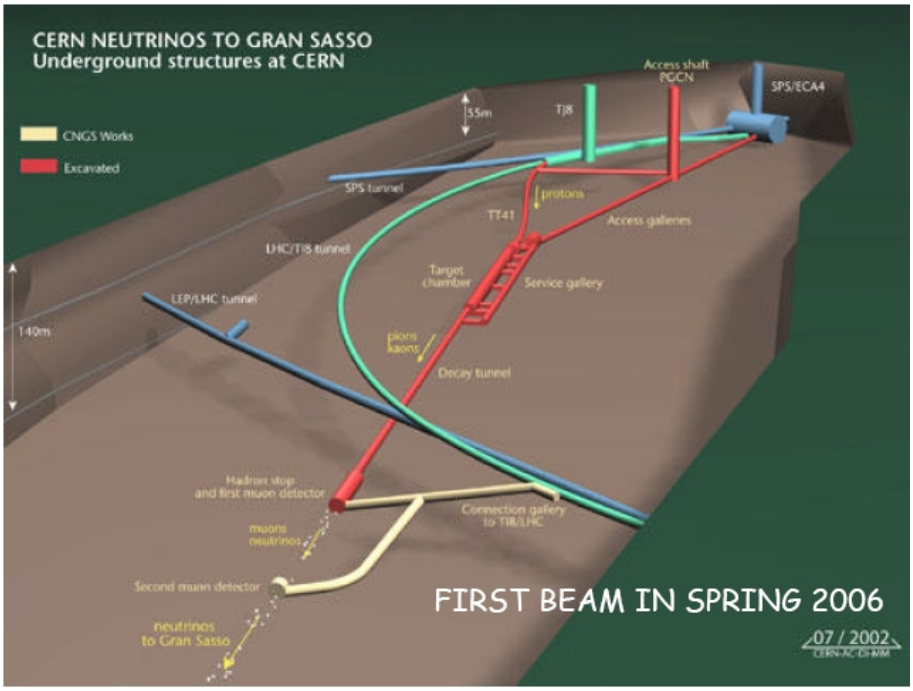

Figure 2.1: Underground structures of the beam line at CERN.

a high energy beam optimized for ν_τ appearance with the mean neutrino energy of about 17 GeV. Fig. 2.1 shows the underground structures of the beam line at the CERN site, while Fig. 2.2 shows the expected neutrino energy distribution at Gran Sasso, located at 732 km from CERN.

The ν_μ flux at Gran Sasso is 3.5×10^{11} $\nu/\mathrm{m}^2/\mathrm{year}$ with a contamination of 2.1% $\bar{\nu}_\mu$, 0.8% ν_e and less than 0.05% $\bar{\nu}_e$. The prompt ν_τ contamination (mainly from D_s decays) is negligible. The number of charged current interactions expected from ν_μ is about 2600/kton/year. If the $\nu_\mu \leftrightarrow \nu_\tau$ oscillation hypothesis is confirmed the number of τ's produced via charged current interactions at Gran Sasso is about 12.8/kton/year for $\Delta m^2 = 2.4 \times 10^{-3}$ eV^2 and maximal mixing.

Civil engineering works are finished and the accelerator team plans to deliver the first neutrino beam by May 2006. The possibility of an increase of the neutrino beam intensity is being studied by the CNGS design group and other groups working on the PS and SPS machines: it is expected that the maximum intensity accelerated in the SPS could be 7×10^{13} rather than

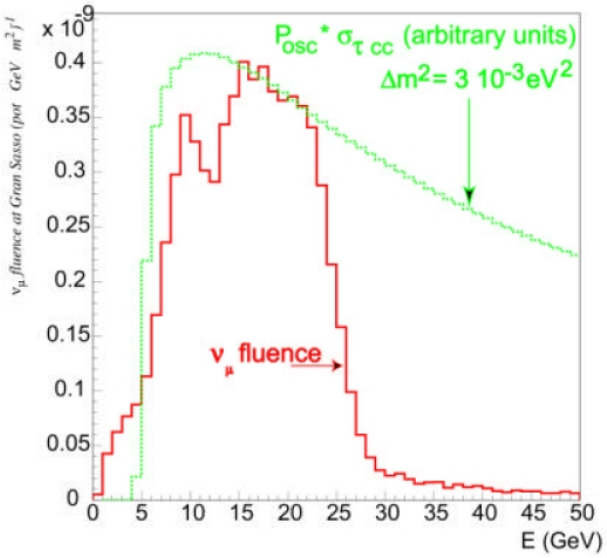

Figure 2.2: Histogram with dark line: CNGS ν_μ fluence as a function of the energy at Gran Sasso Underground Laboratory. The histogram with thin line shows the energy dependence of the production rate of τ's produced via charged current interaction for $\Delta m^2 = 3.0 \times 10^{-3}$ eV^2 and maximal mixing.

4.5×10^{13} pot/cycle. All the improvements could increase the proton flux by a factor 1.5.

The low ν_e ($\bar{\nu}_e$) contamination allows to search for the sub-dominant $\nu_\mu \leftrightarrow \nu_e$ oscillation seeking an excess of ν_e charged-current (CC) interactions [46]. The systematic error associated with the ν_e contamination plays an important role for the $\nu_\mu \leftrightarrow \nu_e$ oscillation search, the statistical fluctuation of the ν_e component being the other limiting factor. This uncertainty depends on the knowledge of the K yield. It can be assumed a 5% systematic error on the overall ν_e flux [47].

2.2 The detector

The ν_τ appearance search is based on the observation of $\tau^\pm$ events produced by CC interactions, with the $\tau^\pm$ decaying in all possible decay modes. The

possible τ^- decays are

$$\tau^- \rightarrow e^- \nu_\tau \overline{\nu}_e$$
$$\tau^- \rightarrow \mu^- \nu_\tau \overline{\nu}_\mu$$
$$\tau^- \rightarrow h^- \nu_\tau (n\pi^0)$$

Since the expected event rate is small, it is crucial to separate efficiently the ν_τ CC events from all the other flavor neutrino events and to keep the background at a very low level. To this purpose, the detectors will have to identify the event by exploiting the τ decay specific properties, characterized by a short lifetime and the presence of missing transverse momentum due to the ν_τ in the final state.

The OPERA apparatus consists of 2 identical parts called *supermodules* (SM). Each SM has a target section, equipped with electronic detectors and emulsion targets, and a muon spectrometer. Tab. 2.1 lists the SM features. Fig. 2.3 shows the general layout of the OPERA detector. A snapshot taken underground at the beginning of October 2004 is shown in Fig. 2.4.

Dimensions (m^3)	~6.71(H) x 6.75(W) x 3.75(L)
Thickness of one layer of ECC (mm)	1.3
Number of emulsions films/brick	57 + 1 CS
Brick x-section (cm^2)	10.2 x 12.7
Brick thickness (cm)	7.6 (packing not included)
Brick thickness (X_0)	10
Brick weight (kg)	7.9 (lead) + 0.4 (films) = 8.3
Module thickness (cm)	12
Number of modules/superm.	31
Number of bricks/superm.	103168
Emulsions films surface/superm. (m^2)	~75000
Target weight/superm. (ton)	815 (lead) + 41 (films) = 856

Table 2.1: Design features of the target section of a supermodule. H stands for height, W for width and L for length.

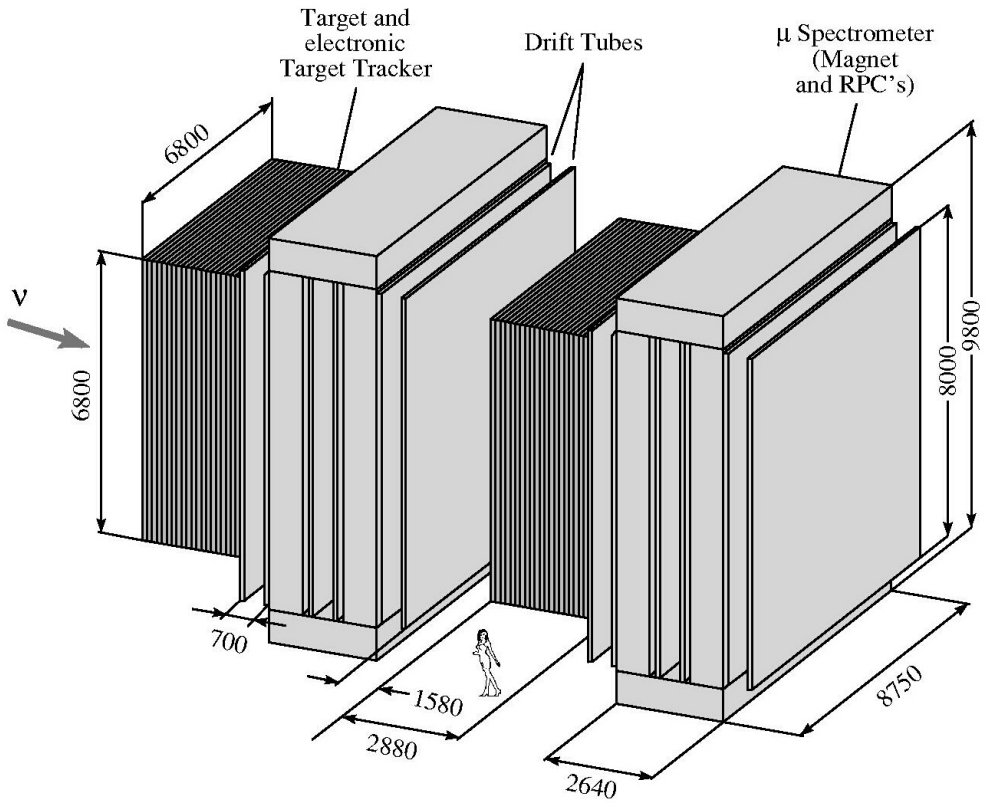

Figure 2.3: Layout of the OPERA detector composed of 2 supermodules with 2 spectrometers.

Figure 2.4: Status of detector installation in October 2004. The first magnet is fully installed and the filling of the target modules in the first supermodule had started.

2.2.1 Emulsion target

To provide the large target mass (1.8 ktons) the emulsion sheets are interleaved with 1 mm thick lead plates. The basic structure of the emulsion detector is called Emulsion Cloud Chamber (ECC). An emulsion sheet in OPERA consists of two emulsion layers (each $\sim$42 μm thick) put on either side of a plastic base (210 μm thick).

The basic detector unit, called an ECC *brick*, is obtained with 57 emulsion sheets interspersed by 56 Pb plates, plus an extra film, called Changeable Sheet (CS), behind 2 mm of plastic plate. The CS, tightly attached to the brick, can be detached from the rest of the brick for analysis. It will be used to promptly locate the tracks produced in neutrino interactions which have to be followed in the rest of the brick. The dimensions of the brick are $12.5 \times 10.2 \times 7.5$ cm^3, the weight is 8.3 kg. In terms of radiations length, a brick corresponds to a thickness of 10 X_0, which is long enough to allow electron identification, through their electromagnetic showering, and momentum measurement by multiple Coulomb scattering following tracks in consecutive emulsion sheets. Approximately 210000 bricks will be installed into walls, each containing 64×52 bricks.

Fig. 2.5 shows a schematic layout of all detectors installed in one OPERA supermodule.

2.2.2 Target trackers

Each emulsion wall will be followed downstream with two plane of electronic trackers. The main goal of the electronic detector is to provide a trigger for the neutrino interactions and to localize the brick where the neutrino interaction took place in order to guide the scanning, by defining the region of the films to be scanned. The CS is used to confirm the brick choice.

An electronic target tracker module consists of two plane of 6.6 m long scintillator strips in each transverse directions (X and Y, horizontal and vertical) (see Fig.2.6). The strips, 2.6 cm wide and 1 cm thick, have Wave Length Shifting (WLS) fibers for readout by 64 multi-anode photomultiplier tubes. The transverse pointing accuracy is about 1.5 cm for CC events and 3.0 cm for NC events.

The selection of the brick containing the neutrino interaction vertex is performed by combining different algorithms based on the observed transverse and longitudinal event profiles as well as on the presence of individual

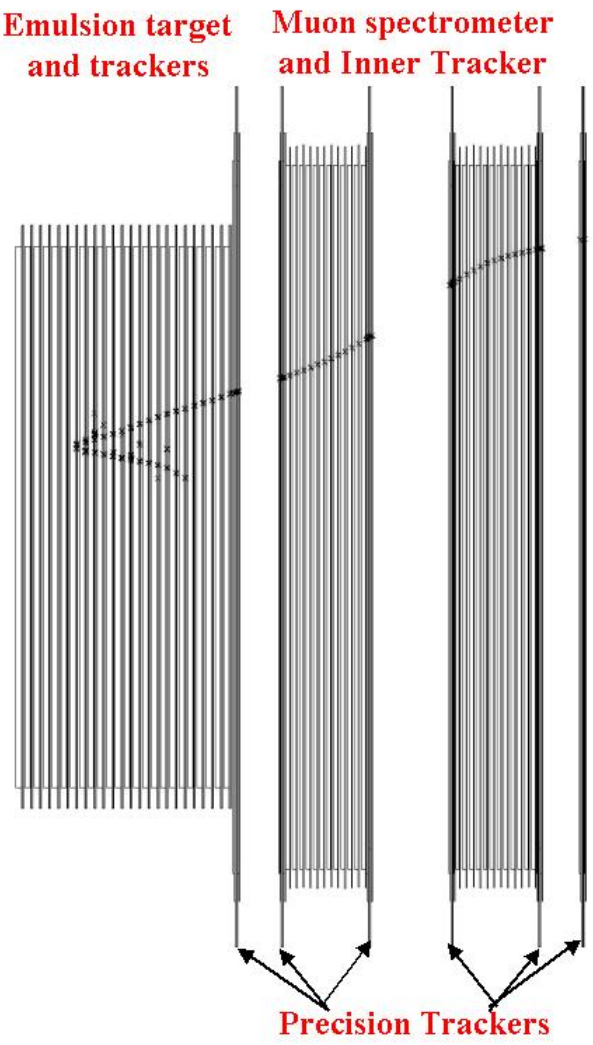

Figure 2.5: A schematic layout of the detectors installed in one OPERA supermodule. It is also shown a ν_μCC interaction. The muon track is bent in the spectrometer.

reconstructed tracks. As an illustration, Fig. 2.7 shows a simulated ν_τ event with a muonic decay for one of the two projections transverse to the beam direction. The overall efficiency to find the right brick is ∼70%.

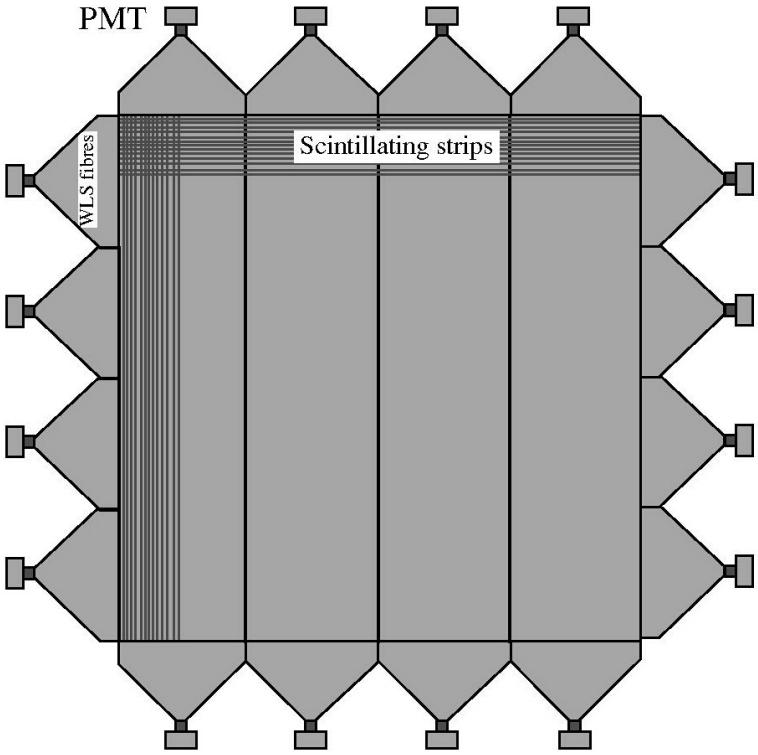

Figure 2.6: A schematic layout of the Target Tracker: two planes are installed after each emulsion wall.

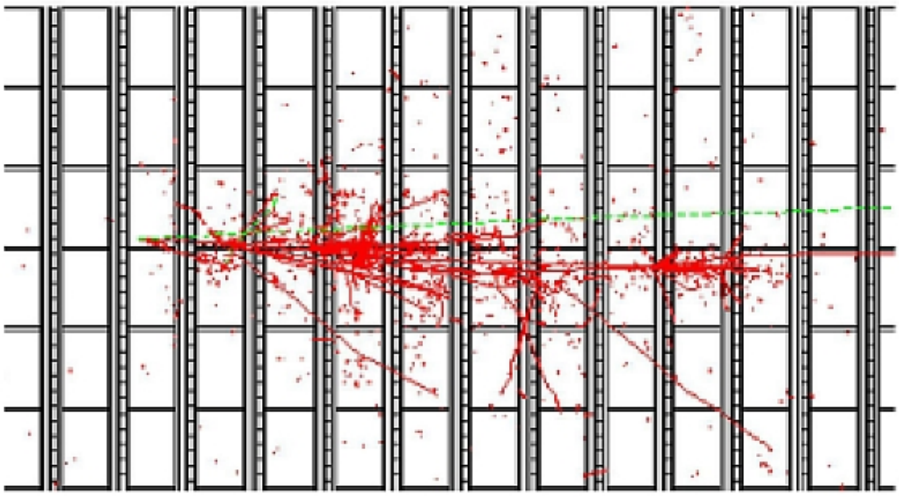

Figure 2.7: Display of a simulated $\tau \rightarrow \mu$ event in the OPERA target. The neutrino beam comes from the left. The primary vertex occurs in the third brick wall. The muon track corresponds to the longest track escaping on the right.

2.2.3 Muon spectrometers

The spectrometers measure the charge and the momentum of through going muons. Each spectrometer is made of two magnetized iron walls equipped active detectors (RPC and high-precision drift tube detectors interspersed with iron layers).

The transverse dimensions of a magnet are 8.75 m (horizontal) and 8 m (vertical) providing adequate geometrical acceptance also for muons originating in the upstream target volume.

The six wall per magnet of Precision Trackers (Fig. 2.5) consist of vertical drift tube planes with an intrinsic resolution of 0.3 mm in the bending direction. Allowing for some misalignment, an overall resolution on each measured coordinate of 0.5 mm is assumed. The two tracker planes housed between the two magnet walls provide an angular measurement of the track with a 100 cm lever arm. The lever arm for the external trackers is > 50 cm. This design leads to a momentum resolution of better than 30% in the relevant kinematical domain.

12+12 Inner Trackers are inserted between the iron plates of the two parts

of each magnet (Fig. 2.5). They are made of RPC detectors. On each face of the chambers, the induced pulses are collected by 3 cm wide pickup copper strips in the horizontal and vertical directions. The Inner Trackers allow a coarse tracking inside the magnet to identify muons and facilitate track matching between the Precision Trackers. They also provide a measurement of the tail of the hadronic energy leaking from the target and of the range of muons which stop in the iron.

2.2.4 OPERA operation mode

With the CNGS beam on, OPERA will run in a rather complex mode. First of all, upon the event trigger, a combined analysis of target tracker and spectrometer electronic detectors will produce an event classification (CC-like or NC-like event) and a "prediction" of the individual brick where the neutrino interaction happened. This candidate brick is extracted and the interface CS is detached and developed. In the meanwhile the brick is stored underground, waiting for CS scanning feedback.

The analysis flow will be dependent on the background density in the Changeable Sheets: some possible strategies are under study. One possible analysis flow is the following. If no track originating from neutrino interaction is found, the rest of the brick is left untouched for re-use and a suitable nearby brick is removed.

When a neutrino event is confirmed by the CS, the candidate brick is brought at lab surface and exposed to cosmic-rays inside a "pit", where it is shielded by 40 cm iron to minimize the electron component at mountain altitude [48]. Penetrating cosmic-ray muons will allow the sheet-to-sheet alignment with sub-micrometric precision, see Par. 3.4.2. Finally the brick is disassembled and processed, to be ready for scanning (refer to Par. 3.3 for more details about the emulsion scanning procedure). The run mode from the trigger to event location is sketched in Fig. 2.8 with some details of the target structure.

2.3 Physics performances

OPERA will study four event categories:

- Minimum-bias sample: about 1000 located neutrino interactions have

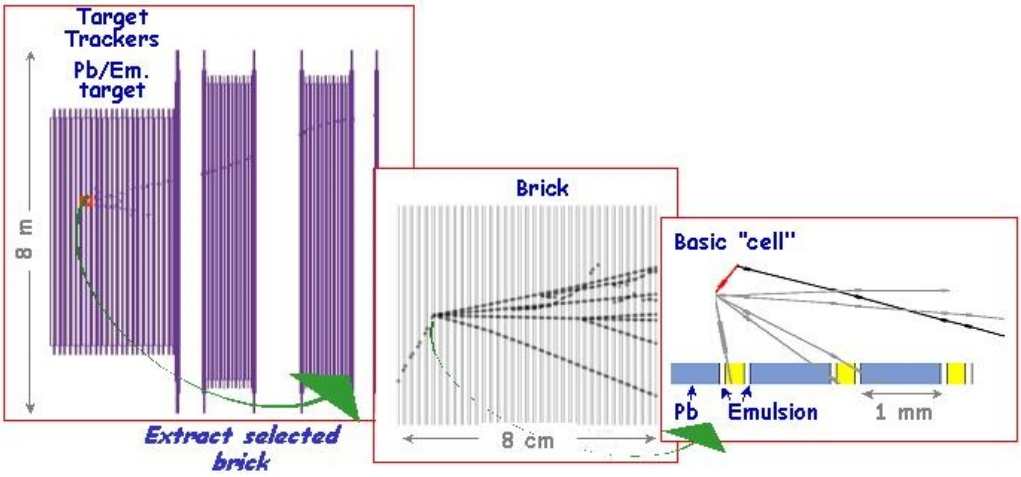

Figure 2.8: OPERA operation mode: the information of the electronic detectors locate the brick where the interaction happened. After brick extraction and measurements, the event is reconstructed.

to be carefully scanned in order to check the reliability of the Monte Carlo used and to fine tune the intranuclear interaction model in describing the interactions in lead;

- Events with charm production to validate the cross-section used to define the cuts in the hadronic channel;

- CCν_μ interactions to search for $\nu_\mu \leftrightarrow \nu_\tau$ oscillations;

- CCν_e interactions to search for $\nu_\mu \leftrightarrow \nu_e$ oscillations.

The first two samples are needed to reduce systematics on event location and detection efficiencies. The other two constitute the main OPERA physics program.

Moreover, the electronic detectors and the spectrometers will also able to measure all the neutrino interactions in the rock before the detector: this can allow to monitor the CNGS beam, *e.g.* the beam position and the flux, and to check $\nu_\mu \leftrightarrow \nu_\tau$ oscillation parameters.

2.3.1 τ detection

The signal of the occurrence of $\nu_\mu \leftrightarrow \nu_\tau$ oscillations is the CC interaction of ν_τ's in the detector target ($\nu_\tau N \rightarrow \tau^- X$), through the decay topologies of its decay modes into an electron, a muon or a single charged hadron. The branching ratios (BR) of the three single-prong decay modes are 17.8%, 17.7% and 49.5% for the electronic, muonic and hadronic channel, respectively [49]. For the typical τ energies expected with the CNGS beam one obtains the decay length distribution shown in Fig. 2.10.

If a τ is produced in a lead plate it will decay either in the same plate (*short decays*) or further downstream (*long decays*) as shown in Fig. 2.9. For long decays, the τ is detected by measuring the angle between the charged decay daughter and the parent τ direction. Fig. 2.11 shows the distribution of the τ decay kink angle for the electron channel. For this measurement the directions of the tracks before and after the kink are reconstructed (in space) by means of the pair of emulsion films sandwiching the lead plate where the decay vertex occurred. The τ can also decay in the same lead plate in which the primary interaction occurred or in one of the films or in the plastic base downstream of the vertex plate (short decay). The kink angle is reconstructed, albeit with a lower angular resolution, from the track segments in the emulsion layers on either side of the base. A fraction of the short decays is detectable by measuring a significant impact parameter (IP) of the daughter track with respect to the tracks originating from the primary vertex.

The detection of the τ decay into an electron benefits from the dense ECC structure, which allows the electron identification through its showering in the downstream emulsion sheets (Fig. 2.12).

2.3.2 Expected background

For the muonic decay mode the presence of the penetrating (often isolated) muon track allows an easier event vertex finding. The potential background from large angle scattering of muons produced in ν_μCC interactions can be reduced to a tolerable level by applying cuts on the kink angle and on the transverse muon momentum at the decay vertex.

Hadronic decay modes have the largest branching ratio but are affected by background due to hadron reinteractions. One of the primary hadrons may interact in the first lead plates and simulate the charged single-prong decay of

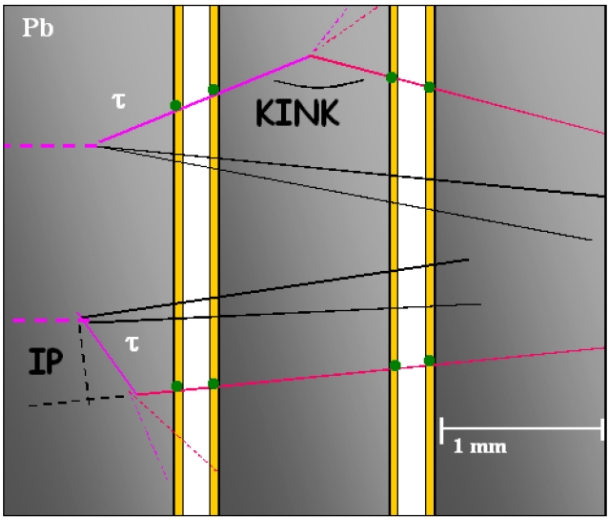

Figure 2.9: Schematic picture of the τ detection technique in the ECC structure for long (top) and short (bottom) decays.

the τ. Kinematic cuts are used to reduce this background. An important tool for background rejection is the determination of the transverse momentum of the daughter particle with respect to the direction of the τ track candidate.

For electronic τ decays the ECC technique is well suited to identify electrons and to determine their energy by measuring the density of track segments associated to their showering in the brick. For charged hadrons and muons, the momentum is deduced from the measurement of the multiple scattering in the lead plates. As discussed in the following, the muon momentum is also measured by the electronic detectors in a large fraction of the cases.

The background due to prompt ν_τ production in the primary proton target and in the beam dump is negligible. The number of interaction due to these ν_τ is estimated to be $\mathcal{O}(10^{-6}) \times N_{\mathrm{CC}} \times \varepsilon_\tau$, where N_{CC}, the total number of ν_μCC events collected, is of the order $\mathcal{O}(10^4)$ and ε_τ, the τ detection efficiency, is $\sim$10% [50, 51].

The total number of background events in 5 years of OPERA data taking is estimated to be 0.71. The contributions from the single decay channel is given in Tab. 2.2.

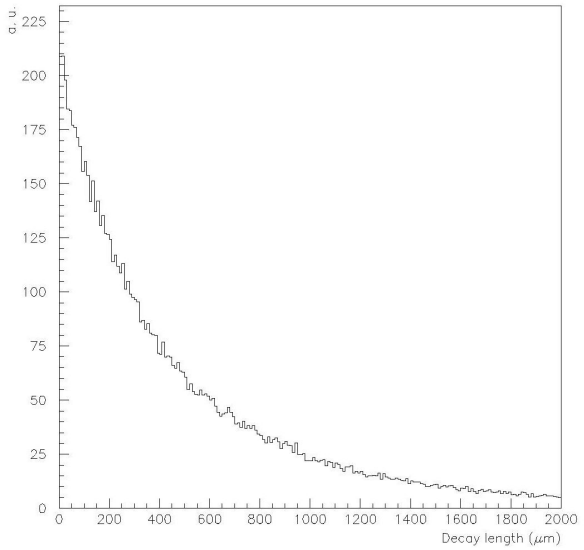

Figure 2.10: Expected τ decay length distribution.

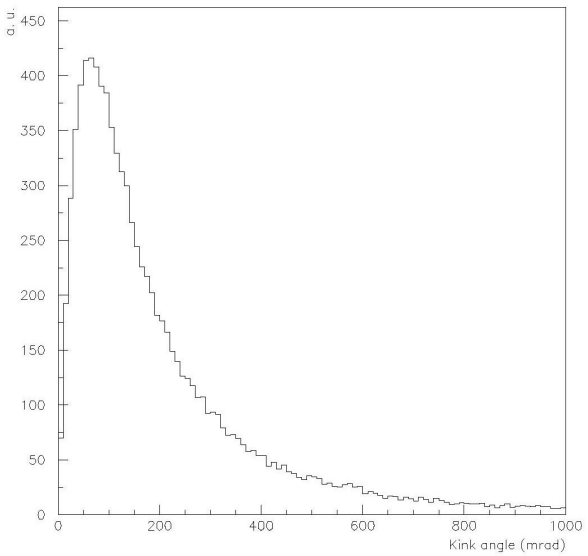

Figure 2.11: Expected τ kink angle distribution for the $\tau \rightarrow e$ decay mode.

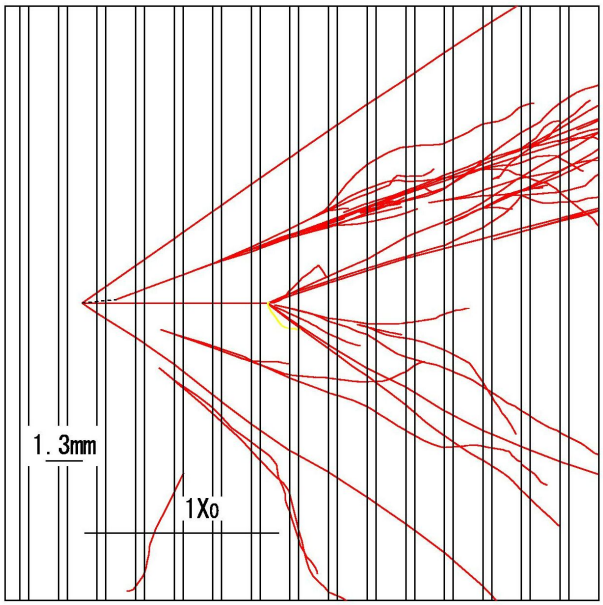

Figure 2.12: Simulated ν_τ event with τ decaying into an electron.

2.3.3 Sensitivity to $\nu_\mu \rightarrow \nu_\tau$ oscillation

The signal detection efficiency of OPERA has been estimated on the basis of tests and simulations. The latter have been tuned with data obtained in the CHORUS and DONUT experiments.

A flow diagram of the analysis chain to search for ν_τ events is shown in Fig. 2.13. The first two steps, trigger and brick finding, rely on the electronic detectors in order to select neutrino interactions and to locate the brick where the interaction took place.

The next step consists of finding the neutrino interaction vertex by scanning backward the tracks found in CS, that match the prediction of the electronic detectors, inside the emulsion sheets. After vertex finding, all tracks attached to the primary vertex are reconstructed. Particle identification as well as momentum measurements are then performed. At this point, the algorithm for electron identification is applied. A minimum amount of traversed X_0 is needed in order to have adequate momentum (energy) resolution and identification efficiency. Tracks which leave the brick from the sides or downstream having traversed an insufficient amount of material have to be

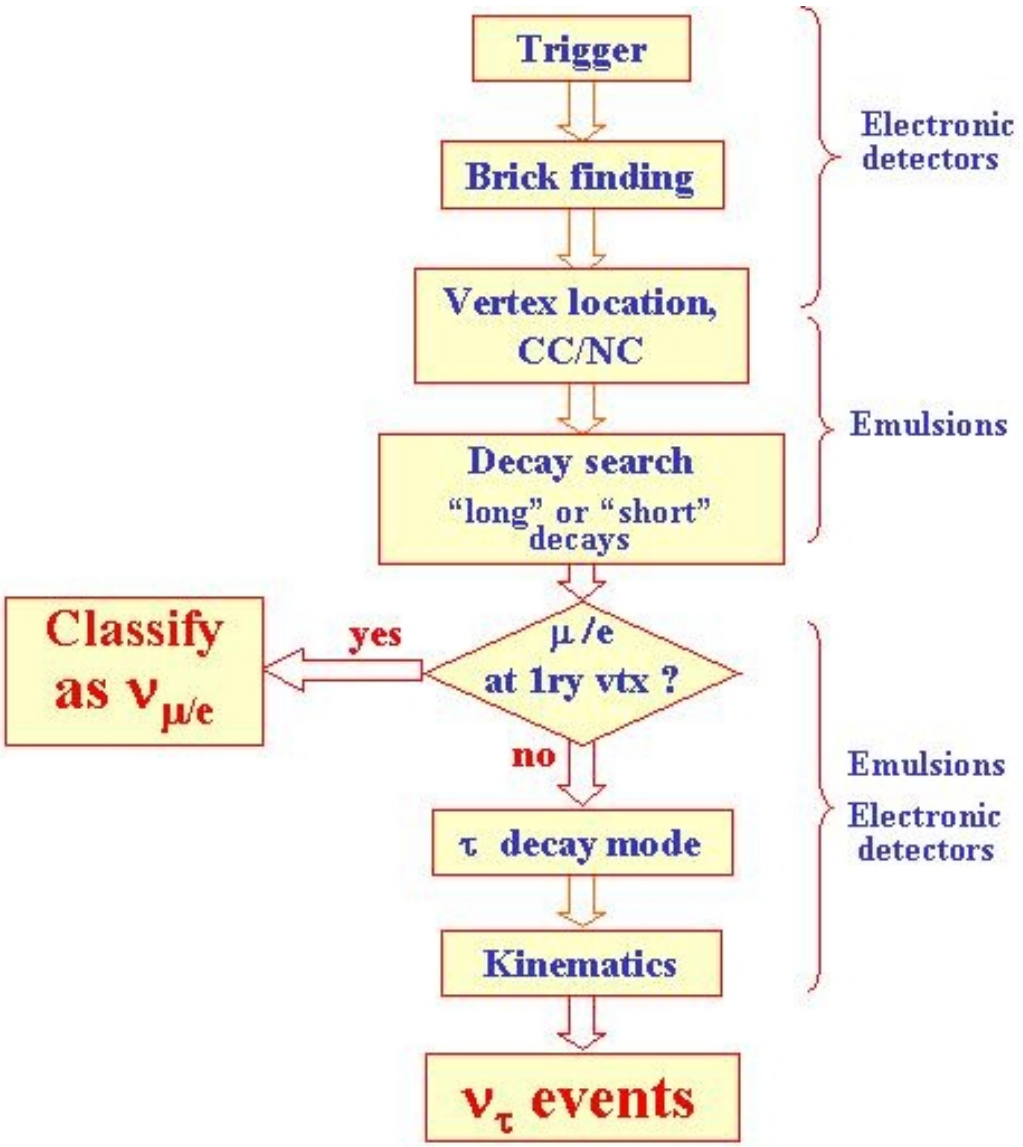

Figure 2.13: Flow diagram of the analysis chain to search for ν_τ induced events.

followed in adjacent and/or downstream bricks.

If a track attached to the primary vertex is identified as an electron or a muon, the event is classified as a CC event with charm production and

rejected, even if a kink is detected.

For events surviving the above cuts a decay search inside the *decay volume* is applied and tracks at the primary vertex are carefully measured for kinematic analysis.

All single-prong τ decay modes are used to search for the so-called long τ decays. These are events in which the τ track is long enough to exit the lead plate where the primary vertex occurs. Short decays (in which the τ track is contained within the vertex plate) are considered for the $\tau \rightarrow e$ channel.

Long decay candidates are selected by detecting a kink topology and short decays by exploiting an impact parameter method. Kinematic cuts are applied to both samples in order to enhance the signal to background ratio.

The $\tau \rightarrow e$ decay mode is identified by the distinctive energy loss of the daughter electron in the lead/emulsion brick structure. The main background to this channel is given by charm production in ν_μCC interactions undergoing electronic decay and with the primary muon escaping detection.

Muonic τ decays are characterized by an identified muon originating from the τ track kink. For these events the main background is due to large angle muon scattering in the lead plates.

Hadronic decay candidates are defined as those events in which the kink daughter particle is not identified either as an electron or a muon. In this case, charm production with subsequent hadronic decay and hadronic reinteractions in lead give a similar contribution to the background. A summary of the expected numbers of τ events in 5 years for different Δm^2 with the expected background and detection efficiencies per decay channel for OPERA is given in Tab. 2.2.

Assuming $\Delta m^2 = 2.4 \times 10^{-3}$ and maximal mixing, the probability to observe the number of events required to obtain a 4σ significance in 5 years of data taking, is 97%.

2.3.4 Search for $\nu_\mu \rightarrow \nu_e$ appearance

Sub-dominant $\nu_\mu \rightarrow \nu_e$ oscillations at the "atmospheric scale" are driven by the mixing angle θ_{13}. The angle is constrained by reactor experiments to be small ($\sin^2 2\theta_{13} < 0.1$ [24, 25]).

Due to its electron identification capability exploited for the reconstruction of the $\tau \rightarrow e$ decay, OPERA is able to perform also a $\nu_\mu \rightarrow \nu_e$ oscillation search.

channel	signal for $\Delta m^2(eV^2)$			$\varepsilon \times Br$	Background
	1.6×10^{-3}	2.5×10^{-3}	4.0×10^{-3}		
$\tau \to e$	1.6	3.9	9.9	3.4	0.16
$\tau \to \mu$	1.3	3.2	8.2	2.8	0.29
$\tau \to h$	1.4	3.2	8.2	2.9	0.20
Total	4.3	10.3	26.3	9.1	0.65

Table 2.2: Summary of the expected numbers of τ events in 5 years for different Δm^2 with the expected background and detection efficiencies per decay channel for OPERA.

In the CNGS beam the expected ν_e contamination is relatively small compared to the dominant ν_μ component ($\nu_e/\nu_\mu = 0.8\%$) and allows search for the oscillation $\nu_\mu \to \nu_e$ seeking an excess of ν_e charged current events. The systematic error associated with the ν_e contamination plays an important role for the oscillation search, the statistical fluctuation ($\sim$5%) of this component being the irreducible limiting factor.

The analysis principle is based on a search for an excess of ν_eCC events at low neutrino energies. The backgrounds are:

- the dominant $\nu_\mu \to \nu_\tau$ oscillation channel where the produced τ decays in one electron;
- ν_e beam contamination;
- the decay of neutral pions produced in NC interactions;
- ν_μ events with the primary muon not identified and with another track miming an electron.

The OPERA $\nu_\mu \leftrightarrow \nu_e$ search seeks for neutrino interactions with a candidate electron from the primary vertex with an energy than 1 GeV (to cut the soft γ component) and a visible energy smaller than 20 GeV (to reduce the background due to the prompt component). Moreover, a cut on the number of grains associated with the track of the candidate electron is also applied. The latter has a strong impact on the reduction of the background from ν_μCC and ν_μNC events and allowed for a softer cut on electron energy. Finally, a cut on missing p_T of the event is applied ($p_T < 1.5$ GeV) to further reduce NC contamination and suppress $\tau \to e$ background.

θ_{13}	$\sin^2 2\theta_{13}$	ν_eCC signal	$\tau \to e$	ν_μCC $\to \nu_\mu$NC	ν_μNC	ν_eCC beam
9^0	0.095	9.3	4.5	1.0	5.2	18
8^0	0.076	7.4	4.5	1.0	5.2	18
7^0	0.058	5.8	4.6	1.0	5.2	18
5^0	0.030	3.0	4.6	1.0	5.2	18
3^0	0.011	1.2	4.7	1.0	5.2	18

Table 2.3: Expected number of signal and background events in the $\nu_\mu \to \nu_e$ oscillation search, assuming $\Delta m^2_{23} = 2.5 \times 10^{-3}$ eV^2 and $\theta_{23} = 45^0$ for 5 years of OPERA data taking.

The expected number of signal and background events for OPERA assuming 5 years data taking with the nominal CNGS beam is given in Tab. 2.3 for different values of θ_{13}. The 90% confidence level limit for the OPERA experiment is $\sin^2 2\theta_{13} < 0.06$.

An increase of the sensitivity to $\nu_\mu \to \nu_e$ can be obtained by fitting the kinematic distributions of the selected events.

In order to disentangle $\nu_\mu \to \nu_e$ and $\nu_\mu \to \nu_\tau$ oscillations, the transverse missing momentum distribution was exploited. The $\nu_\mu \to \nu_e$ are balanced, while $\nu_\mu \to \nu_\tau$ show a sizable transverse momentum due to the presence of neutrino(s) in the final state. The visible energy and the missing transverse momentum are combined into a binned-fitted χ^2-fit, in which the three oscillation parameters are allowed to vary. By fitting simultaneously the E_{vis}, E_e, P_T^{miss} distributions, it is obtained the 90%CL exclusion plot shown in Fig. 2.14 under the assumption $\theta_{23} = 45^0$. The OPERA P_T^{miss} distributions for signal and background channels are shown in Fig. 2.15 [46].

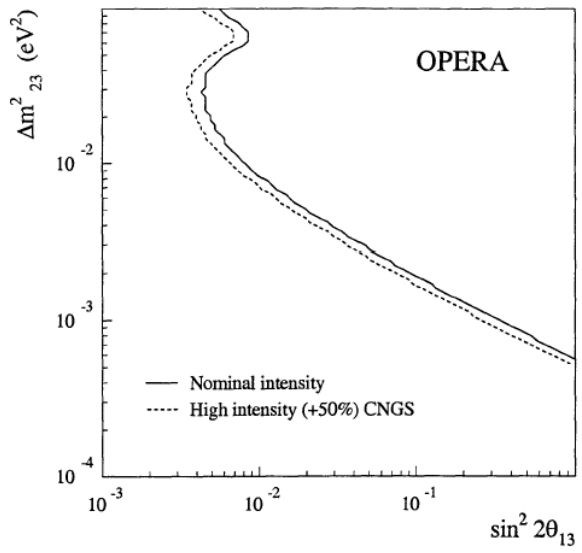

Figure 2.14: OPERA sensitivity to the parameter θ_{13} at 90% C.L. in the three family mixing scenario, in the presence of while $\nu_\mu \rightarrow \nu_\tau$ with $\theta_{23} = 45^0$.

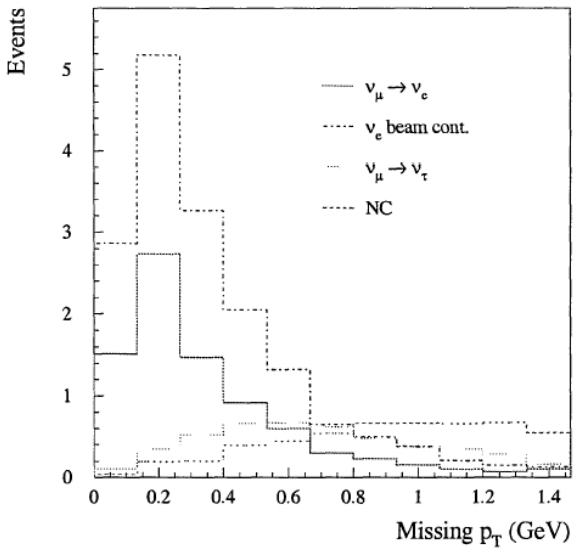

Figure 2.15: p_T^{miss} distribution for the $\nu_\mu \rightarrow \nu_e$ signal and for the background channels assuming $\theta_{13} = 8^0$, $\Delta m^2_{23} = 2.5 \times 10^{-3}$ eV^2 and $\theta_{23} = 45^0$.

Chapter 3

Nuclear emulsions and automatic scanning system

Nuclear emulsions provide very high position resolution, smaller than 1 μm and truly three-dimensional information. This makes them particularly suitable to detect short lived particles. As described in Par. 2.2 and 2.3, the OPERA experiment will use a massive nuclear emulsion detector to identify τ leptons through the direct detection of their decay topology. The feasibility of experiments such as OPERA using a large mass emulsion detector is linked to the impressive progress under way in the development of automatic emulsion analysis. R&D programs are going on in the laboratories of the Collaboration for a new generation of scanning systems with high accuracy and high speed. Recent improvements and preliminary results, using new prototype systems are briefly reported.

3.1 Nuclear emulsions

The use of photographic emulsions to study nuclear particles began in 1896, when H. Becquerel for the first time observed a blackening of photo-plates in contact with salts of uranium. The development of the nuclear emulsion method for recording high-energy charged particles involved many physicists worldwide during the 1930s [52]. The real breakthrough was made in 1946, when an industrial chemist, C.Waller, produced the first "concentrated" emulsions, with a halide/gelatin ratio higher than previously used, sensitive enough to make the tracks of mesons visible for the first time: in

1947 the pion was discovered by observing the $\pi \rightarrow \mu \rightarrow e$ decay chain in nuclear emulsions exposed to cosmic rays [53]. In the following years, several particles such as the K mesons and hyperons were observed using emulsion detectors. In the 1960s accelerators started to replace cosmic rays as sources of high-energy particles, and fast-response detectors, such as counters and spark chambers, started to replace cloud chambers and nuclear emulsions. Anyway, nuclear emulsions were not abandoned, because of their unique peculiarities: they are very sensitive and allow to resolve particle tracks to less than 1 μm, and therefore the ideal device to detect short-lived particles.

The development of automatized scanning systems during the last two decades has made possible the use of large nuclear emulsion detectors. Indeed, nuclear emulsions are still successfully used nowadays, especially in neutrino experiments: for example experiments like WA17 at CERN [54], aiming at the search for charmed particles in neutrino charged current interactions, or E531 at Fermilab [55], aiming at the measurement of charmed particle lifetimes in neutrino interactions, or WA75 at CERN [56], searching for beauty particle production induced by a 350 GeV/c π^- beam. Furthermore, the use of nuclear emulsion allowed the first (and still unique) detection of ν_τ neutrinos by the DONUT collaboration [6]. The neutrino experiment CHORUS at CERN used a large amount of nuclear emulsion as target and tracking detectors [57].

Nuclear emulsions are made of micro-crystals of silver halides (AgBr) dispersed in a gelatin layer. The energy released by ionizing particles to the crystals produces a *latent image* which is almost stable in time. A chemical development process reduces the irradiated grains to metallic Ag. After fixing and washing to remove undeveloped crystals, the paths of an ionizing particle is visible as a sequence of black silver grains (Fig. 3.1).

Nuclear emulsions are basically the same as general purpose photographic emulsions, but have several distinguishing features: the silver halide crystals are very uniform in size and sensitivity, which allow to detect tracks with good efficiency; the silver to gelatin ratio is much higher than in a conventional emulsions; they are thicker.

The grain density along a track of a particle of well-known charge and velocity depends on the sensitivity of the emulsion and on the development process. The ionization curve must be calibrated. Presently nuclear emulsions can be produced with well controlled composition (concentration of crystals - normally $20 \div 50\%$ in volume, enrichment with particular elements,

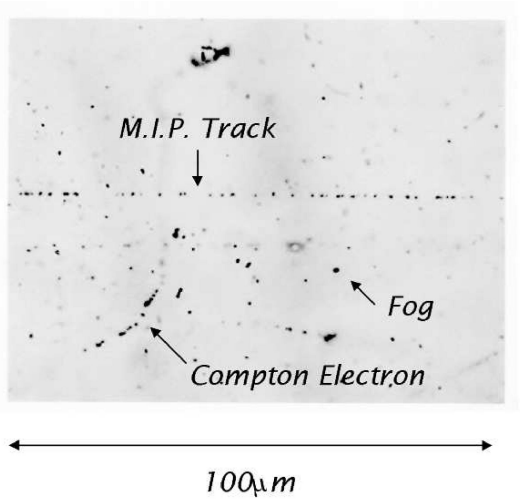

Figure 3.1: Photograph of a minimum ionizing particle recorded in emulsion.

etc.). A minimum ionizing particle (mip) yields ≃30 grains per 100 μm with a diameter of about 0.6 μm. An intrinsic resolution of 0.06 μm can be achieved measuring the grain centers. Three-dimensional tracks are observed under high magnification optical microscopes. The precision of the measurement depends on the quality of the set-up and on the corrections which have to be applied. The use of emulsions as quantitative device is difficult: the correct measurement requires an exact knowledge of the instrument itself.

3.1.1 OPERA emulsion films

The total area of emulsion films in the OPERA detector is $\simeq$ 150000 m^2. This quantity is a few orders of magnitude larger than all the ones used by previous experiments. This makes the emulsion pouring by hand impossible (as was always done in the past). To overcome this problem, an automatic procedure for the OPERA nuclear emulsion production has been performed by the Fuji Film company following an R&D in collaboration with Nagoya University.

Fig. 3.2 shows a photograph of the cross section of an OPERA emulsion film taken by an electronic microscope. Two emulsion layers of 42 μm are coated on both sides of a 210 μm thick triacetate base. A thin ($\approx$ 1 μm) protective film (gelatin) is placed over both emulsion layers in order to prevent

the occurrence of black patterns, due to silver chemically deposited during the development. In addition, the presence of this protective layer allows to place emulsions in direct contact with lead plates.

Unlike hand-made films, the thickness of the emulsion layer can be precisely controlled as in the case of commercial color films.

The crystal diameter distribution is rather uniform around 0.2 μm (see Fig. 3.3). The emulsion sensitivity, *i.e.* the grain density along a mip track, is $30 \div 35$ grains/100 μm. Several measurements performed with high-energy π beam have confirmed this value. The fog due to accidentally developed grains is randomly distributed in the emulsion volume and is at the level of ≤ 5 fog grains/1000 μm^3. This value smoothly depends on the chemical development and the refreshing procedure. In the following some of the physics properties of our emulsions are reported:

- density $\rho = 2.4$ g/cm^3,
- average atomic number $\langle A \rangle = 18.2$,
- average atomic charge $\langle Z \rangle = 8.9$,
- radiation length $X_0 = 5.5$ cm,
- $(dE/dx)_{mip} = 1.55$ MeV/g/cm^2 or 37 keV/100 μm,
- nuclear collision length $\lambda_T = 33$ cm.

3.1.2 Production, refreshing and development

The total number of emulsion sheets needed for the experiment is about 12 millions. The production started in Japan by Fuji Photo Film Company on April 2003 and 4.3 million sheets have already been produced.

Due to their continuous sensitivity, the emulsion sheets collect latent track images, mainly from cosmic-rays and ambient radioactivity, from the beginning of their life at the Fuji production firm to the installation in the OPERA detector in the Gran Sasso Underground Laboratory. All tracks not related to an event induced by the CNGS beam are to be considered as background. The background tracks increase the scanning time, affect the pattern recognition and may cause a degradation of the measurement of the energy of

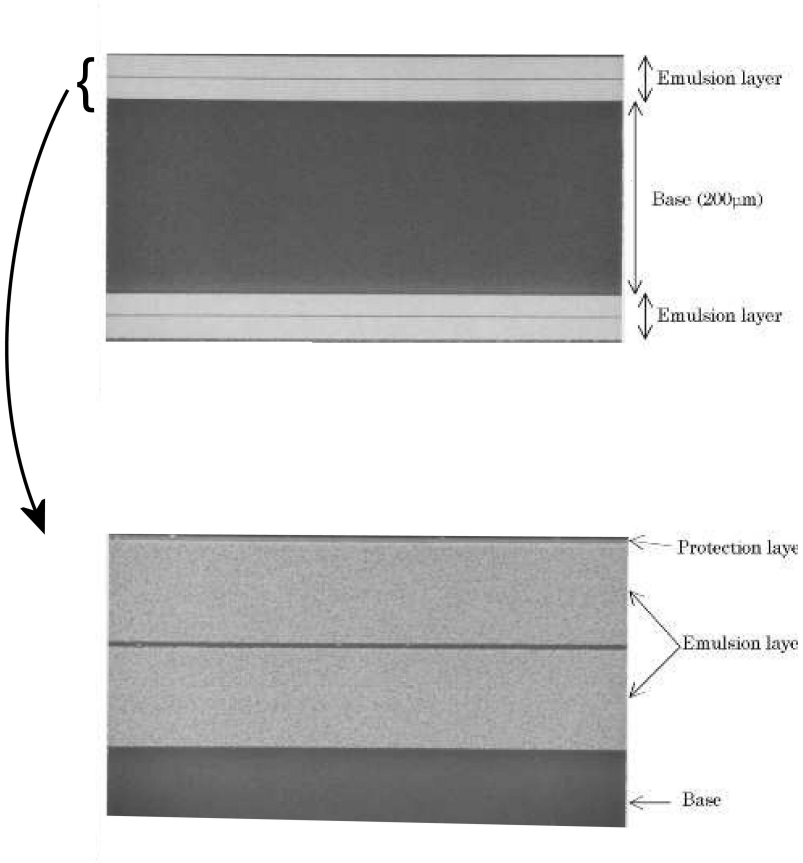

Figure 3.2: Top: photograph of the cross section of a machine-coated emulsion film taken with an electronic microscope. Diluted emulsion layers of 42 μm thickness are coated on both sides of a 210 μm thick triacetate base. Bottom: enlarged view of the top emulsion layer. A thin ($\sim$ 1 μm) protective film (gelatin) is placed over the emulsion layer at the same time of coating.

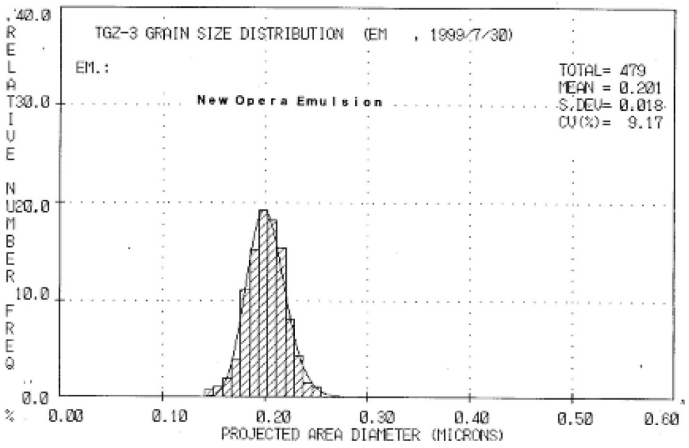

Figure 3.3: Crystal diameter of the Fuji emulsion produced for the OPERA experiment.

electromagnetic showers. A remedy was proposed and successfully tested at Nagoya University: a treatment of the emulsion sheets at moderate temperature and very high humidity for a few days cancels most of the previously stored latent track images (∼96%). This is known as *refreshing* procedure. After production, the OPERA emulsions are stored in the Tono mine, in Japan, where, at the depth of 96 m, a refreshing facility has been set up. Emulsions are stored for three days at 30 ^{0}C and 98% relative humidity. The refreshing procedure affects minimally the sensitivity and the fog density of the emulsions. After shipment to the Gran Sasso Underground Laboratory, a refreshing procedure is foreseen only for the Changeable Sheets, since they must guide the back-scanning in the brick, as described in Par. 3.3.

The development procedure is a many-step chemical treatment in a dark-room, lasting about 3 hours. This process is very complex and involves a considerable number of steps in order to reduce completely those crystals containing a latent image center and leave unchanged those not containing a center. In practice, a certain number of crystals will be developed even though they do not contain a development center. These grains, when developed, constitute what is known as fog or background. After the development, a fixation procedure must be made in order to remove all the residual silver halides. These, if otherwise left in the emulsion, would slowly induce the browning and degrading of the image. Finally the emulsions must be washed

very thoroughly to remove all the complexes used in the previous phases: if any remains, it would eventually obscure the image.

The possibility of obtaining sub-micrometric tracking precision is strictly linked to the stability of grain relative positions inside the emulsion volume during and after the development. Two main deformation effects have to be taken into account, the *shrinkage* and the *distortion*:

- the shrinkage effect is due to a reduction of the thickness of the emulsion sheet after the development process. The shrinkage factor is defined as the emulsion thickness at the time of exposure divided by the thickness after the development. This factor must be taken into account by the tracking algorithm, because the measured micro-track slopes must be multiplied by this factor to obtain the real value. This effect is sketched in Fig. 3.4;

- the distortion is a local deformation of the surface of the emulsion, which may limit the measurement precision. A typical distortion map measured in an OPERA emulsion is shown in Fig. 3.5. The arrows indicate the distortion direction. The absolute value of the distortion is indicated by the length of the arrow. The average value of the measured distortions is $\sim$5 mrad. The use of double-sided emulsions coated on a plastic support plate improves the angular resolution at a level of 2 mrad, because the track direction can be defined by the two points near the support plate, which are practically free of distortion.

3.2 Automatic scanning system

An automatized system for emulsion analysis consists of a microscope with motorized stage, a dedicated optical system, a CCD camera and a computer with a frame grabber, a vision processor board and a motor control board.

The emulsion scan is done by microscopes with a vertical resolution of a few microns: the three dimensional structure of the tracks is reconstructed by raising or lowering the best focus plane of the objective in order to span the whole emulsion thickness.

The first fully automated system, the *Track Selector* (TS), was developed at the University of Nagoya [58]. The TS and its improved version, the Ultra

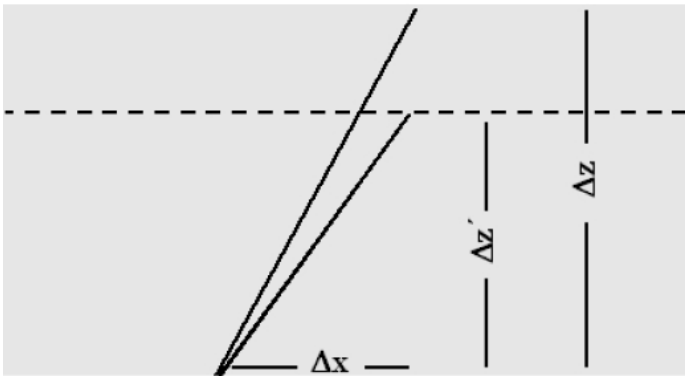

Figure 3.4: The shrinkage effect: the measured track slope $\Delta z'/\Delta x$ does not coincide with the real slope $\Delta z/\Delta x$. The shrinkage correction is obtained by multiplying the measured slope by the shrinkage factor $\Delta z/\Delta z'$.

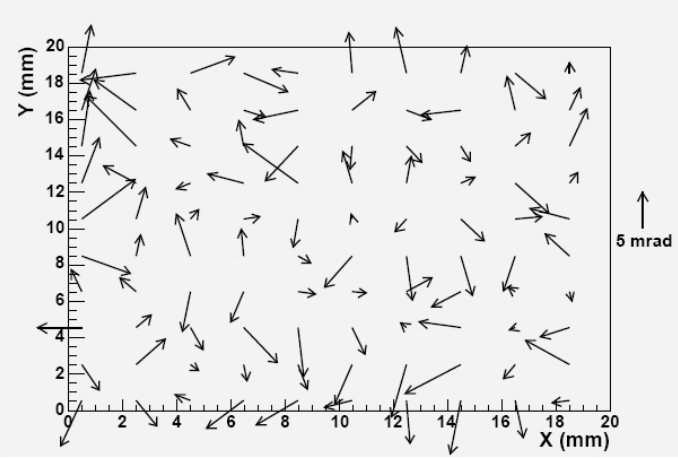

Figure 3.5: A typical distortion map of an OPERA nuclear emulsion.

Track Selector (UTS) [59], have been successfully used in the CHORUS [57] and DONUT [6] experiments. The UTS is able to scan emulsions with a maximum speed of about 2 cm^2/h.

OPERA requires an improvement of a factor of ten in speed, *i.e.* a speed of about 20 cm^2/h. To achieve this goal, two different R&D programs are carried out:

- The Nagoya University group aims to a further improvement of the UTS system, the *Super-UTS*.
- The European laboratories of the OPERA collaboration worked together to the realization of an European Scanning System [60]. The R&D was based on a previous work done by the Salerno and Napoli groups with the SySal (Salerno System) track reconstruction system for the CHORUS experiment [61].

3.2.1 The European Scanning System

The guidelines followed in the realization of the European Scanning System are the use of the *state-of-art* of commercial products for hardware components and a strong software dependency, to provide the flexibility needed to easily upgrade the system following the quick technological progress. The design takes into account besides the request of a high scanning speed also position and angular accuracies adequate for event analysis.

The system was conceived with the following features:

- high-performance mechanics with sub-micrometric position accuracy and very small settling-time;
- optics with a large field of view (360×280 μm^2), 50X magnification to have $\sim$4 pixels for an object of the order of 0.8 μm (the size of processed grain) and a working distance of 0.4 mm (to cover the whole thickness of an emulsion film);
- camera 1280×1024 pixels (1 pixel $\sim$0.28 $\times$0.28 μm^2) and high frame rate;
- powerful image processors;
- high software flexibility.

The working principle of the European Scanning System is based on the possibility to reconstruct all tracks in each field of view regardless of their slope by measuring the spatial position of the developed grains along their trajectories.

By lowering the best focus plane of the objective, the whole emulsion thickness is spanned and digitized images, corresponding to the pixels mask

of the camera, are taken at different depth (every $2 \div 3$ μm) inside each emulsion layer (see Fig. 3.6). These raw images are processed using a high-pass digital filter to enhance the contrast between pixels that are images of focused grains and pixels darkened by not-in-focus grains or electronic noise.

A threshold is applied to select the pixels that are candidates to become clusters. It is worth to distinguish between a grain, a physical object in the emulsion, and a cluster, that is the digitized images of a grain.

After the morphological information of the clusters (position, area, ...) have been calculated, the next processing step uses these information to recognize geometrical alignments between clusters of different layers in order to form to so-called *micro-tracks*. All these operations are performed in real time according to the time needed for the image processing and the movement of the mechanics (settling time).

The data acquisition software for the emulsion automatic scanning and track segments reconstruction is developed on a Windows platform by using the object-oriented C++ language. The scanning output is a collection of raw data files (in binary format) which contain information related to the detected micro-tracks plus some general information related to the acquisition process.

The automatic scanning system presently working in the Bologna laboratory is shown in Fig. 3.7. In 2004 it reached the desired scanning speed of 20 cm^2/h.

3.3 Scanning procedure of the OPERA emulsions

The scanning procedure of the OPERA emulsions will consist of the following steps:

- **Changeable sheet analysis**
  Once the brick finding algorithm recognizes the most probable brick where the neutrino interaction took place, it is extracted by the brick manipulator system; the related CS is detached and analyzed. The scanning procedure is the so-called *general scanning*: all tracks with any angle are read out within the scanned area. Electronic detectors predict the position of the neutrino interaction vertex inside the brick

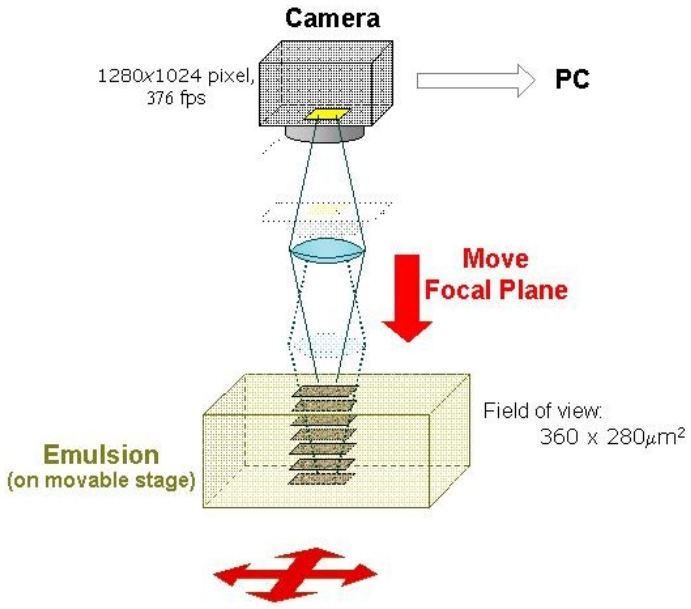

Figure 3.6: The readout: several images are taken at different focal depths.

with about 1 cm accuracy for CC events while for NC ones the hadron track accuracy does not allow to provide any position prediction within the brick. Unlike hadron tracks, the muon angle can be reconstructed with an accuracy of a few tens of mrad and therefore the muon angular information can be used to constrain track candidates in the CS.

- **Scan back**
  If the neutrino interaction is confirmed by the CS analysis, the brick is exposed to cosmic rays for sheet to sheet alignment, developed and sent to the OPERA scanning laboratories for the analysis. In the case of no interaction confirmation, the brick, with a new attached CS, is relocated in the detector and, eventually, another brick can be removed. Starting from the most downstream emulsion sheet (the nearest to the CS), the tracks found in the CS are followed upstream from sheet to sheet until they stop, *i.e.* they are generated from a vertex in the next upstream lead plate or make a large angle scattering. The lead plate downstream of the first emulsion sheet where the track disappeared is defined as the vertex plate. This procedure of track following is called

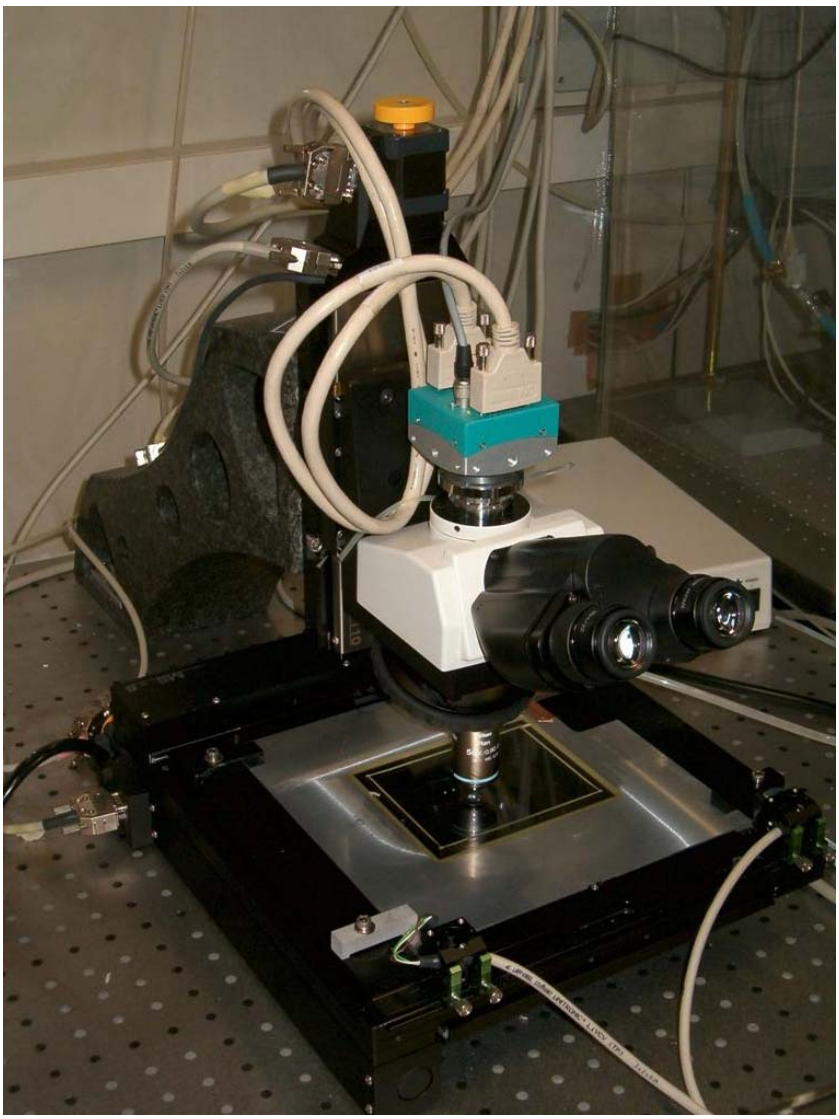

Figure 3.7: A photograph of the prototype automatic scanning system for emulsions realized in the Bologna laboratory.

Scan Back. The scanning is performed in an area determined by the accuracy of the predicted position. Track segments are searched for in an angular range limited by the prediction angular accuracy and by the possible distortion of the emulsion layers. A 3×3 mm^2 area is needed

for each track in the first emulsion layer, as the mechanical alignment between the CS and the brick is about 1 mm. In the following emulsion sheets, data taking of a single field of view of (360×280 μm^2) for each track is sufficient, since the intercalibration done by means of passing through cosmic rays allows a precision of $10 \div 20$ μm.

- **Vertex reconstruction**
  Once the neutrino vertex position is found, 10 sheets are used (2 upstream of the lead plate and 8 downstream) for vertex confirmation and study. A 5×5 mm^2 general scanning area is needed for this purpose. Secondary vertices (decays) are searched for, reconstructed and checked for their compatibility with the decay topology. All the information on tracks and vertices will be stored and subsequently used by dedicated analysis tools, aiming at particle identification, momentum or energy measurement and shower reconstruction.

3.4 Event reconstruction in the emulsion

The on-line DAQ is aimed at the micro-track reconstruction, as described in the previous section. The track reconstruction is performed by an off-line analysis tool in several steps:

- micro-track linking (or base-track reconstruction);
- emulsion sheet intercalibration;
- volume-track reconstruction.

A *base-track* is built by connecting two micro-tracks that cross the plastic base, and a *volume-track* is constructed from two or more base-tracks, each one in a different emulsion sheet; thus we reconstruct the trajectory of a particle transversing an ECC brick.

The off-line reconstruction tool used in our analysis is FEDRA (Framework for Emulsion Data Reconstruction and Analysis), an object-oriented tool based on C++ language and developed in the ROOT[1] frame-work [62].

For the study of the performances of the automatic scanning system, in June 2004 a brick was exposed to a high intensity pion beam at the CERN

[1] http://root.cern.ch

PS, that can provide high momentum particles (up to 10 GeV/c). The beam energy was set to 10 GeV in order to minimize multiple Coulomb scattering. The momentum resolution was about 1%. The electron contamination was measured to be ∼1% and the muon contamination ≤ 10%. To provide an unbiased evaluation of the base-track reconstruction efficiency and the position and angle resolutions, a brick without lead was assembled. The brick was exposed to different angles in order to determine the performances of the system over all the angles of interest. For each angle position, the trigger density was ∼2 particles/mm^2. Fig. 3.8 shows the angular spectrum of the tracks impinging on the brick measured with the Bologna automatic microscope.

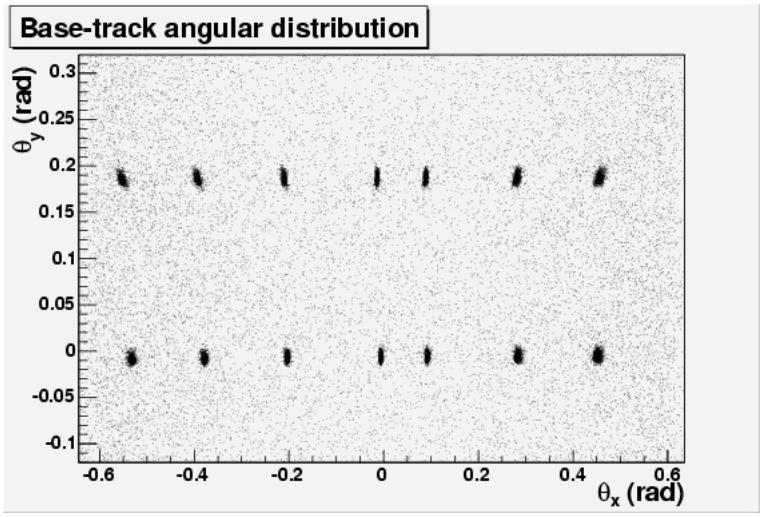

Figure 3.8: Angular spectrum of the tracks used for the measurement of the microscope performances. The peculiar peak shape is due to the representation in the plane (θ_x, θ_y).

3.4.1 Micro-track linking

In the general scanning mode all micro-tracks within a given angular range are searched for, while in the scan back mode, only well defined positions and angular areas are investigated. In any case, two micro-tracks found in the two emulsion layers are connected to form a base-track if they are within the expected angle and position resolutions.

The base-track reconstruction is performed by projecting micro-track pairs across the plastic base and searching for an agreement within given slope and position tolerances (Fig. 3.9).

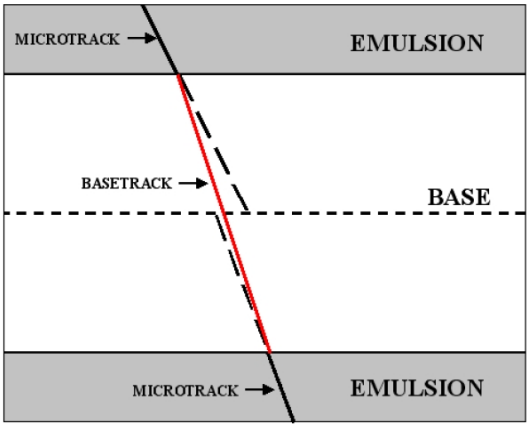

Figure 3.9: The principle of base-track reconstruction: the micro-tracks matching is obtained when an acceptable agreement in slope and position is found. The base-track is formed by joining the two points closer to the base.

The micro-track slopes are used only to define the angular agreement, while the base-track is defined by joining the points of intersection of the micro-tracks with the measured surface of the plastic base. A micro-track is defined by a series of aligned clusters. A cluster is the digitized image of a grain, whose depth in the emulsion is randomly distributed and is affected by the vertical resolution of the microscope ($\sim$2.5 μm). So, the micro-track resolution, defined as the angular difference between a micro-track and a base-track, is affected by this value. Since the points used for the base-track definition lie in the surface between the emulsion and the plastic base, they are almost unaffected by distortion effects: the base-track has an angular resolution approximatively one order of magnitude better than the micro-tracks. However, good micro-track resolution allows to keep the background due to casual match low. Fig. 3.10 shows the obtained resolution both in angle and in position.

The base-tracks are selected on the base of a quality estimator of the

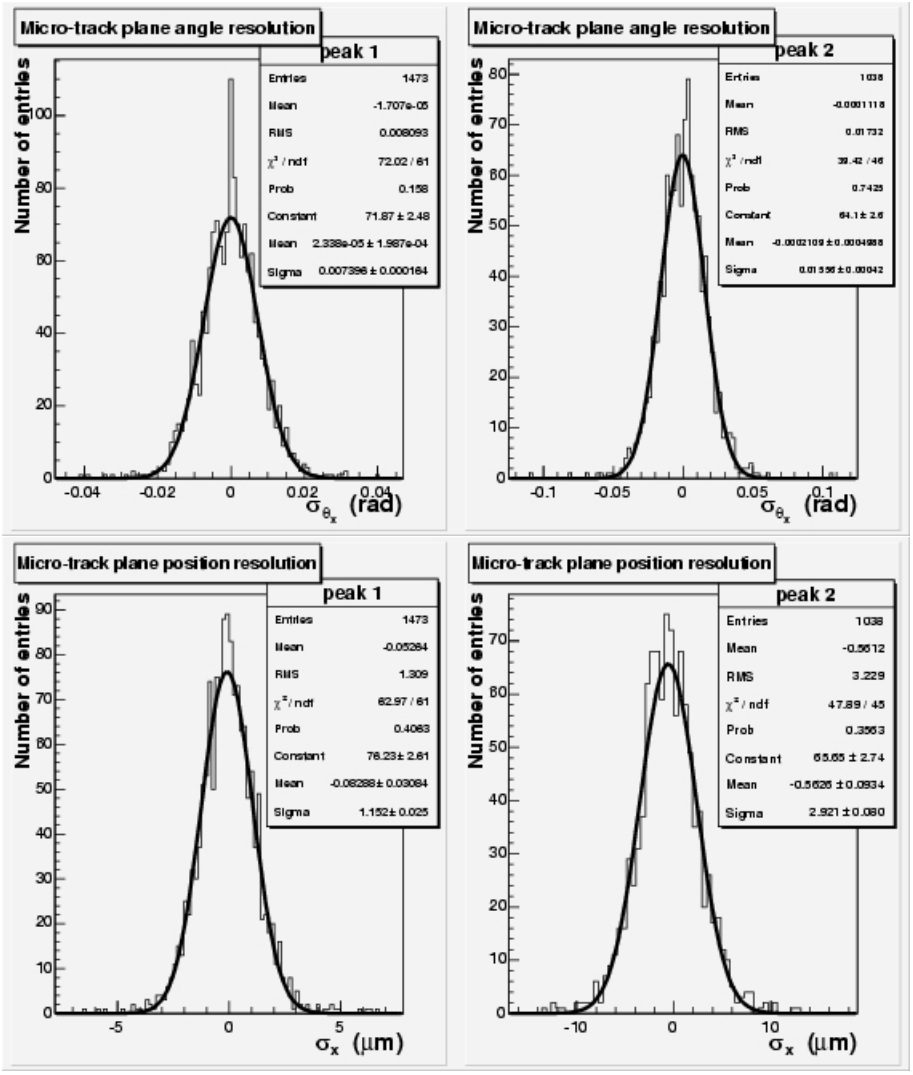

Figure 3.10: Micro-tracks plane resolution of the angle (top) and position (bottom) for two different angles: 0 mrad (left) and 400 mrad (right).

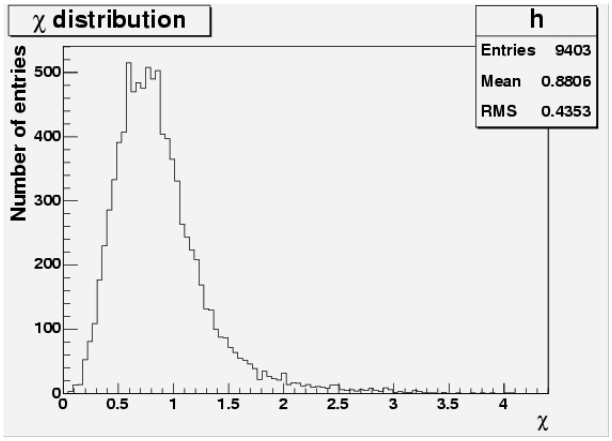

Figure 3.11: Base-track χ distribution for the signal inside 5σ around the central peak position in angular space.

micro-track angular agreement, χ^2, defined as

$$\chi^2 \equiv \frac{1}{4}\left[\frac{(S_{x_t}-S_{x_B})^2}{\sigma^2_{S_x}}+\frac{(S_{x_b}-S_{x_B})^2}{\sigma^2_{S_x}}+\frac{(S_{y_t}-S_{y_B})^2}{\sigma^2_{S_y}}+\frac{(S_{y_b}-S_{y_B})^2}{\sigma^2_{S_y}}\right] \quad (3.1)$$

where S_x and S_y are, respectively, the x and y slopes and σ_{S_x,S_y} are the micro-track angular resolutions. The under-script t (b) refers to top (bottom) micro-track, while B to base-track.

The name of this quantity is a little misleading since this definition is not a pure χ^2: the variables used in its construction are not independent but are correlated two by two. Moreover, the reconstruction program uses $\sqrt{\chi^2}$ instead of χ^2 as signal/background separator. So in the following we will refer always to χ.

A typical χ distribution is shown in Fig. 3.11. In order to discard as much background base-tracks as possible and minimize the signal loss, the cut

$$\chi < 3.5 \quad (3.2)$$

is applied in the measurements reported in the following of the Paragraph.

3.4.2 Emulsion sheet intercalibration

In the OPERA standard operation, a brick extracted from the detector is exposed to cosmic rays for the alignment before the unpacking. In an ex-

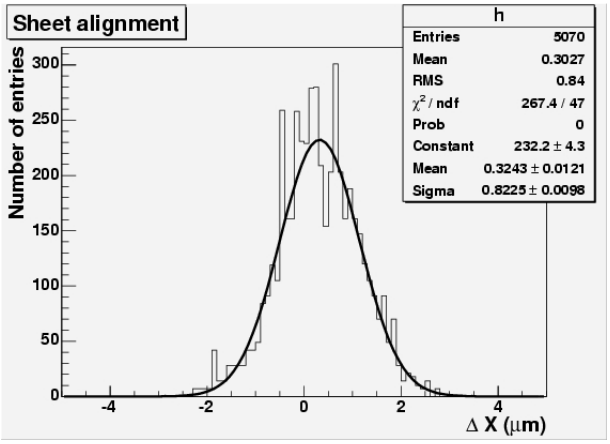

Figure 3.12: The difference of base-track position in two adjacent emulsion sheets.

perimental test, during which bricks are exposed to high density beams, no cosmic ray exposure is needed as the beam particles themselves can be used for the alignment. This is the case of the brick we are analyzing.

The emulsion sheet intercalibration is done by subdividing the emulsion sheets in several cells and applying some relative displacements. The right translation will maximize the number of track coincidences. The alignment between two sheets is described by an affine transformation, defined as

$$\begin{pmatrix} x \\ y \end{pmatrix} = \begin{pmatrix} a_{11} & a_{12} \\ a_{21} & a_{22} \end{pmatrix} \begin{pmatrix} x \\ y \end{pmatrix} + \begin{pmatrix} b_1 \\ b_2 \end{pmatrix} \tag{3.3}$$

The use of a large quantity of *passing through* volume-tracks allows to determine the relative displacements at sub-micrometric level. Fig. 3.12 shows the distribution of the differences of track positions in adjacent emulsion sheets. The average of the distribution corresponds to the error on the sheet intercalibration. The measured value is less than 1 μm.

3.4.3 Volume-track reconstruction

The algorithm used for track reconstruction is essentially based on finding and fitting a sequence (chain) of base-tracks. The basic principle consists in building base-track pairs, trying to extend the pairs in both directions inside

the brick and building base-track chains. The chain is interrupted when a decay or an interaction vertex is found, or by the inefficiencies of the base-track finding algorithm. A merging procedure of tracks recovers such inefficiencies. The track fitting is based on the Kalman filtering algorithm [63].

In the analysis of this thesis no merge procedure has been used since a new algorithm for shower reconstruction has been developed.

Once volume-tracks have been constructed, the base-track angular resolution, σ_θ, can be evaluated. It is obtained by studying the angular residuals of two consecutive base-tracks belonging to the same volume-track. The obtained resolution is shown in Fig. 3.13 (top). For vertical tracks the angle resolution is 1.5 mrad; this corresponds to the microscope resolution since there were no lead plates between consecutive emulsion sheets. The base-track angular resolution is well approximated by the empirical relation

$$\sigma_B(\theta_{x,y}) = \sigma_B(0)(1 + 4 \cdot \theta_{x,y}) \ , \quad \sigma_B(0) = 1.5 \text{ mrad}. \tag{3.4}$$

In Fig. 3.13 bottom, the position resolution, σ_r, as a function of the base-track angle is shown. It would be expected that $\sigma_r = \sigma_\theta \times d$, where d is the distance of two consecutive emulsion sheets. In our case, an OPERA brick without lead plates, $d = 300$ μm, hence $\sigma_r \simeq 0.45$ μm. For vertical track we find $\sim$1.5 μm. This discrepancy is explained by considering the sheet intercalibration accuracy that is of the order of 1 μm. It is worth to note that sheet-to-sheet alignment does not affect the angle resolution.

3.5 Performances and resolutions

The performances of a scanning system are also specified by the scanning speed, the tracking efficiency and the tracking purity, besides the position and angle resolutions described in the previous Paragraph. In the following of this Paragraph a measurement of the base-track reconstruction efficiency and of the instrumental background is reported.

3.5.1 Base-track reconstruction efficiency

The evaluation of the base-track reconstruction efficiency, ε_{bt}, is based on the reconstruction of volume-tracks passing through an OPERA-like brick.

For each emulsion sheet, ε_{bt} has been defined as the number of passing through volume-tracks that "hit" that sheet with respect to the total number

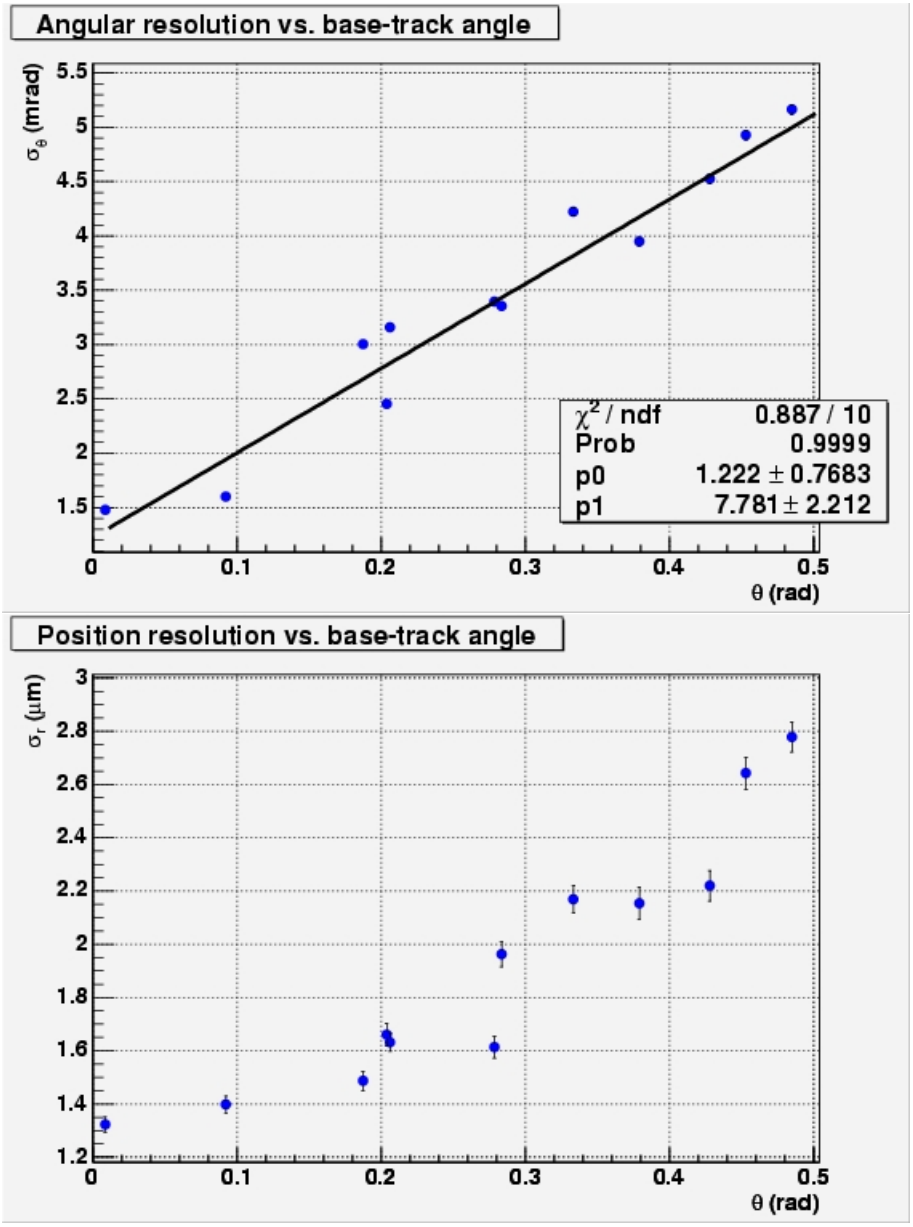

Figure 3.13: Top: angular resolution as a function of fit base-track angle. Bottom: position resolution as a function of fit base-track angle.

of passing through tracks. It is independent of the number of emulsion sheets used for the definition of the volume-track sample, provided the number of sheets is large enough to avoid that the volume-track sample includes tracks due to random coincidences or to tracks that are not mip. The obtained efficiencies and their errors are shown in Fig. 3.14 as a function of the spatial base-track angle θ. This peculiar behavior is due to the average number of clusters as a function of base-track angle. Fig. 3.15 shows that the average cluster number has a minimum for $\theta \simeq 0.250$ mrad, in correspondence with the minimum of the efficiency. Vertical base-tracks have a large number of clusters since each grain is reinforced by its shadow; 400 mrad base-tracks have on average a large number of clusters because of their longer path in emulsion.

3.5.2 Background

Two different background sources need to be accounted for. The *instrumental* background is due to random coincidences of two micro-tracks generated by the random combination of fog grains. The *physical* background comes from any physical source different from the neutrino interaction (*i.e.* cosmic rays not completely erased after refreshing, lead or environmental radioactivity). Here the performances of the automatic scanning system are described, so only the instrumental background will be considered. The physical background in the shower analysis will be discussed in Chap. 5.

The evaluation of the instrumental background has to be done by visual inspection, since only the human eye check can confirm whether the found track is due to instrumental background rather than to a physical source. The background measurement is performed by using emulsions developed immediately after the end of their refreshing.

The χ cut, defined in Eq. 3.2, brings to a background density of $\sim$3.4 base-tracks/mm^2 within $|\theta| < 0.4$ rad. This value is too high for a visual inspection. A more stringent selection criterion, that affects marginally the base-track reconstruction efficiency while suppressing largely the background, is needed. Since there is a correlation between the number of clusters and χ for "good" base-tracks, a cut in the (χ, n_c) plane has been defined. Fig. 3.16 shows the χ distribution as a function of n_c for the base-tracks linked in one emulsion sheet. The selection criterion is defined as

$$\chi < 0.25 \cdot n_c - 3 \tag{3.5}$$

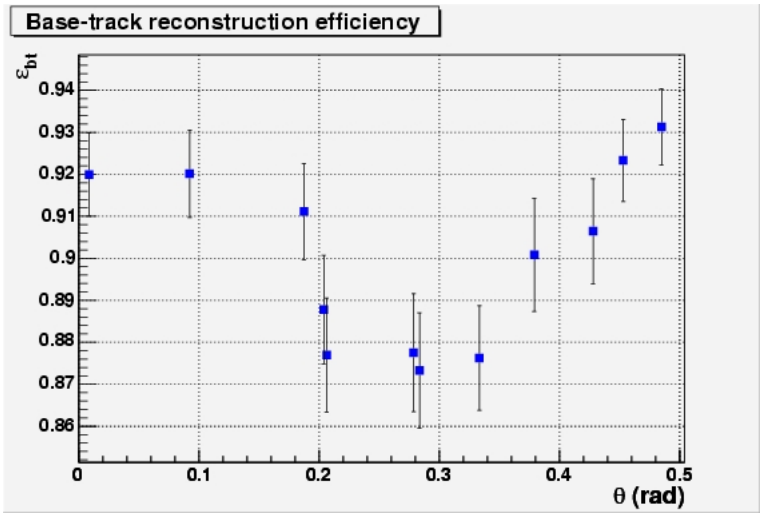

Figure 3.14: Base-track reconstruction efficiency as a function of the base-track angle.

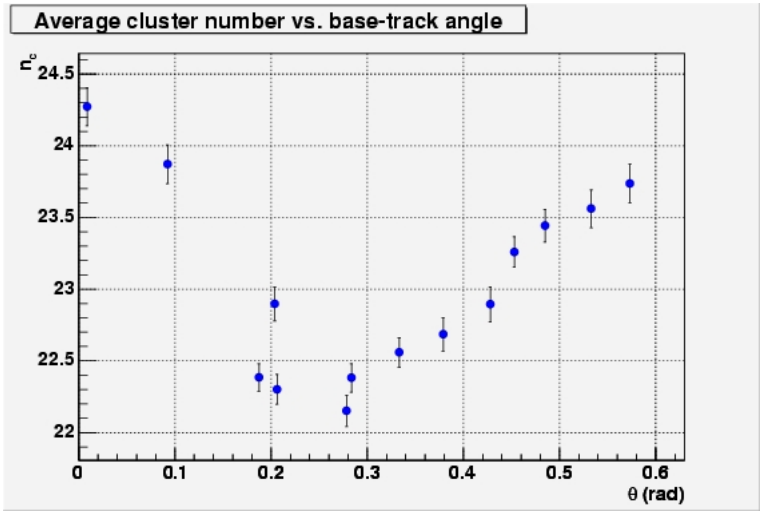

Figure 3.15: Average cluster number as a function of the base-track solid angle. The 250 mrad dip explains the lower base-track reconstruction efficiency in correspondence of the same angle. For details, refer to the text.

which brings to a background of $\sim$1.8 base-tracks/cm^2 within $|\theta| < 0.4$ rad. The new criterion implies a reduction less than 1% of the ε_{bt}, as shown in Fig. 3.17.

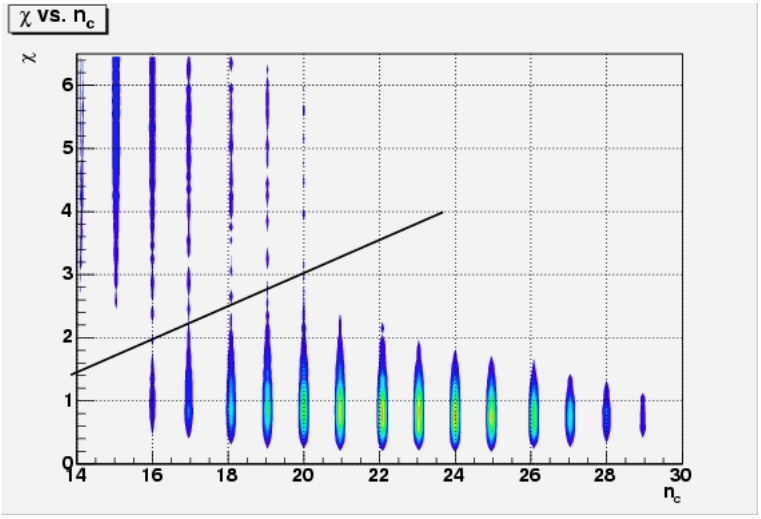

Figure 3.16: χ as a function of the average cluster number for signal base-tracks. The drawn line is the signal-background separator as defined in Eq. 3.5. The base-tracks above the line are assumed to be background tracks. The spot width is proportional to the entry number.

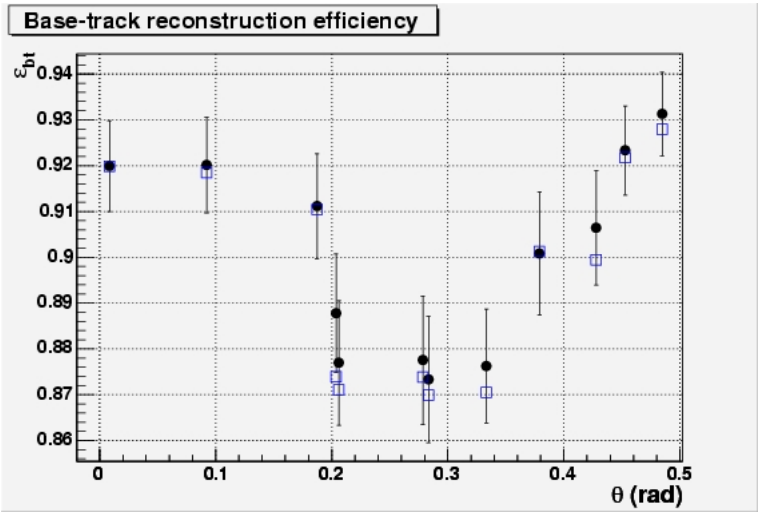

Figure 3.17: Base-track reconstruction efficiency (black circles) after the application of the combined cut in the (χ, n_c) plane. For comparison, also the efficiencies shown in Fig. 3.14 are given (open squares).

Chapter 4

Study of electromagnetic showers in ECC bricks

4.1 Purposes of this analysis

OPERA is an appearance experiment: the main aim is to search the τ's produced by the interactions of ν_μ of the CNGS beam oscillated in ν_τ. The expected number of tau interactions in five years of data taking in the OPERA detector is 180 at $\Delta m^2 = 2.5 \times 10^{-3}$ eV^2 and with CNGS beam upgrade ($\times$1.5). If one takes into account the detection efficiency equal to 9.1%, this number becomes $\sim$18. Hence, to claim the confirmation of $\nu_\mu \rightarrow \nu_\tau$ oscillations is necessary to keep the background at the lowest level possible.

The OPERA physics program about neutrino oscillations is complemented with the search for $\nu_\mu \rightarrow \nu_e$ looking for an excess of ν_eCC interactions.

It is important to have a good particle identification, but also to reduce as much as possible the mis-identification, *e.g.* a low energy pion can undergo a charge exchange process $\pi^- p \rightarrow \pi^0 n$ and produce an electromagnetic. shower. It is worth to note that the cross section of this process increases at low energy.

A good electron-pion separation is important both for the τ detection and the $\nu_\mu \rightarrow \nu_e$ oscillations study in all the following cases:

- to detect the electron in the $\tau \rightarrow e$ channel;
- to avoid the rejection of a ν_τ interaction if a hadron, attached to the primary vertex, is mis-identify as an electron (this inefficiency affects

all tau decay channels);

- to correctly identify a pion attached to the primary vertex that mimics a τ kink, if it undergoes a large scattering (this is a background for the electron channel both if it is a NC interaction or a CC interaction with the muon escaping unidentified);
- to detect the electron in the ν_eCC interactions.

Some Monte Carlo studies and preliminary experimental tests have been done in order to study the electron-pion separation.

In Ref. [1] the electron-pion separation was performed with an analysis based on multiple Coulomb scattering. However, the electron-enriched π^- beam did not provide a clean environment. In order to cross-check the procedure, the efficiency obtained with a Monte Carlo were used to compare the pion beam contamination with an independent test beam measurement performed with Cherenkov detectors.

In the OPERA proposal [44], a method to identify electrons based on a shower analysis is described. An electron is identified by counting the base-tracks related to the shower. The direction of the primary base-track, called "seed", defines the axis of a cone with an opening angle $\alpha = 50$ mrad. All the base-tracks inside the cone and with a relative angle with respect to the seed $\theta_{max} \leq 200$ mrad are considered as belonging to the e.m. shower generated by the seed itself.

Following this "crude" approach, in Ref. [64] a Neural Network algorithm for electron identification is implemented. However, at that time no real data were available, so no comparison with experimental data was performed.

At the DESY electron synchrotron, a new experimental test was performed exposing some OPERA bricks to a pure electron beam. In Bologna and in other laboratories of the Collaboration some bricks have be scanned. Unfortunately, the track density in these bricks is very far from the real OPERA situation and for a shower analysis as performed until now, since the number of tracks, not related to the electromagnetic shower, falling into the analysis region is too high. The primary electrons impinging on the exposed bricks have a density of $\sim$100 electrons/cm^2, comparable with the lateral spread of an electromagnetic shower. Hence adjacent electromagnetic showers overlap. Moreover, about one month elapsed from the brick exposure to the emulsion development, during which the emulsions integrated cosmic ray tracks.

Another limitation for a shower analysis is the number of emulsion sheets. The scanned bricks have 15 emulsion sheets, interleaved by the same number of lead plates. This length corresponds only to $\sim$3.3 X_0, so there is no shower containment at least for high energy electrons.

In this thesis we shall present a new algorithm to reconstruct e.m. showers and reduce the background tracks. For the electron/pion separation a new Neural Network is trained following the lines laid down in Ref. [64].

To complement this approach, a multiple Coulomb scattering analysis with a pure pion beam at the CERN PS-T7 was performed (refer to Ref. [2]).

4.2 Passage of particles and development of e.m. showers in the OPERA brick

Charged particles, like π's, K's or protons, having an energy lower than 100 GeV, lose energy in matter primarily by ionization and atomic excitation. Nuclear diffusion are, usually, negligible in the calculus of the energy loss. The mean rate of energy loss (or stopping power) is given by the Bethe-Bloch equation

$$-\frac{dE}{dx} = Kz^2\frac{Z}{A}\frac{1}{\beta^2}\left[\frac{1}{2}\ln\frac{2m_ec^2\beta^2\gamma^2T_{max}}{I^2} - \beta^2 - \frac{\delta}{2}\right] \tag{4.1}$$

where z is the charge of the incident particle, Z and A are respectively the atomic number and the atomic mass of the absorber, T_{max} is the maximum kinetic energy which can be imparted to a free electron in a single collision and I is the mean excitation energy measured in eV. With $K/A = 4\pi N_A r_e^2 m_e c^2$ measured in MeVg^{-1}cm^2 and A in gmol^{-1}, the units are MeVg^{-1}cm^2.

The average energy loss has a very characteristic dependence on the velocity of the incident particles, as it is shown for a muon in Fig. 4.1. The function is characterized by broad minimum whose position drops from $\beta\gamma = 3.5$ to 3.0 as Z goes from 7 to 100. In this energy region the incident particle are said "minimum ionizing particles", (*mips*) and, expressing the absorber thickness in unit of $x = \rho \times d$, where ρ is the density of the absorber (g/cm^3) and d is the thickness (cm), it can be found that for a mip the average energy loss is varying from a value of 2 MeV/g cm^{-2} for low-Z materials to 1.1 MeV/g cm^{-2} for high-Z materials, such as lead. Below the mip region energy loss increase, as $1/\beta^2$, above increases approximately logarithmically.

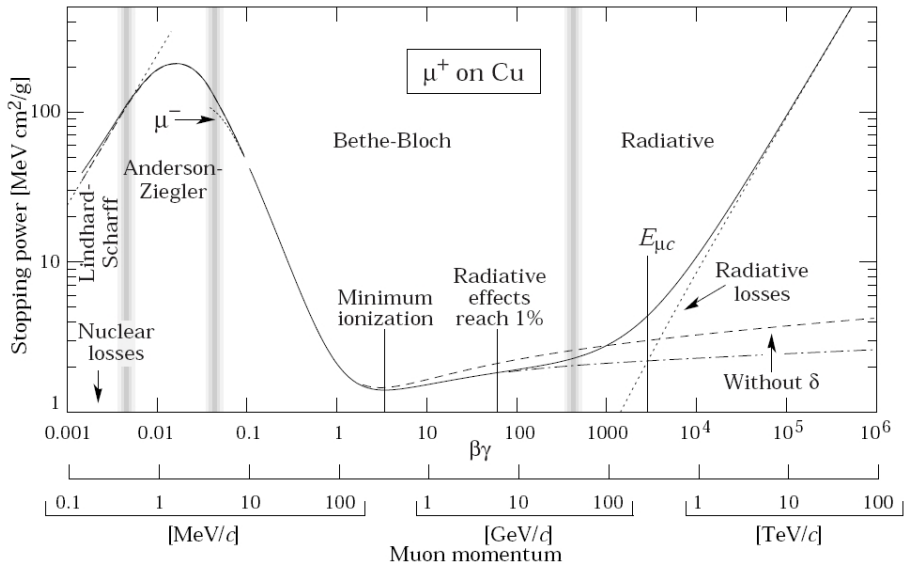

Figure 4.1: Stopping power ($= \langle -dE/dx \rangle$) for positive muons in copper as a function of $\beta\gamma = p/Mc$.

In the derivation of the Bethe-Bloch formula, it is assumed that the energy loss by the incident particle in a single interaction is negligible with respect to its total kinetic energy. This hypothesis is true only if the mass of the incident particle is much greater than the electron mass.

Since electrons and positrons do not verify this hypothesis, the formula that describes their energy loss is different[1].

As we shall see, in the energy range of our interest ($1 \div 10$ GeV) radioactive processes, which are responsible for the electron-positron shower development, dominate.

Multiple Coulomb scattering at small angles

A charged particle traversing a medium is deflected by many small-angle scatterings. Most of these deflections are due to Coulomb scattering from nuclei,

[1]For the electrons, moreover, it must be taken into account that the interaction with the atomic electrons are between identical particles, so the exclusion principle must be considered. The differences between electrons and positrons are appreciable only at low energy $\approx$ MeV, where Møller diffusion ($e^- e \to e^- e^-$), Bhabba diffusion ($e^+ e^- \to e^+ e^-$) and positron annihilation processes have to be taken into account.

and hence the effect is called multiple Coulomb scattering. For hadronic projectiles, the strong interactions also contribute to multiple scattering. The Coulomb scattering distribution is well described by the theory of Molière. It is roughly Gaussian for small deflection angles, but at larger angles, greater than a few θ_0 (defined below), it behaves like Rutherford scattering, having larger tails than does a Gaussian distribution.

If we define

$$\theta_0 = \theta_{plane}^{rms} = \frac{1}{\sqrt{2}}\theta_{space}^{rms}, \tag{4.2}$$

then it is sufficient for many applications to use a Gaussian approximation for the central 98% of the projected angular distribution, with a width given by

$$\theta_0 = \frac{13.6\ MeV}{\beta cp} z\sqrt{x/X_0}\left[1 + 0.038\ln(x/X_0)\right]. \tag{4.3}$$

The angular and position displacements as a function of the momentum of a particle transversing an emulsion sheet and a lead plate are show in Fig. 4.2. Since this formula is depending on the momentum of the traversing particle, it can be used for particle identification. The average energy of an electron after passing through a material of thickness z decreases exponentially as $E_e(z) = E_0 e^{-z/X_0}$, where E_0 is the incident electron energy, as explained in the following of this Paragraph. For a pion, instead, it is almost constant, $E_e(z) = E_0$. This difference can be used to distinguish electrons from pions by constructing two χ^2 corresponding to the two possible interpretations. Moreover, since E_0 is treated as a free parameter in the minimization of the χ^2, this method provides also a measure of the energy of the incident particle. For more details, refer to Ref. [1, 2].

Model of an electromagnetic shower

The simplified description of the development of e.m. showers was first developed by Heitel and Rossi [65]. There are two high-energy ($E > 100$ MeV) e.m. energy loss mechanisms through which the e.m. cascade is propagated. Electrons and positrons lose energy by *bremsstrahlung* radiation (Fig. 4.3), whereas photons degrade by *pair production* (Fig. 4.4).

The cross sections are quite energy-independent for $E \geq 10$ MeV, justifying the assumption of a constant cross section or constant mean free path

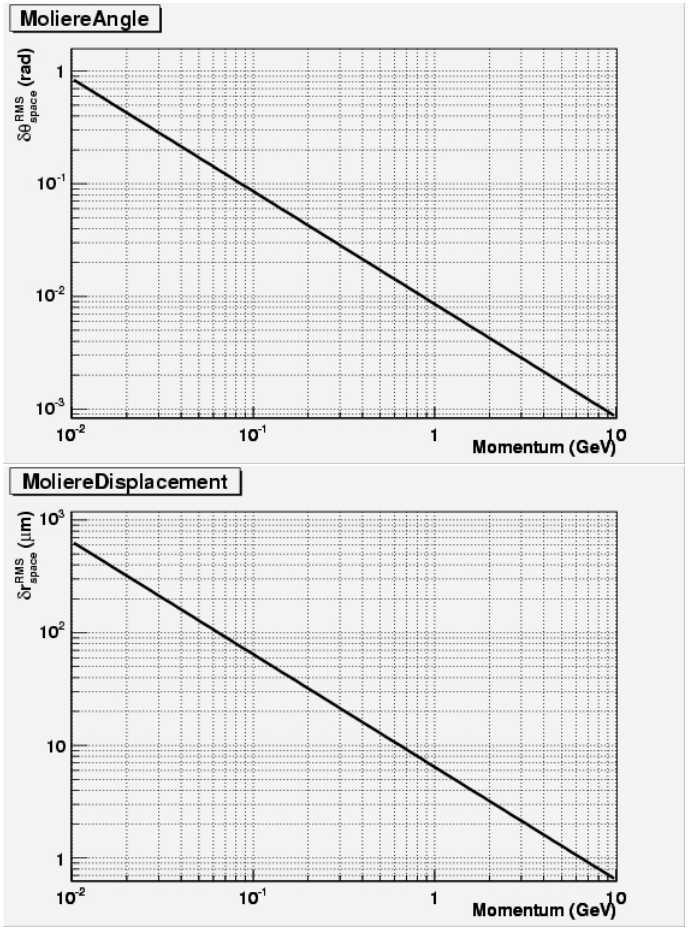

Figure 4.2: Molière angle and displacement as a function of the momentum of the transversing particle through an OPERA Emulsion Cloud Chamber.

between energy-degrading collisions. This picture leads to a two-dimensional cascade model, as sketched in Fig. 4.5.

The typical longitudinal dimension of an electromagnetic shower is determined by the mean free path between collisions, "radiation length", defined through the equation

$$\Delta E_{rad} = -E\frac{\Delta X}{X_0} \tag{4.4}$$

x_0 is the length over which the energy is degraded to $1/e$ of its initial

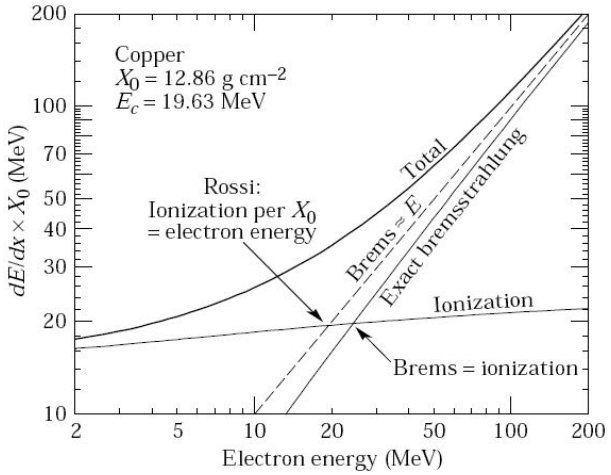

Figure 4.3: Energy loss mechanism for electrons and positrons in copper. Above the "critical energy" the main mechanism is the emission of bremsstrahlung radiation.

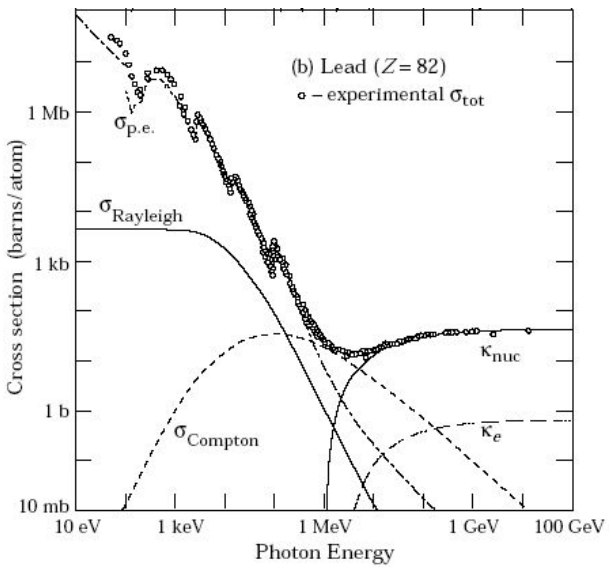

Figure 4.4: Cross section for the interactions of photons in lead. At high energies ($E_\gamma \geq 10$ MeV) the main contribution is pair production.

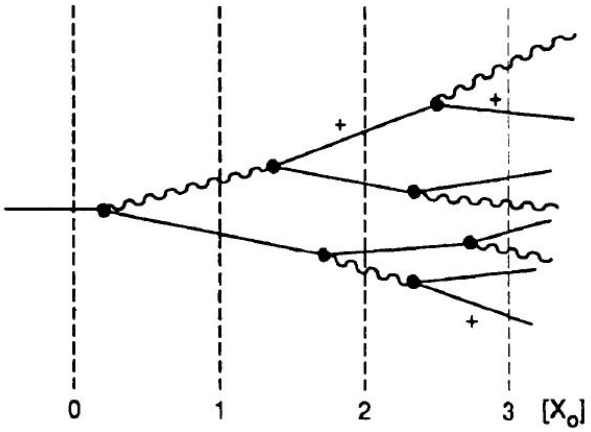

Figure 4.5: Two-dimensional cascade model of an e.m. shower. Two processes, bremsstrahlung and pair production are responsible for the energy degradation and the shower development.

value. This quantity can be estimated with the formula

$$X_0 = \frac{716.4 \text{ g} \cdot \text{cm}^{-2} A}{Z(Z+1)\ln 287/\sqrt{Z}}. \tag{4.5}$$

The cascade will continue until the energy of the components in the shower reaches a "critical energy" E_c, below which further multiplication stops, since the cross-sections for bremsstrahlung and pair production become smaller than for other energy loss processes, see Fig. 4.3 and 4.4). Numerically, the value for E_c is approximately

$$E_c = \frac{610 \text{ MeV}}{Z + 1.24}. \tag{4.6}$$

This simple model points to a remarkable feature of the e.m. shower. Given that the only dimensional scale of the problem is the radiation length X_0, it could be concluded that all e.m. showers should have the same longitudinal shape when the depth is expressed in units of X_0 for a given absorber material.

The transverse shower dimension in different materials scales fairly accurately with the Molière radius R_M, given by [66, 67]

$$R_M = X_0 \frac{21 \text{ MeV}}{E_c}, \tag{4.7}$$

expressed in unit of X_0 when E_c is in MeV. On average, only 10% of the energy lies outside the cylinder with radius R_M. In the case of OPERA, where the passive material is lead, $E_c \simeq 7.3$ MeV and the e.m. showers are well confined inside a radius of some millimeters.

4.3 Experimental test at DESY

An experimental test with a pure electron beam was performed at DESY to study the electron identification in a very clean environment.

In December 2003 the electron beam was studied [68]. The characterization was performed to achieve the best beam conditions for the exposure of ECC bricks, namely:

- the lowest number of electrons per unit of time;
- the lowest number of electrons per unit area;
- the lowest possible contamination due to interactions of electrons along the beam line.

The intensity can be reduced both by acting on the collimators or by reducing the primary beam intensity. The second method is preferable since it does not affect the beam profile. The density can be reduced by defocalizing the beam. However, this increase the the number of non controlled events. A compromise must be found.

The brick exposure was performed in July 2004.

The beam line

Three test-beam lines (T21, T22 and T24) providing electrons are available at the DESY electron synchrotron. A bremsstrahlung beam is generated by a carbon fiber put in the circulating beam of the electron/positron synchrotron DESY II. The photons are converted to electron/positron pairs with a metal plate. Then the beam is selected in sign and spread out into a horizontal fan with a dipole magnet. The final beam slice used is cut out of this fan with a collimator. A schematic layout of a test beam line at DESY is given in Fig. 4.6.

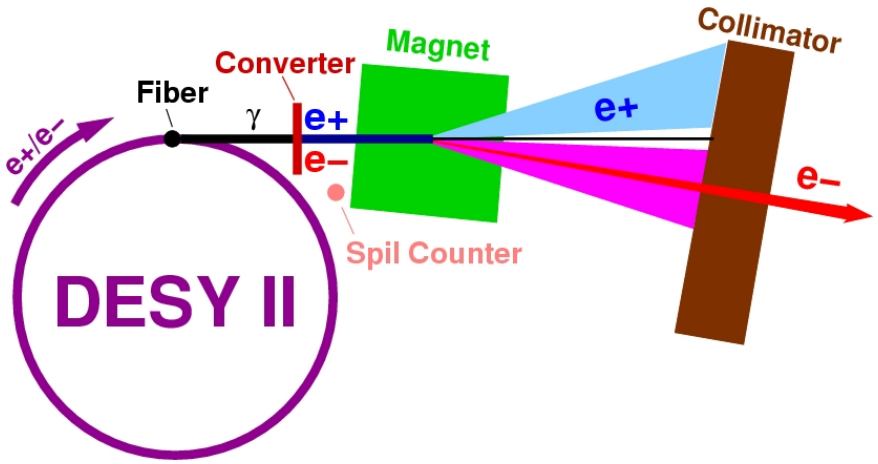

Figure 4.6: Schematic layout of a beam line at DESY.

The physics of the beam line is simple. The bremsstrahlung spectrum has a $1/E$ dependence. The energy distribution of the electron/positron pair conversion is nearly flat. The geometry is fixed by the beam pipe and the beam momentum can be set by changing the magnet current. The real situation is more complicate because the energy of the synchrotron varies with time: *i.e.* the bremsstrahlung edge of the photon spectrum changes in time with the cycles of the accelerator. The beam particles can reach the experimental area obviously only during the time E/c is above the chosen momentum. The momentum of the electrons reaching the experimental area can typically range from 1 to 6 GeV/c with an energy spread of $\sim$5%.

The electron rates are influenced by many parameters: the current in the machine, the operation mode of the machine (if DESY II is injecting particles to DORIS and/or PETRA or not), the position of the carbon fiber in the beam, the converter target, the current in the magnets of the beam line, *i.e.* the selected momentum, the opening of the collimators.

The accelerator control room handles the fiber target and the beam intensity in DESY II. The currents in the magnets, the choice of the target and the positions of the 4 jaws defining the collimator opening are under control of the user from the counting room.

In order to get the lowest possible particle rate, the beam can be run in a dedicated mode by reducing the current intensity circulating inside the synchrotron from the normal 2 mA to a minimum of 0.04 mA.

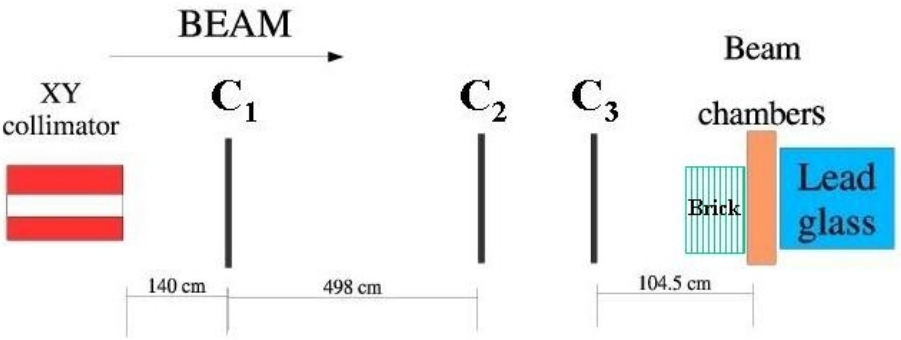

Figure 4.7: Schematic layout of the experimental set-up at DESY. It is shown the location of the brick during the exposure in July 2004.

Moreover, the beam line can run without converter target and with a 0.5 mm thick aluminum window at the end of the vacuum chamber just to have the photons converting into e^+e^- pairs.

We tried to use the shortest exposure time of a brick on the beam line. This is determined by the time needed to move the beam shutter in the secondary line. Once the beam is on, to turn it off the minimum time is about 3 s. This is an important number to be taken into account in order to evaluate the lowest achievable track density for a given brick position.

The experimental set up

Following the beam line the most upstream part of the set-up is the trigger system: it is made out of three scintillation counters centered with respect to the beam line by means of motorized supports remotely controlled from the counting room. They are mounted perpendicularly to the beam line. Two of them, C_1 and C_2, are normally used in coincidence to provide the trigger signal, the third one (C_3) was used to evaluate the trigger efficiency. Due to their superposition, C_1 and C_2 have a transverse sensitive area of about 10×12 cm^2. The distance between these 2 scintillation counters is 498 cm. In this configuration the trigger system selects the particles crossing an area of about 10×10 cm^2 centered around the beam axis. The experimental set-up is shown in Fig. 4.7.

Behind the trigger system, 104.5 cm far from C_3, there is a Multiwire

Proportional Chamber operating with a gas mixture of 50% Ar and 50% CO_2 and allowing to measure two perpendicular coordinates with a resolution of 200 microns. The chamber has an active area of 11×11 cm^2. A few centimeters downstream of the chamber there is a lead glass that provides an energy measurement of the electrons. The lead glass block has a square section of 15×15 cm^2 and a length corresponding to about 20 radiation lengths.

The trigger efficiency (ε_{trig}) was measured by the counter C_3. Each counter efficiency is estimated by the ratio of the number of triple coincidences to the number of double coincidences between the other two counters. The measurements were repeated at various energies, since there were changes in the beam profile due to the multiple Coulomb scattering (thus implying different effective areas of the counters). These values have to be considered as lower limits on the real efficiencies. The results are given in Tab. 4.1.

E (GeV)	ε_{C_1}	ε_{C_2}	ε_{trig}
1	92.2 ± 0.3	96.3 ± 0.2	88.8 ± 0.4
3	96.6 ± 0.1	98.44 ± 0.07	95.1 ± 0.2
6	94.14 ± 0.10	98.93 ± 0.04	93.14 ± 0.13

Table 4.1: Efficiency of the counters C_1 and C_2 as measured by the coincidence with C_3 and the trigger efficiency.

Beam characterization

Our aim was to get the cleanest, widest and as much as possible uniform beam.

The lead glass is used to measure the energy resolution. Fig. 4.8 shows the energy resolution calculated as the percentage ratio of the sigma of the Gaussian that fits the lead glass response to its mean for different nominal energies and the lead glass response as a function of the nominal energy, fitted by a linear function.

The beam width is defined as two times the RMS of the projected distribution of the impact points measured by the beam chambers.

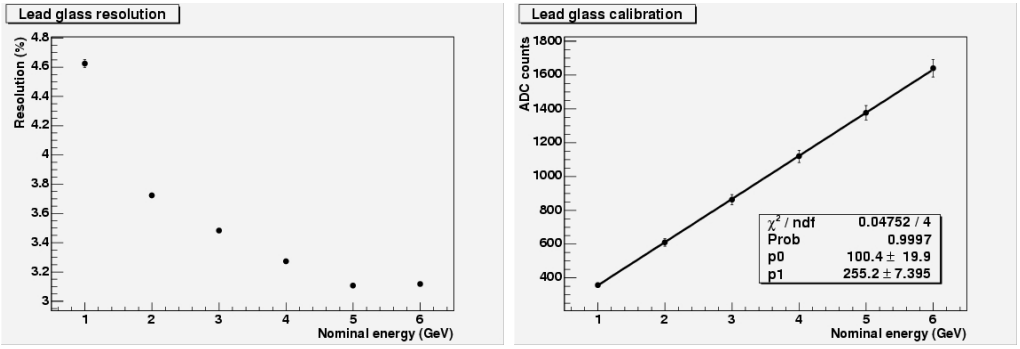

Figure 4.8: Right: beam energy resolution measured with the lead glass as a function of the nominal energy. Left: calibration of the lead glass.

The contamination of the beam, ε_{cont}, is defined as the fraction of events that were more than 3σ far from the mean value of the energy spectrum measured with the lead glass. Both the sigma and the mean value were obtained with a Gaussian fit. The beam contamination for different values of the beam nominal energy given in Tab. 4.2. ε_{cont} increases at low energy because the beam is wider.

E (GeV)	ε_{cont}
1	5.7 ± 0.2
2	3.4 ± 0.1
3	3.0 ± 0.1
4	3.1 ± 0.1
5	2.8 ± 0.1
6	2.4 ± 0.1

Table 4.2: Beam contamination for different values of the beam nominal energy.

Moreover, the beam contamination varies with the opening of the collimators. The opening of the collimator is referred to the center of the beam line and could be varied independently for the top and bottom edge slides or the right and left ones. ε_{cont} increases with a large opening because of interactions along the beam pine. Moreover, ε_{cont} increases when the col-

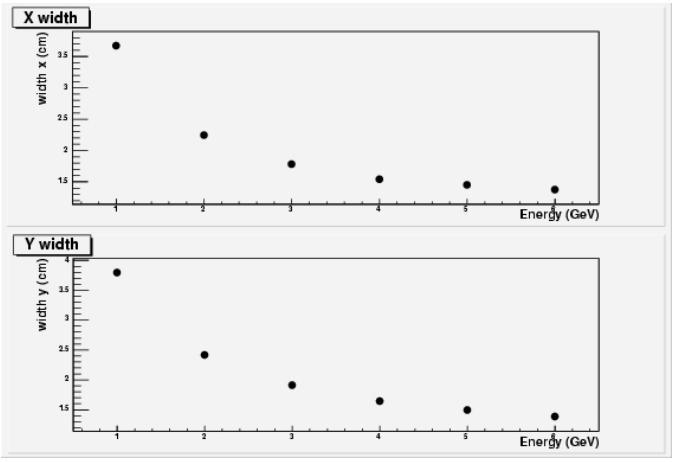

Figure 4.9: Beam width as a function of the beam energy.

limators are almost closed because of the interactions with the collimators themselves. The results for a 6 GeV beam are summarized in Tab. 4.3. Due to the minimum beam contamination, the configuration 2 was used.

The beam width as a function of the energy is shown in Fig. 4.9. The beam profile and its projections obtained with the final collimator configuration for 1 and 6 GeV are shown in Fig. 4.10.

The measured energy distributions with the lead glass for nominal energies between 1 and 6 GeV are shown in Fig. 4.11.

To have reasonable statistics all the studies of the beam contamination and beam profile were performed at standard beam intensity (2 mA). The reduction of the synchrotron current reflects in the counting rates without

	current (mA)	left/right (mm)	top/bottom (mm)	rate (Hz)	h. width (mm)	v. width (mm)	ε_{cont} (%)
1	2	10.0	5.0	154	18.1	13.8	3.4
2	2	5.0	5.0	75	13.9	13.7	2.4
3	2	2.5	2.5	17	12.5	11.9	3.2

Table 4.3: Beam width as a function of the collimator aperture with respect to the center of the beam line. The beam energy was 6 GeV.

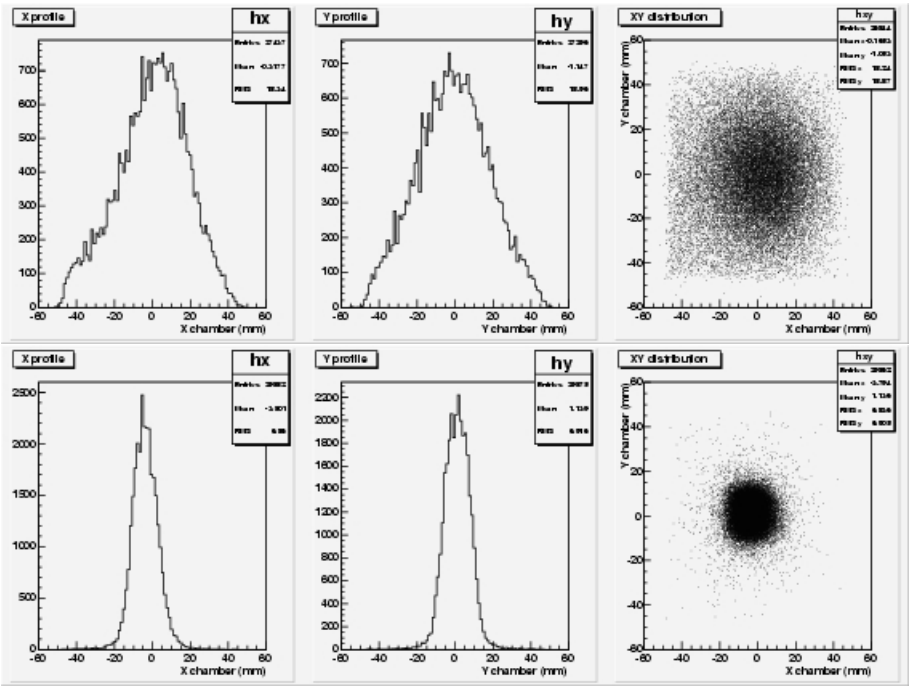

Figure 4.10: Beam profile for 1 GeV (top) and 6 GeV (bottom) in the configuration 2 of Tab. 4.3.

any effect on the beam contamination and beam profile. We studied the rates as a function of the energy for two different reduced beam currents. At the current of 0.2 mA we took measurements at all energies, while at the lower 0.04 mA current we took just two energies to check that the rates were scaling accordingly; the same scaling factor can be easily applied for all the remaining energies. The results, corrected for the efficiencies, are given in Tab. 4.4. In the last column a rough estimate of the flux is reported. We considered the number of events per time unit within an ellipse with semi-axises equal to the RMS's of the X and Y beam distributions centered along the beam line.

In order to have a more precise flux estimate, we divided a brick in cells of 1×1 cm^2/s and calculated the flux for each cell. Using the rates given in Tab. 4.4 and the measured beam profile, we simulated the exposure of a brick to an electron beam of a given energy to several spots in different

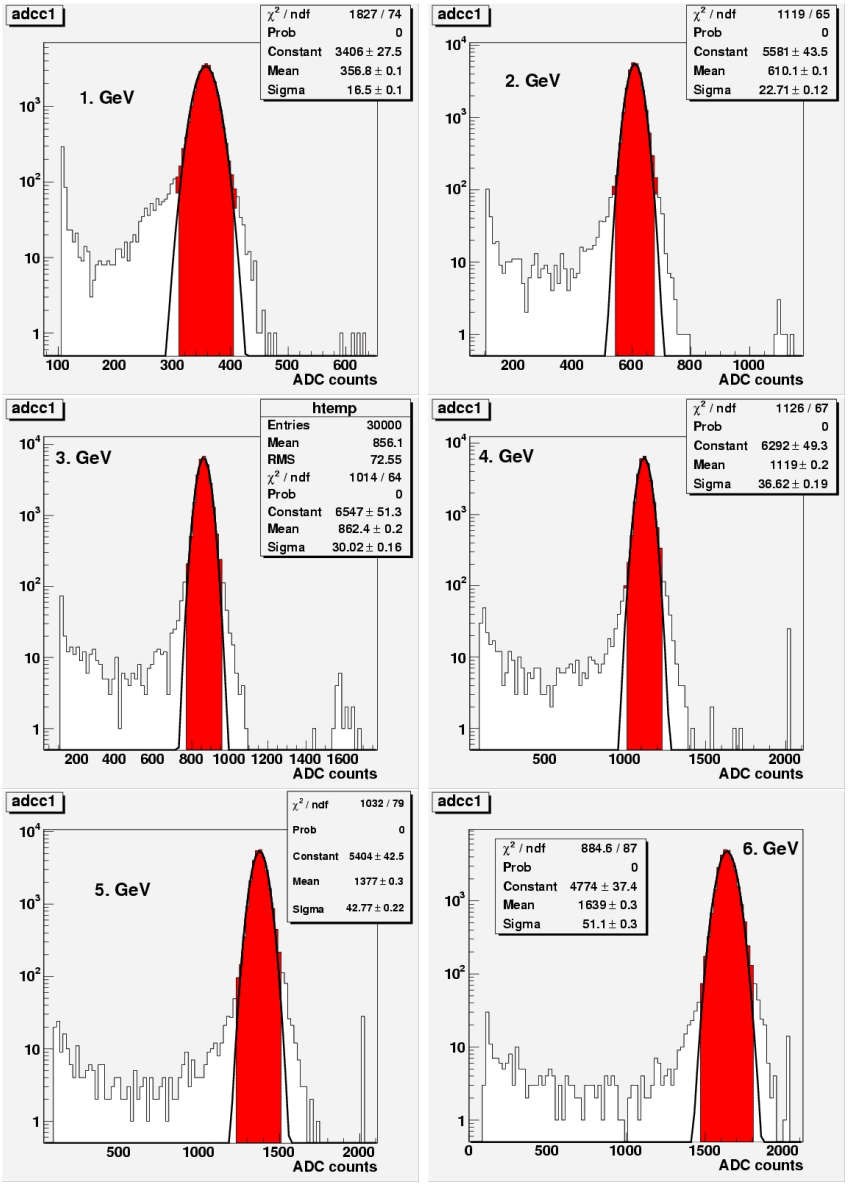

Figure 4.11: Lead glass output for electron exposure at the different energies. The electron signal (dark area) is fitted with a Gaussian. The fit result is plotted with the black continuous line. The white area of the distributions are the background events (more than 3σ from the mean of the Gaussian).

points. This simulation was used to optimize the number of spots for the low density exposures (1 particle/cm^2). The results for 1 and 6 GeV are shown in Fig. 4.12. Similar plots have been obtained at the other energies.

Bricks exposure

The second experimental test was performed in July, 2004 with the same electronic experimental set-up as in December 2003. The bricks were placed upstream of the beam chamber (see Fig. 4.7) on a translation stage remotely controlled from the counting room, in both the directions perpendicular to the beam line. This allows to "hit" the bricks with several beam spots in different positions.

It was chosen to expose six OPERA bricks to different energies: 4 at high density (50÷100 particle/cm^2) at the energies of 1, 3 and 6 GeV (two time) and 2 at low density ($\sim$1 particles/cm^2) at the energies of 3 and 6 GeV. Each brick was exposed several times to the electron beam by changing each time the impact zone (spot) according to the study performed after the first test beam experiment (see Fig. 4.12). In Tab. 4.5 the exposed bricks are summarized. One brick was not exposed for background estimation, this brick was in the controlled area zone (but not on the beam line) during the exposure of the brick 7.

current (mA)	E (GeV)	rate (Hz)	flux (Hz $\times$ cm^{-2})
0.2	1	4.3 ± 0.2	0.39 ± 0.02
0.2	2	18.7 ± 0.5	4.4 ± 0.1
0.2	3	33.1 ± 0.7	12.4 ± 0.3
0.2	4	28.5 ± 0.6	14.4 ± 0.3
0.2	5	17.3 ± 0.5	10.2 ± 0.3
0.2	6	7.4 ± 0.3	5.0 ± 0.2
0.04	3	3.7 ± 0.7	1.4 ± 0.3
0.04	6	0.9 ± 0.3	0.6 ± 0.2

Table 4.4: Electron rates recorded by the scintillation counter trigger and electron fluxes measured with the wire chambers as varying with the synchrotron current and the nominal beam energy.

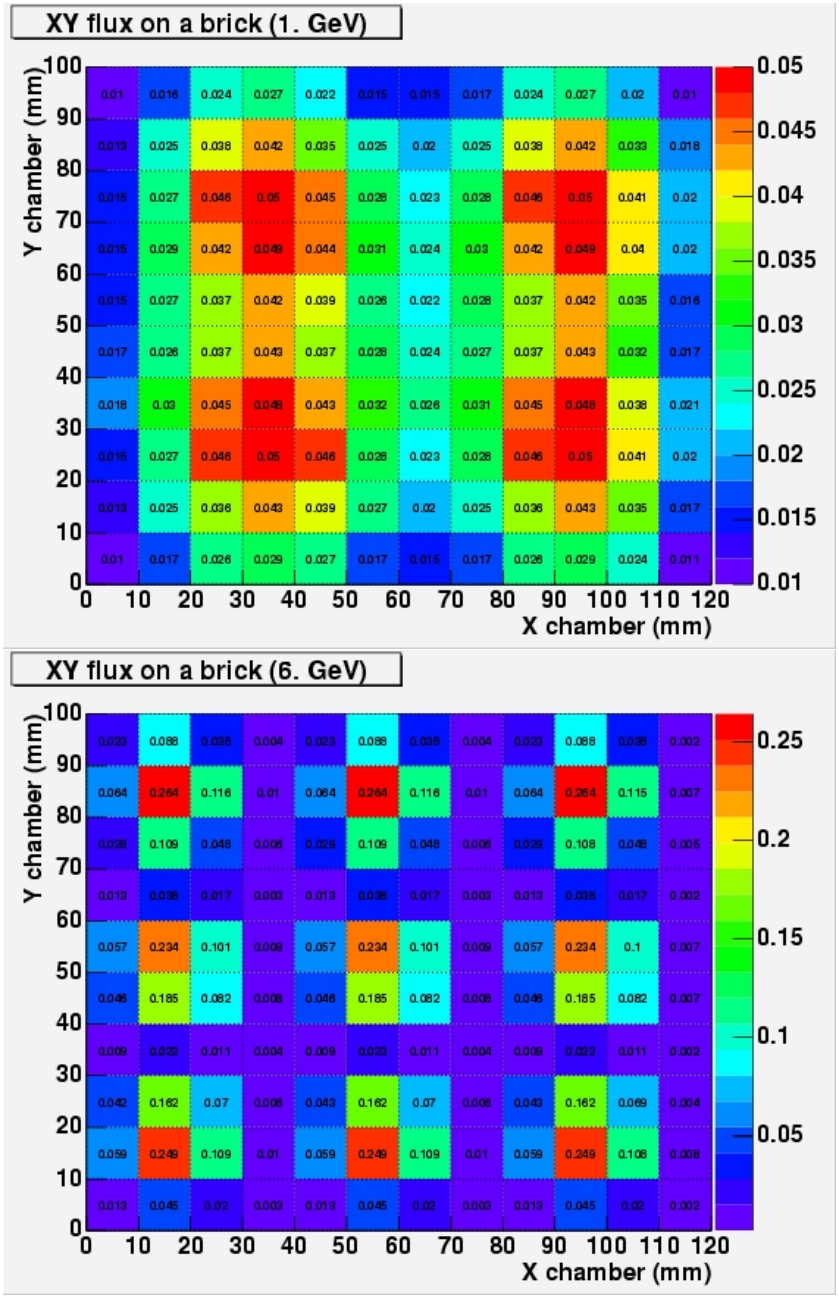

Figure 4.12: Simulation of the flux on a brick exposed to electron beams with energies of 1 GeV (top) and 6 GeV (bottom). In each square, with an area of 1 cm^2, the number of electron per time unit is given.

Brick	E (GeV)	Emulsion sheets per brick	Density (electrons/mm^2)
1	1	15	0.5
2	3	15	1
3	6	15	1
4	6	20	1
5	not exposed	20	
6	3	40	0.01
7	6	50	0.01

Table 4.5: Summary of the bricks exposed at DESY. The tables gives the electron beam energy, the electron density and the number of emulsion sheets for each brick.

4.4 Scanning of the exposed bricks

In this section a first analysis of the measured data is presented and a rough estimation of the background at the base-track level is given.

In Bologna laboratory the high density brick at 1 and 3 GeV (1 and 2 in Tab. 4.5) were scanned but we also profit of the scanning of the bricks 3 and 4 done in other laboratories, Bari and Neuchàtel.

Fig. 4.13 shows the electron peak signals as seen in the most upstream sheet. The distribution of the x angular projection is given by selecting the base-tracks that are within 4σ from the mean of distribution of the y angular projection fitted with a Gaussian. The same is for the y projection.

As anticipated in Par. 4.1, the shower analysis with the analyzed bricks is very "critical" since it suffers from two different sources of background:

1. background of tracks not related to the beam;

2. showers overlapping.

An estimate of the track density in the scanned emulsion sheets is made by counting all base-tracks within 400 mrad in both the angular projection and with the cut of Eq. 3.5. The measured value is $\sim$35 base-tracks/mm^2, two order of magnitude larger than what we can tolerate to perform a shower analysis as accordingly to the OPERA proposal [44]. It is not reasonable to

count all base-tracks inside a cone but a proper propagation of the showers inside the bricks has to be done preliminary in order to reduce the background.

The overlapping of adjacent showers is due to their lateral spread, that is of the order of 1 mm in lead. This value is almost coincident with the average distance of two primary electron impinging on the analyzed bricks.

Angle and position tolerances must be optimized in order to collect as much base-track related to shower as possible while rejecting background tracks. To be efficient in the shower reconstruction, the angular and position tolerances must be increased with respect to a standard propagation of a mip. From Fig. 4.2 it can be seen that the Molière angle and displacement for 100 MeV particles are of the order of 100 mrad and 100 μm, respectively. We expect that, with this "large" spatial tolerances, background contamination will be reduced at the level of $\sim$0.2/base-tracks/cm^2 by simple computation based on phase space reduction.

In the next Chapter we shall discuss the optimization of the algorithm for shower reconstruction. It is worth to note that background sources, that we had to face in this analysis work, are very far from the real OPERA case. Therefore, the obtained results can be considered as conservative and only lower limits to what can be obtained in the real OPERA exposure.

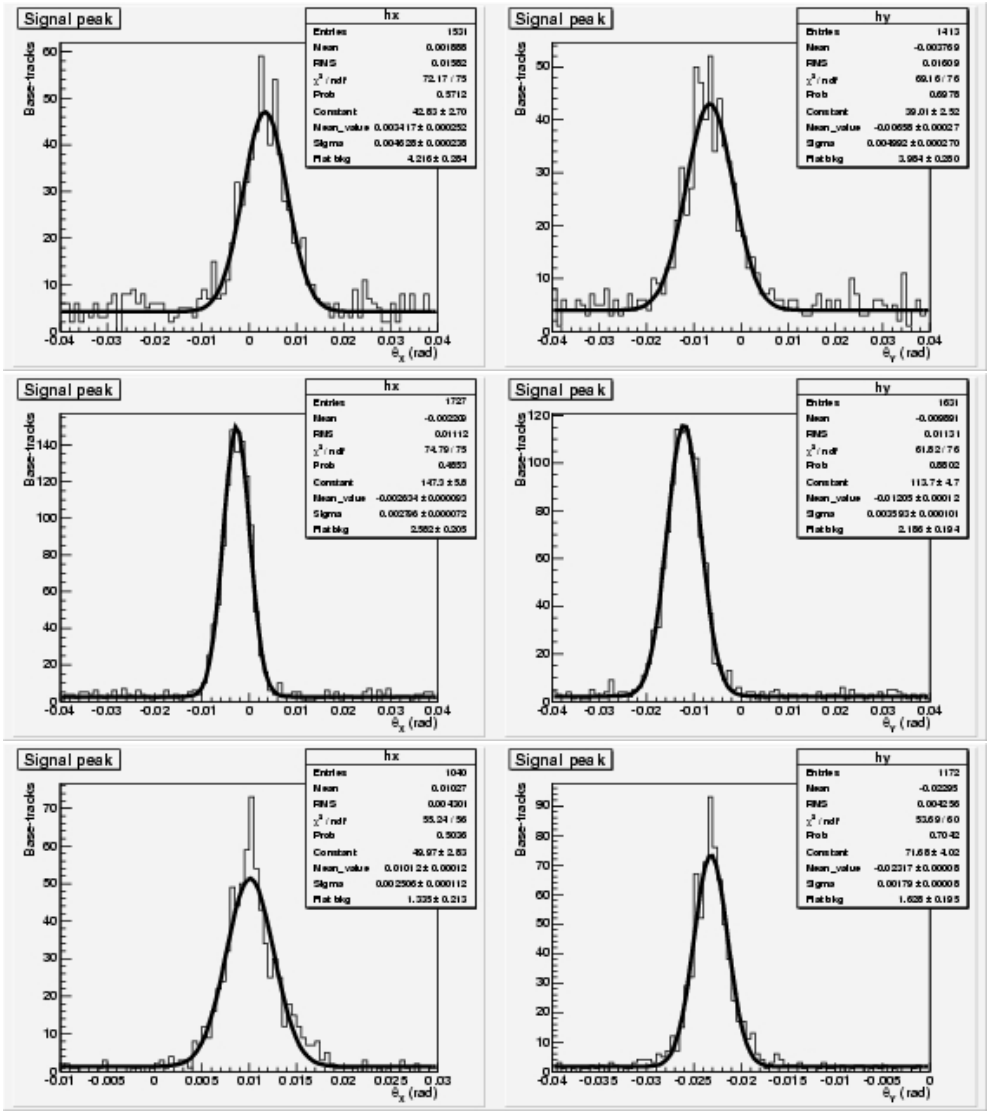

Figure 4.13: Base-tracks signals in the first emulsion sheet of the bricks exposed to electrons at DESY. Angular distributions for the x projection is on the left column, y projection on the right. Top figures are for 1 GeV, central figures for 3 GeV, bottom figures for 6 GeV.

Chapter 5

Analysis and results

In this Chapter we discuss the shower reconstruction algorithm and the electron-pion separation analysis using a Neural Network. The implementation of the algorithm for shower reconstruction has been discussed in Par. 5.2. Since its formulation is strongly based on data-Monte Carlo comparisons, a preliminary discussion on the Monte Carlo's used in this thesis is given in Par. 5.1. A short overview about the use of a Neural Network as a classification tool is given in Par. 5.3, while the NN input variables used to describe the longitudinal development of electromagnetic showers are defined in Par. 5.4. Finally, the study of electron and pion identification efficiencies is reported in Par. 5.5, together with the results obtained with real data. Besides the electron data of the DESY exposure, described in Par. 4.3, also pion data have been analyzed. These exposures were performed at the CERN PS in June 2003 [2] and August 2004.

5.1 Monte Carlo simulations

The official simulation package of the OPERA experiment, *OpROOT*, is based on GEANT3 [69]. In the near future, the use of GEANT4 and FLUKA packages are foreseen.

In this work we have used a simplified version of OpROOT which deals with stand-alone bricks, taking into account the brick geometry and materials. All the generated primary and secondaries tracks are traced through a brick taking into account all the relevant physical processes. Secondaries are propagated down to 1 MeV kinetic energy.

To correctly simulate the multiple Coulomb scattering, we forced steps of 10 μm inside the materials, since GEANT3 does not take into account the lateral displacement of the scattered particles.

In order to cross-check the GEANT3 simulation results, we also used FLUKA [70] to simulate the propagation of electrons and pions in a OPERA brick. All the physical cuts were fixed to the ones used in GEANT3.

For each emulsion layer, Monte Carlo provides a pair of *hits*, one at the entrance of the emulsion, the other at the exit. These pair of hits are then connected to form a "micro-track". Micro-tracks are then properly treated by a dedicated software [71].

A Gaussian smearing has bean applied both to the micro-track angle and base intercepts. We observe that base-track angular resolutions are affected only by the intercept smearings, since they are built connecting the two intercepts across the base. The intercept smearings, $\sigma_{X,Y}$, have been chosen in order to reproduce the experimental base-track resolution, $\sigma_{\theta_{X,Y}}$, according to the relation

$$\sigma_{\theta_{X,Y}} = \sqrt{2}\frac{\sigma_{X,Y}}{d} \tag{5.1}$$

where d is the thickness of the base (210 μm) and the $\sqrt{2}$ factor takes into accounts the two micro-tracks used to construct a base-track. The degradation of the resolution as a function of the angle (see Eq. 3.4) has been taken into account.

Micro-track reconstruction efficiency has been simulated using a constant value for all angles: it is the square root of the mean value of the base-track efficiency as measured with the microscope (see Fig. 3.17).

Finally the number of clusters for each micro-track has been sampled from a Gaussian distribution, whose parameters were obtained from experimental data[1].

No local effects (*e.g.* distortions) have been simulated. They are strongly dependent on the emulsion development phase and its simulation is a very hard task. Given the small emulsion thickness, distortions should play a minor role. No smearing of the micro-track z position has been applied. The emulsion-base surface, as measured by the automatic system, changes within

[1]In the real data the distribution of the number of clusters of micro-tracks follows a poissonian distribution: however, a poissonian distribution with a mean value $\sim 12 \div 13$ is well approximated by a gaussian distribution.

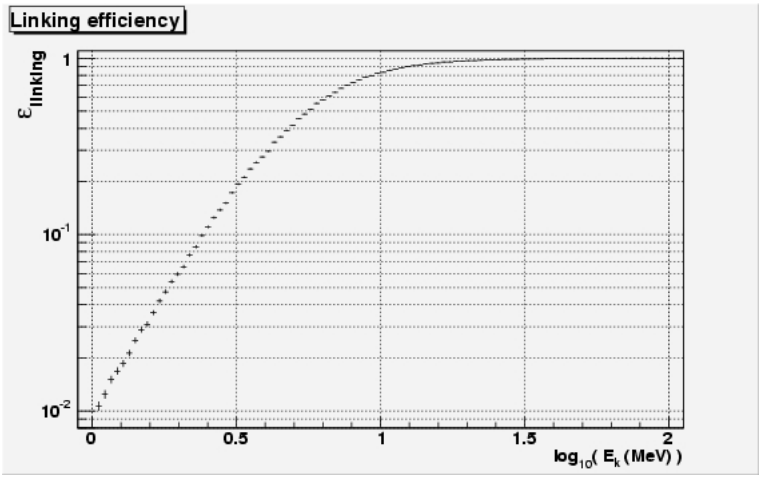

Figure 5.1: Top-bottom linking efficiency as a function of the kinetic energy of the incoming particles (electrons in this case).

few microns inside the scanned area. For the simulated data, we considered an "ideal" planar surface.

Once smearing and efficiency corrections are applied to the micro-tracks, base-tracks are formed by means of FEDRA libraries. Each top micro-track is linked with the corresponding bottom one using the tolerances estimated from real data. The linking efficiency as a function of the kinetic energy is given in Fig. 5.1.

From now on, both experimental and simulated data follow the same analysis flow, with the exception of the alignment procedure performed only for real data using FEDRA libraries.

Another difference between real data and Monte Carlo simulation is the signal selection. In the real data, a base-track is propagated if it is within 4σ from the average of the angular projection distributions (Fig. 4.13). For Monte Carlo data, all the primary electron base-tracks in the first sheet are propagated.

The following data have been simulated in a brick made of 15 emulsion sheets interleaved with 15 lead plates:

1. 12000 electrons and pions with energy in range $0.5 \div 10$ GeV with GEANT3;

2. 1000 electrons per each of the following energies: 1, 2, 3, 4, 5, 6, 7, 8,

9 GeV with both GEANT3 and FLUKA;

3. 1000 pions per each of the following energies: 1, 2, 3, 4, 5, 6, 7, 8, 9 GeV with both GEANT3 and FLUKA;

4. a simulation with GEANT3 of the brick exposed at DESY to 1, 3, 6 GeV electrons according to the electron number collected during the exposure and with the same density.

The first sample is used to train the Neural Network. The second and the third samples are used to cross-check the two Monte Carlo's, to tune the propagation algorithm and to test the Neural Network performances with events not used during the training. The last samples have been used to study the shower overlapping in the exposed bricks.

The same area was measured in all the sheets of a brick. This defines the *scanned volume*. To simulate the scanned volume in the Monte Carlo data, we defined the region that includes all the primary electrons in the first sheet of the simulated brick. All base-tracks that intercept the downstream sheets outside this region have been discarded.

5.2 Algorithm for shower reconstruction

To reconstruct a shower, it is necessary to develop a dedicated algorithm that starts the propagation from the "seed", the base-track in the most upstream emulsion sheet. This procedure has to mimic the real OPERA case, where all tracks emerging from a neutrino interaction vertex are followed. Moreover, there are some requirements to be satisfied: a good efficiency in collecting the base-tracks belonging to the shower and avoid casual matches with background base-tracks as discussed in Par. 4.1 and 4.4.

In the following, all base-tracks that satisfy the following criteria are kept:

- $n_{\text{cluster}} \geq 7$ for each micro-track,
- $\chi < 0.25 \cdot n_{\text{cluster}} - 3$,
- $|\tan\theta_X| \leq 0.400$,
- $|\tan\theta_Y| \leq 0.400$.

Once the base-track have been linked and the emulsion sheets aligned, tracking inside the scanned volume is performed inside the FEDRA framework. In this phase, the tolerances take into account both the resolution of the microscope (see Par. 3.5) and the multiple Coulomb scattering. So, the reconstruction volume is filled up with base-tracks in the aligned reference frame. Part of these base-tracks have been linked together to form volume-tracks.

The strategy followed has been to open a cone with the axis coincident with the direction of the seed. In this "critical" experimental situation, the cone is used as a fiducial volume: all the base-tracks that are outside the cone are not considered during the propagation. Moreover, also base-tracks inside the cone are eliminated if they belong to a volume-track that starts outside the cone itself, *i.e.* they are considered as "passing-through" for the actual seed and interpreted as cosmic rays.

The propagation algorithm follows an iterative procedure. Starting from the most upstream sheet, each base-track is considered as "selector" for the base-track "candidates" in the downstream sheets. A selector can be compatible with one or more candidates in a sheet. In order to reconstruct a shower, all compatible base-tracks are considered to belong to the shower. The selector and a candidate are compatible if their angle and position displacements satisfy some predetermined tolerances. The angle displacement $\delta\theta$ is defined as the solid angle difference between the selector and the candidate, while the position displacement δr is the distances of the intercepts of the selector and the candidate tracks with the plane defined by $z = z_0$, where z_0 is the middle point between the z coordinates of the selector and the candidate. Any compatible candidate then becomes the starting point for another propagation step, and so on. In order to take into account the base-track reconstruction efficiency, $\varepsilon_{bt} \simeq 90\%$ (see Par. 3.5.1), a selector is allowed to been propagated for at maximum 3 sheet, otherwise is discarded. However, when a selector is found to be compatible with a candidate, it is not more propagated in the next downstream sheets.

The angle and position tolerances, $\delta\theta_{max}$ and δr_{max} have been studied and optimized using Monte Carlo. Fig. 5.2 and 5.3 show the distributions of position and angle displacements of base-tracks propagate in a shower with $\delta r_{max} = 200$ μm and $\delta\theta_{max} = 100$ mrad. The distributions on the left include all the base-tracks, while the ones on the right include only the base-tracks that have been previously linked in a volume-track by means of FEDRA

libraries. These distributions have been normalized using as a scaling factor the ratio between data and Monte Carlo on the left distributions. As expected, the number of background tracks increases with the tolerance values. Moreover, for small position tolerances the agreement between data and Monte Carlo is poor: this is due to the fact that neither sheet dis-alignment nor local distortions have been simulated. Fig. 5.4 shows the distributions of the differences of track positions in adjacent emulsion sheets for data and Monte Carlo. The difference between the sigmas of the distributions explains the disagreement between data and Monte Carlo for what concerns the small displacements in the distributions of Fig. 5.2. This limitation of the emulsions simulation must be taken into account. So, although one normally expects that data-Monte Carlo agreement is better for small tolerances, our situation is far from the "ideal" one.

To choose the best parameters for the propagation, $\delta\theta_{max}$ and δr_{max}, we varied δr_{max} from 50 μm to 150 μm and $\delta\theta_{max}$ from 50 mrad to 150 mrad. The results are given in Fig. 5.5 and 5.6. The combined studies of these plots suggest the choice $\delta\theta_{max} = 90$ mrad and $\delta r_{max}100$ μm. As explained before, in limit of small tolerances, the data-Monte Carlo ratio is different for 1 because our Monte Carlo simulation does not take into account some peculiarities of the real data.

The second step concern the optimization of the cone aperture α. We varied α in the range from 10 mrad to 50 mrad and then we applied the propagation algorithm. The results are show on the left of Fig. 5.7. After the propagation, backgrounds tracks coming from other events is less 5% even for 6 GeV electrons. We also checked the efficiency of collecting tracks that belong to the shower. The results are given on the right of Fig. 5.7.

Since the shower reconstruction algorithm keeps the contamination due to the shower overlapping at the level of few percent, we chose a cone aperture of 50 mrad. Fixing the propagation tolerances to previously described values, we show the obtained agreement between data and Monte Carlo: in Fig. 5.8 we show the distribution of the number of base-tracks integrated in the cone volume after shower propagation for 3 GeV electrons; in Fig. 5.9 we show the longitudinal profiles of the number of base-tracks as function of the sheet number for 3 GeV electrons. Finally, the reconstructed shower of a 6 GeV electron is shown in Fig. 5.10.

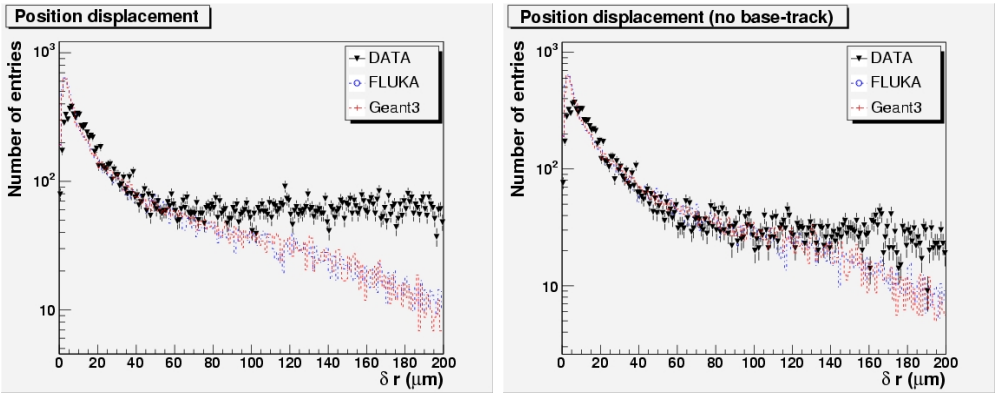

Figure 5.2: Distributions of the position displacement of the base-tracks propagated in a shower for 1 GeV electrons. The angle and position tolerances used are 100 mrad and 200 μm, respectively. The left figure includes all the propagated base-tracks, the right figure only the base-tracks that have been previously linked in a volume-track by means of FEDRA libraries. Comparisons with the Monte Carlo are shown.

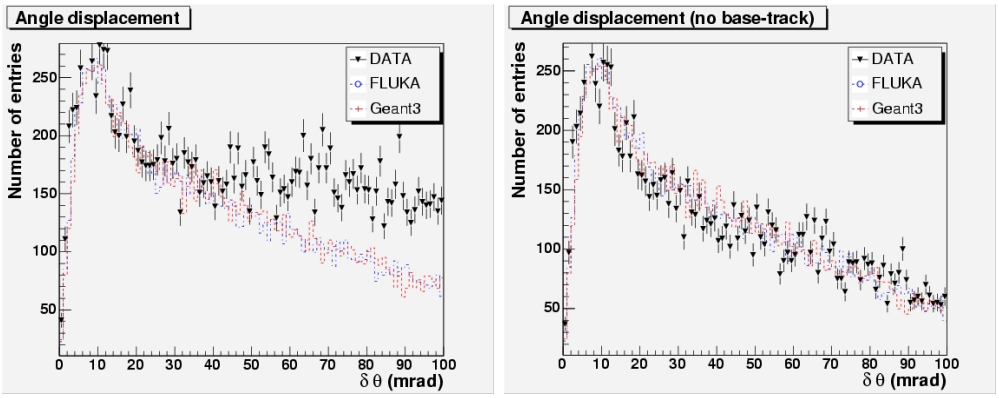

Figure 5.3: Distributions of the angle displacement of the base-tracks propagated in a shower for 1 GeV electrons. The angle and position tolerances used are 100 mrad and 200 μm, respectively. The left figure includes all the propagated base-tracks, the right figure only the base-tracks that have been previously linked in a volume-track by means of FEDRA libraries. Comparisons with the Monte Carlo are shown.

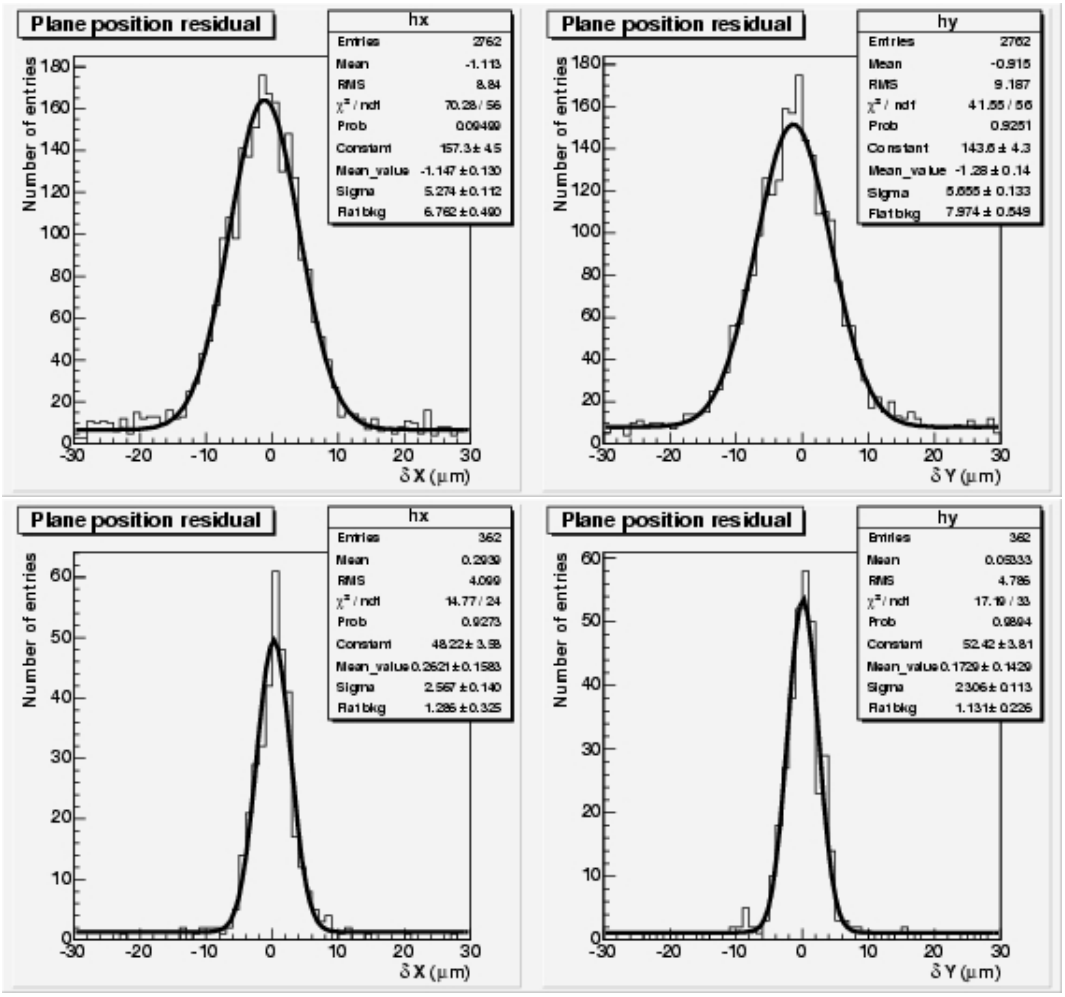

Figure 5.4: Sheet-to-sheet position residuals for the X projection (left) and Y projection (right). Top figures are for 1 GeV real data electrons, bottom figures for 1 GeV Monte Carlo electrons.

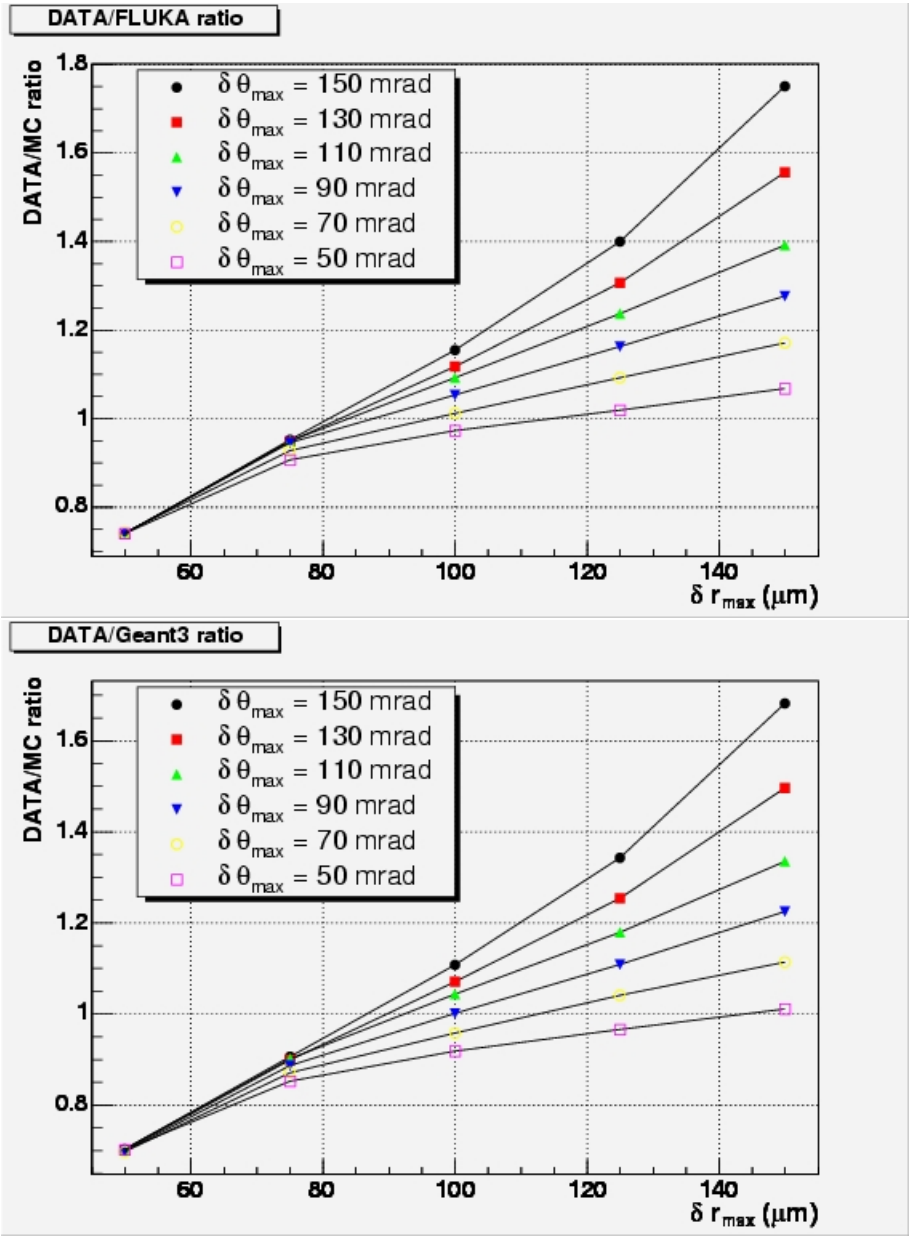

Figure 5.5: The ratio of the number of propagated base-tracks in the real data and in the Monte Carlo as a function of δr_{max}. Different curves correspond to different values of $\delta\theta_{max}$. The figures refer to 3 GeV electrons.

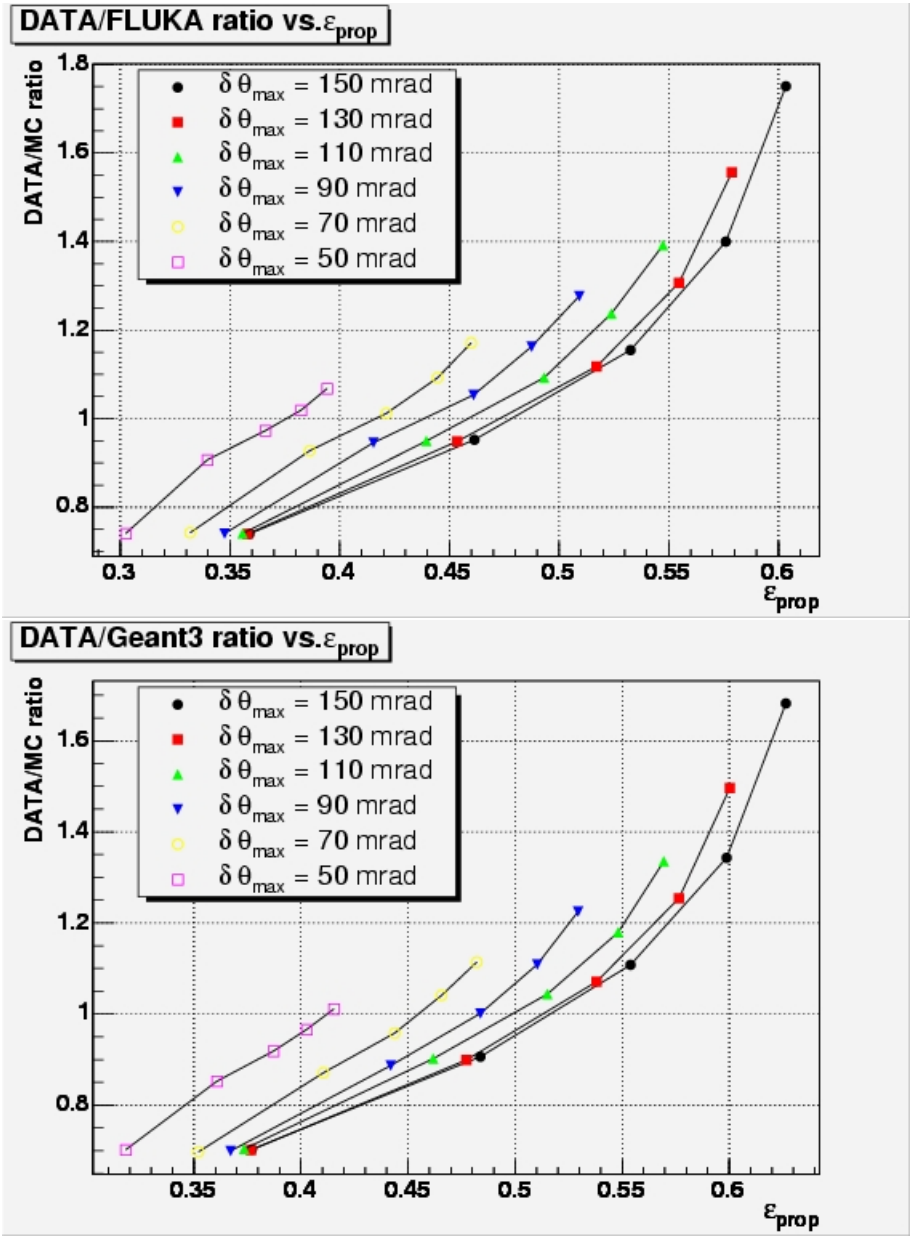

Figure 5.6: The ratio of the number of propagated base-tracks in the real data and in the Monte Carlo as a function of ε_{prop}. Different curves correspond to different values of $\delta\theta_{max}$. The figures refer to 3 GeV electrons.

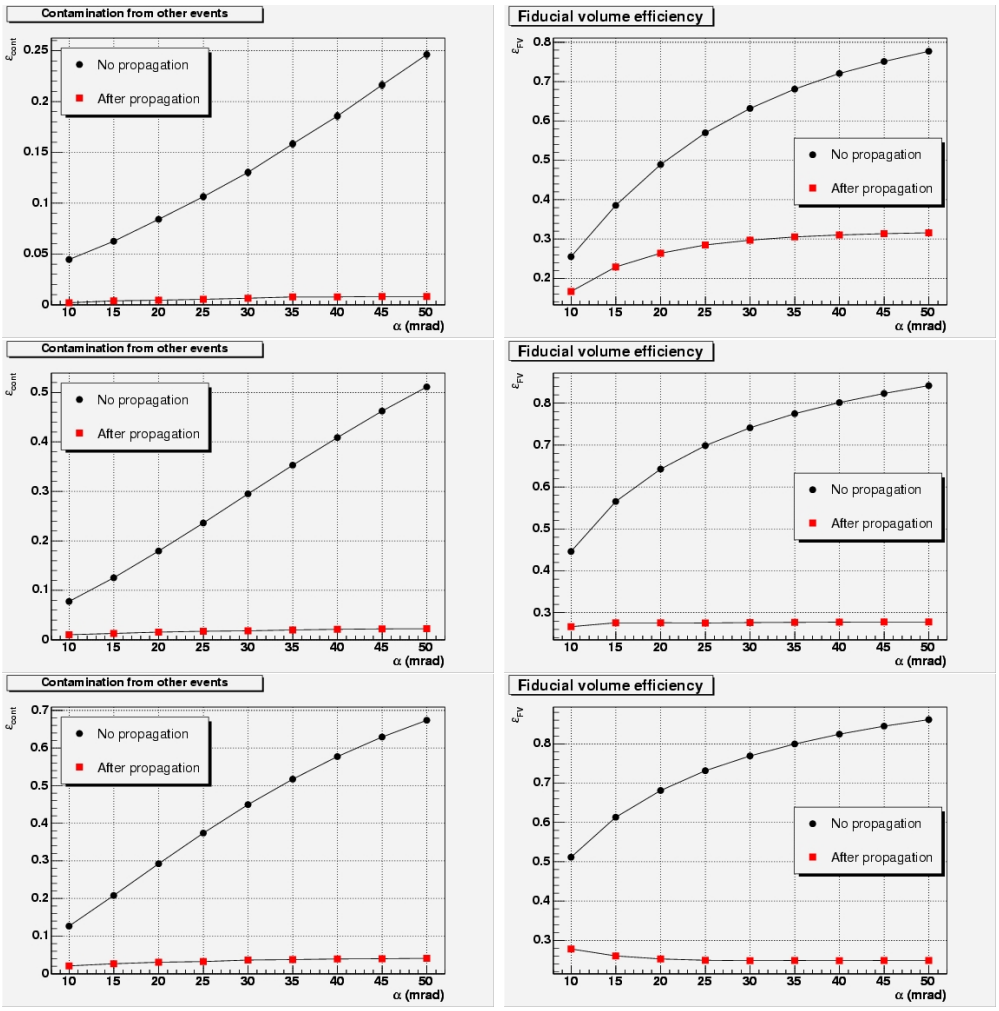

Figure 5.7: Monte Carlo simulation. On the left, base-tracks contamination coming from shower overlapping of different events. On the right, efficiency of the shower propagation algorithm versus the aperture of the cone. It is reported the total fraction of base-tracks integrated inside the cone and fraction of base-tracks surviving after the propagation algorithm. The top figures are for 1 GeV electrons, the central figures for 3 GeV electrons, the bottom figures for 6 GeV electrons.

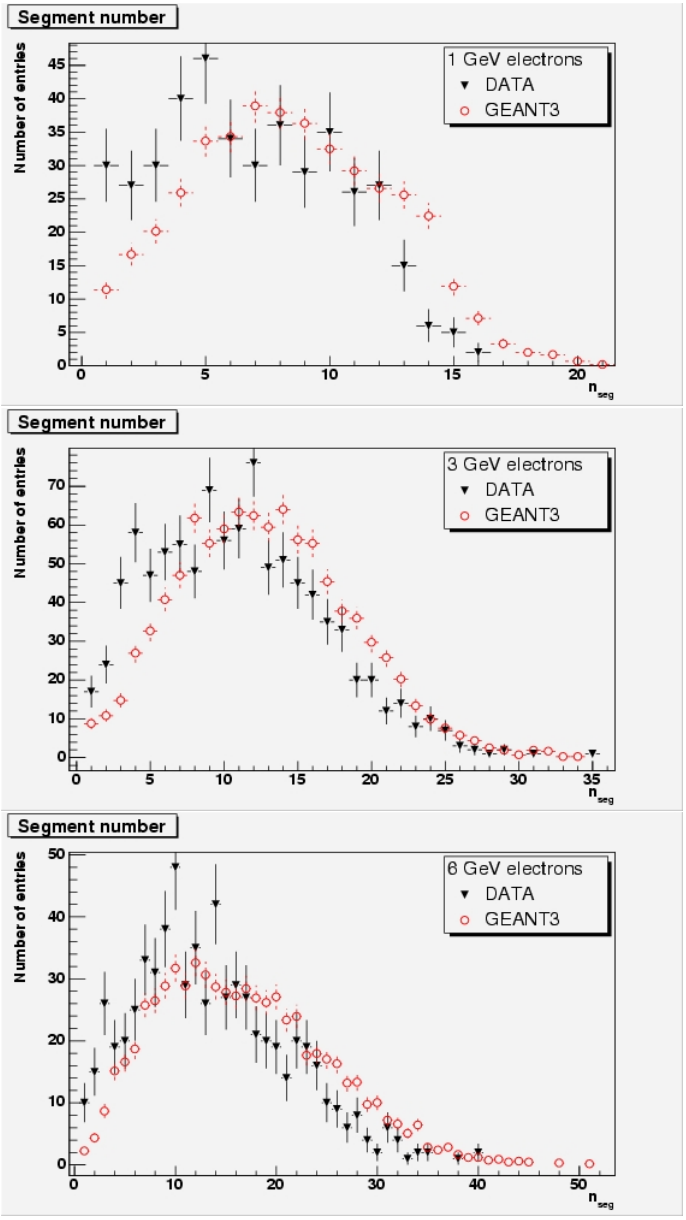

Figure 5.8: Distributions of the number of base-tracks integrated after shower propagation. A comparison with Monte Carlo simulation of the exposed brick is also given. The normalization is with respect to the experimental data.

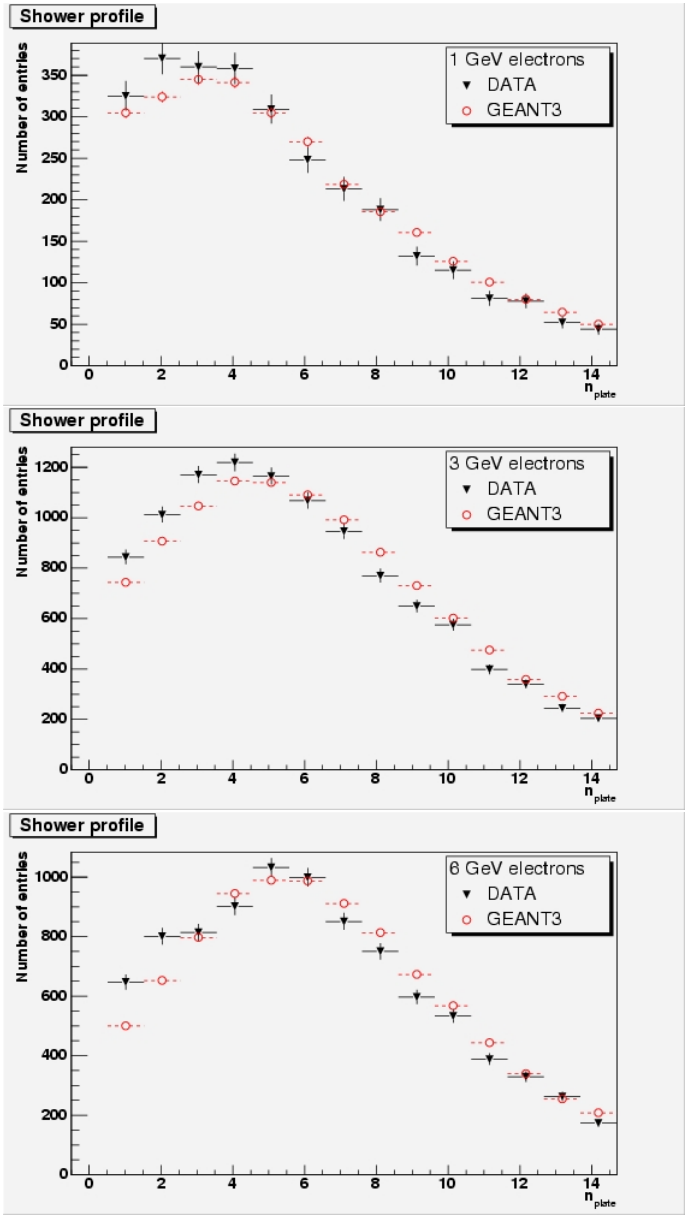

Figure 5.9: Longitudinal profile of the reconstructed shower after propagation. The average base-track number in each sheet is given. A comparison with Monte Carlo simulation of the exposed brick is also given. The normalization is with respect to the experimental data.

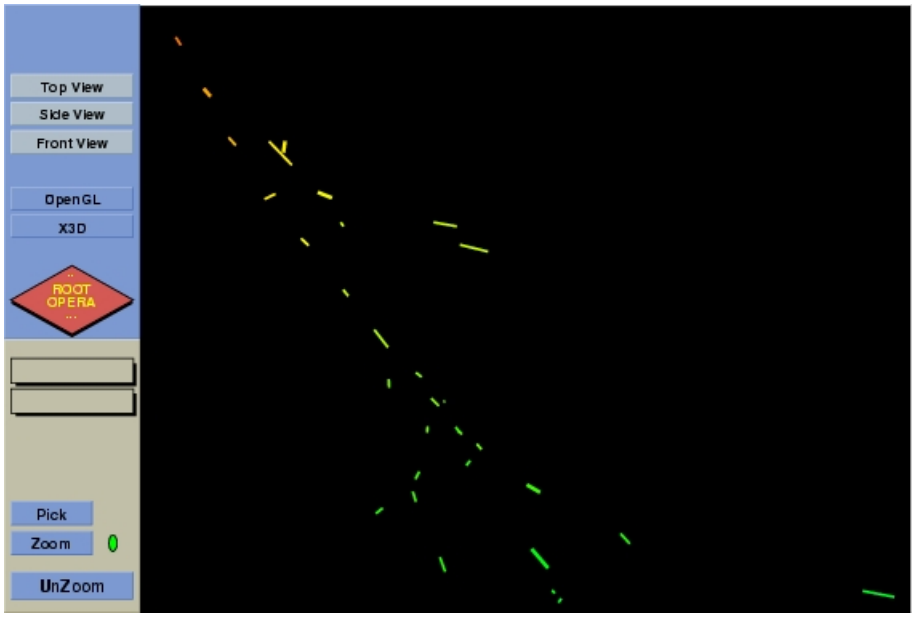

Figure 5.10: A reconstructed shower generated by a 6 GeV electron. The entrance point of the primary electron is the top left angle of the figure.

5.3 Artificial neural networks

A Neural Network is an interconnected group of neurons. The prime examples are biological neural networks, especially the human brain. In this work the term refers to artificial Neural Networks (NN) and this is the sense that is used in the rest of this work.

A NN is a mathematical or computational model for information processing based on a connectionist approach to computation. There is no precise agreed definition amongst researchers as to what a neural network is, but most would agree that it involves a network of relatively simple processing elements, where the global behavior is determined by the connections between the processing elements and element parameters. The original inspiration for the technique was from examination of bioelectrical networks in the brain formed by neurons and their synapses. In a neural network model, simple nodes (or "neurons", or "units") are connected together to form a network of nodes, hence the term "neural network".

NN are very popular paradigm in order to gain knowledge by examples [72] and they are very useful tool to separate distinct distributions in a multidimensional space, *e.g.* particle identification.

In contrast to classical methods, which usually reduce the multidimensional space to several variables, the NN approach can be applied to the raw distributions. The reduction of the configuration space might lead to a loss of important information which may otherwise help to separate the distributions. Thus, for the NN approach all the available information are used. A NN can be considered as a function, which transforms an information space (pattern space), into a discriminating variable space (feature space) by means of several transformation matrices connected in a non-linear way. The entries of the matrices are denoted as weights and serve as the free parameters of the function. These weights are adjusted in terms of a least square minimization of an error function.

In the present thesis the "multi-layered feed-forward" NN's are considered. They consist of neurons arranged in contiguous layers, as shown in Fig. 5.11. Each neuron $k\,(k = 1, ..., N_h)$ belonging to the hidden layer receives as input the output $X_l\,(l = 1, ..., N_i)$ of all the neurons of the input layer, to which it is connected by $w_{lk}^{(1)}$ synaptic weights. On the other hand, the neuron k is also connected, with the weight $w_{lk}^{(2)}$ to the neuron of the

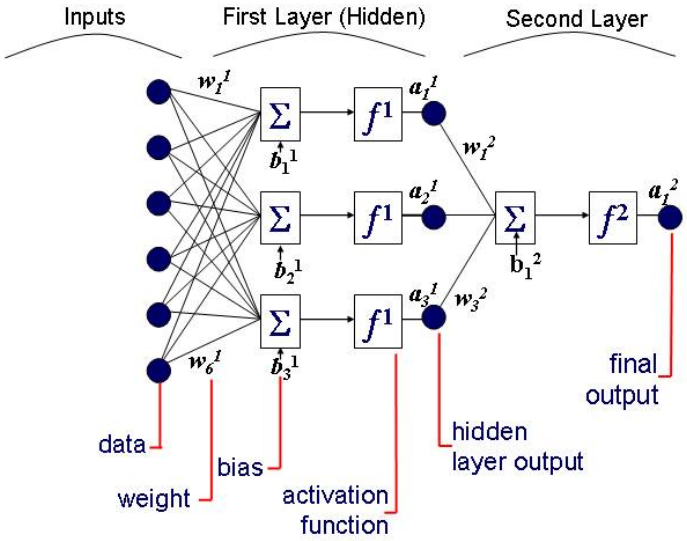

Figure 5.11: Example of Artificial Neural Network multilayer perceptron architecture with one hidden layer.

output layer. The transfer function of the neurons is the sigmoid function

$$g(x,\theta) = \frac{1}{1+\exp -\beta(x-\theta)} \tag{5.2}$$

where θ and β are the neuron threshold and gain factor, respectively. From the data analysis point of view each input neuron is associated with a physical variable. Therefore NN's enable one to explore a multidimensional input space, by taking into account several complex information about the physical event.

The synaptic matrix $W^{(\mathrm{old})}$ is trained by showing to the NN a data set of examples (*training data set*) and updating the weights by minimizing an error function E. In this thesis we have used the following error function:

$$E = \frac{1}{2}\sum_{i=1}^{N}(t_i - o_i) \tag{5.3}$$

where t_i and o_i are respectively the teaching input and the NN output for the i-th event presented to the NN. It can be shown that E is minimized

when NN outputs are minimum, mean-squared, error estimates of Bayesian probabilities [73].

After each training epoch, the quality of the NN behavior is estimated by means of an independent data set (*validation data set*). The learning session is stopped when the error function E, evaluated on the validation test, reaches the lowest value. At this point, the NN generalizes best. If learning is not stopped, overtraining occurs and the performance of the NN on the whole data decreases, despite the fact that the error on the training data still gets smaller.

In conclusion, three different kinds of data sets have been used for the training and the test of the NN performances:

- *training data set* is used to train the NN: the error of this data set is minimized during training;
- *validation data set* is used to determine the performance of the NN on patterns that are not trained during learning;
- *test data set* for finally checking the overall performance of the NN.

In this work, we used the NN's implemented in the ROOT[2] frame-work, inspired from the MLPfit package [74]. The learning method used is the *Broyden, Fletcher, Goldfarb, Shanno* (BFGS) method, that implies the computation of a $n_{weight} \times n_{weight}$ matrix, very powerful (at least) for less than 300 weights [75].

5.4 Algorithm for electron identification

The variables used for the training of the NN are defined in Ref. [64]. They describe the longitudinal development of electromagnetic showers and are defined by the following formula

$$\Xi_i = \sqrt{\sum_{j=1}^{N} \left[(\theta_{x_j} - \theta_{x_0})^2 + (\theta_{y_j} - \theta_{y_0})^2 \right]} \tag{5.4}$$

where θ_{x_0} and θ_{x_j} are the base-track angles in the first and the j-th sheet, respectively and the sum runs over all the base-tracks belonging to

[2]http://root.cern.ch

the shower in the i-th sheet. These variables well describe the contributions both from the scattering of an electron, that is bigger than the scattering of a pion before the starting of the shower because of the energy loss, and from particles belonging to the electromagnetic cascade once the shower has started.

Ref. [64] is based on a Monte Carlo simulation and the electron identification algorithm proposed there takes into account all the tracks inside the cone, as described in the OPERA proposal [44]. Moreover, that study refers to electrons crossing at least 20 emulsion sheets. Finally, at that time no data were available, so no comparison with experimental data was performed.

The bricks exposed at DESY and analyzed in this thesis have 15 emulsion sheets, that corresponds to 3.3 X_0. So our NN is limited to have only 14 input variables. While low energy electrons generally stop in the brick, high energy electromagnetic showers are not fully contained in 3.3 X_0.

Fig. 5.12 shows the profile of the showers as described by the input variables, defined in Eq. 5.4: it is given a comparison between the available data and Monte Carlo. Even in this "critical" situation, the input variables are able to discriminate electrons and pions. For the 6 GeV pion exposure at low density, the agreement between data and Monte Carlo is poor, since the Monte Carlo simulation does not take into account, in this case, the real scanning efficiency.

Besides the input neurons, the used NN has one hidden layer with 10 neurons and one output neuron. The training is performed over 300 epochs. In Fig. 5.13 the error of the validation data set as a function of the training epoch is shown. Training was stopped when the error reached a plateau.

After training, the output of the NN has been evaluated on the whole data set (Fig. 5.14). As expected the NN output for the Monte Carlo electrons is close to 1, while that for Monte Carlo pions is close to 0.

In Fig. 5.15, on the top, we show the profile of the response of the NN as a function of the number of shower base-tracks, while on the bottom we show the profile of the response of the NN as a function of the energy. As expected, the NN has a better electron-pion separation capability at high energies. At low energy the performances are worst, while the discrimination on the basis of the number of base-tracks is not so critical. In the energy range used for the NN training, pions are usually passing-through. However some of them can interact in the lead and mimic an electron-like behavior.

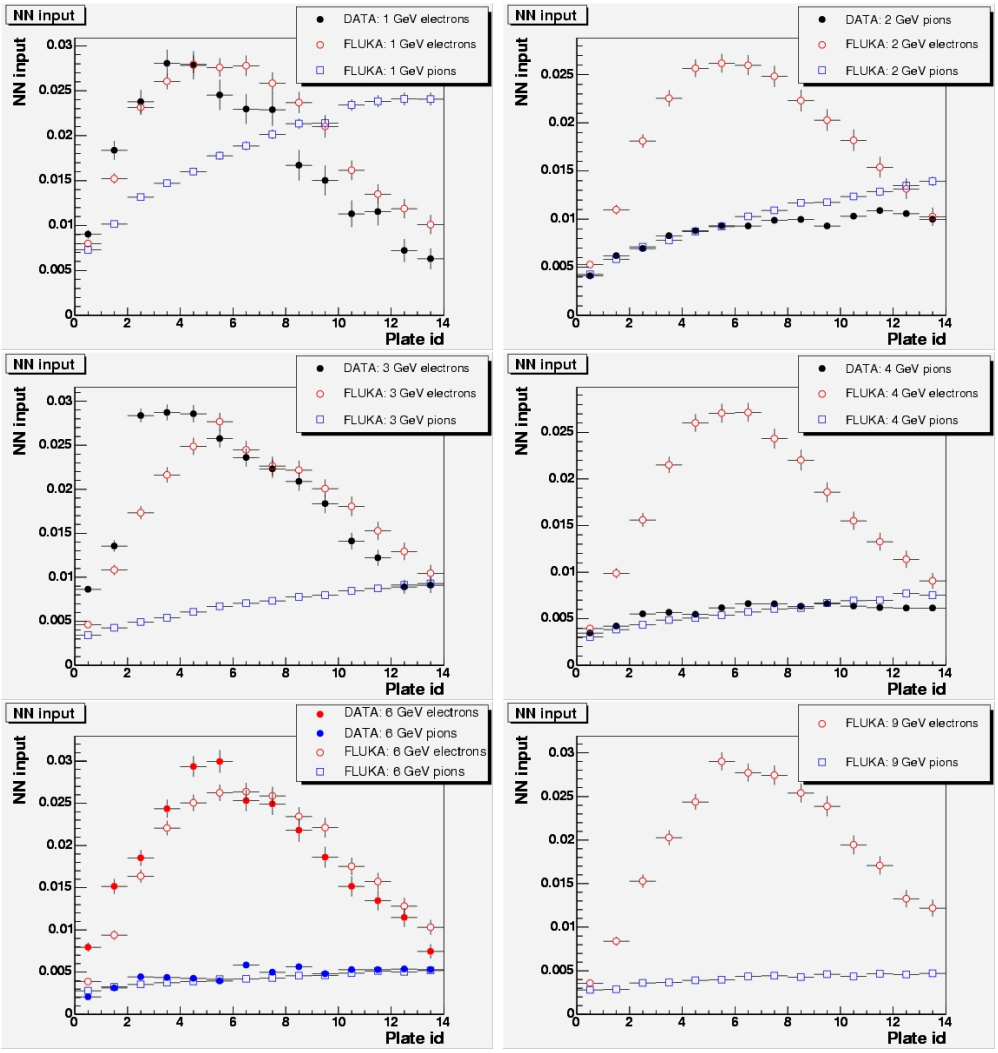

Figure 5.12: Longitudinal profiles of NN input variables as calculated by Monte Carlo at different energies. When available, a comparison with data is given. From left top, electron and pion with 1 GeV, 2 GeV, 3 GeV, 5 GeV and 9 GeV. Full circle are data, open marker are FLUKA Monte Carlo data.

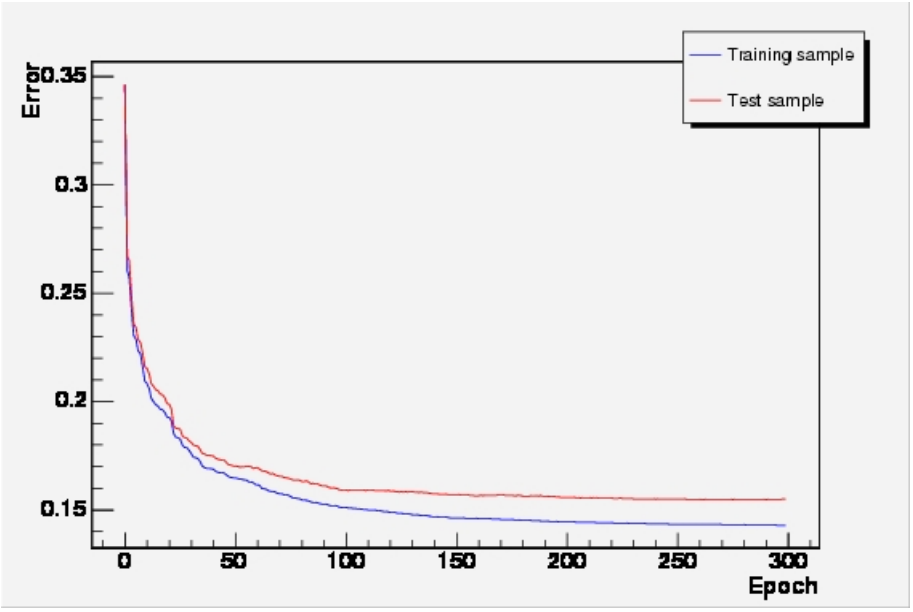

Figure 5.13: Monte Carlo data. The error of the training data set (blu curve) and of the validation data set (red curve) as a function of the training epoch.

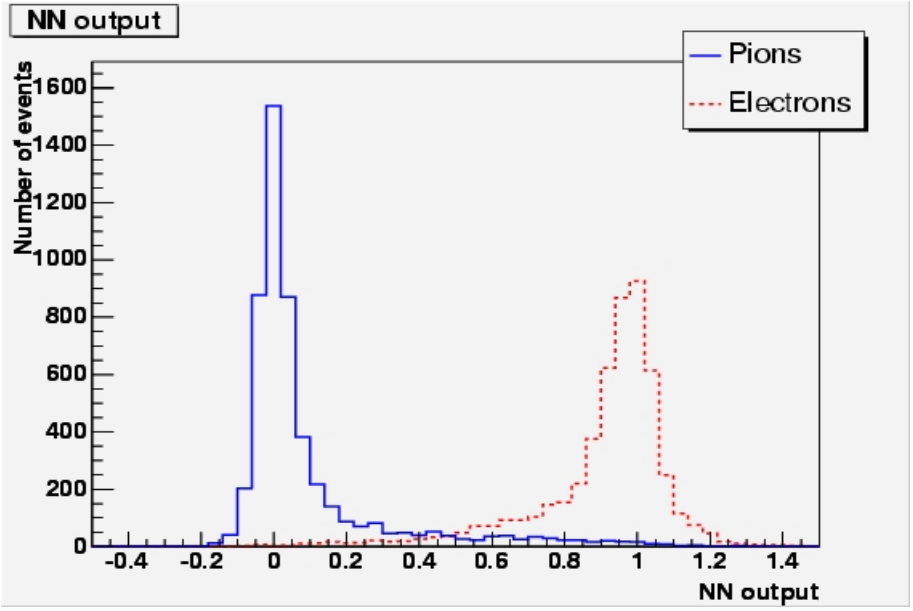

Figure 5.14: NN output on the Monte Carlo data set used during the training.

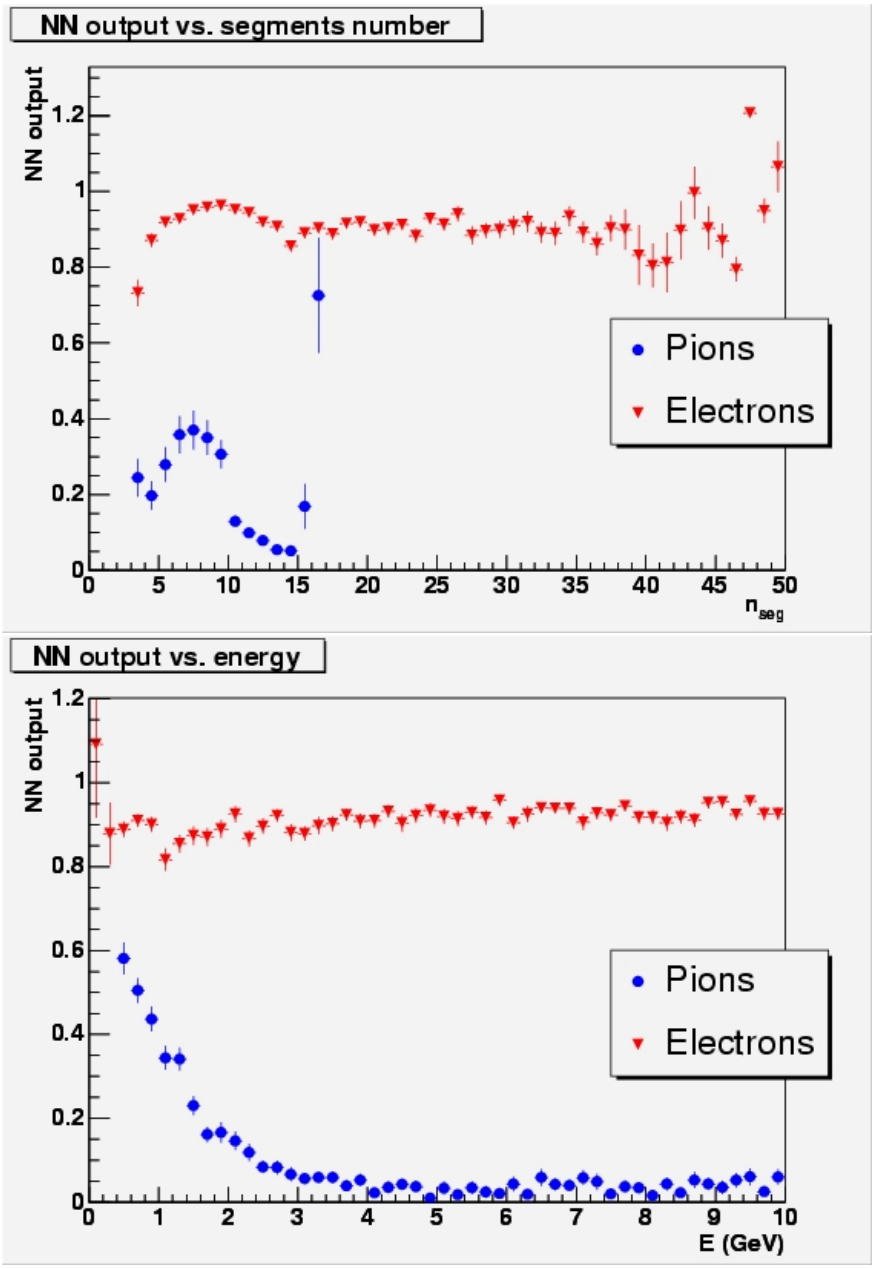

Figure 5.15: Monte Carlo data. NN output as a function of the number of reconstructed base-tracks in the shower (top). NN output as a function of the seed energy (bottom).

5.5 Results

A good algorithm for electron-pion identification must provide both a high probability to correctly identify a particle and a small mis-identification probability. Therefore, we had chosen a cut ζ to separate the two distributions, keeping the mis-identification probability as low as possible. At this point, some definitions are useful. The efficiency to correctly identify an electron is defined as

$$\varepsilon_{e\to e} \equiv \frac{n_{e\to e}}{N} \tag{5.5}$$

where $n_{e\to e}$ denotes the number of events above the cut ζ, correctly identified as electron, and N is the normalization factor, that includes all particles that have been propagated at least 1 base-track, besides the seed.

The probability of electron mis-identification is given by

$$\eta_{e\to\pi} \equiv \frac{n_{e\to\pi}}{N} \tag{5.6}$$

and the fraction of "not classified" (NC) particles is defined as

$$\varepsilon_{NC} \equiv \frac{n_{NC}}{N} \equiv 1 - \varepsilon_{e\to e} - \eta_{e\to\pi} \tag{5.7}$$

where n_{NC} is the number of "not classified" electrons. A particle is "not classified" if it has only 1 or 2 base-tracks besides the seed: for these particle the available information is too small and the NN is not able to distinguish between an electron or a pion.

The purity of the set identified as electrons is defined as

$$P_e \equiv \frac{\varepsilon_{e\to e}}{\varepsilon_{e\to e} + \eta_{\pi\to e}} \tag{5.8}$$

Analogous formulas are for pions.

The efficiency of electron identification versus the purity is given on the left of Fig. 5.16. To optimize the cut ζ, we defined a quality factor Q to be maximized

$$Q \equiv \varepsilon_{e\to e} \times \varepsilon_{\pi\to\pi} \tag{5.9}$$

In the right part of Fig. 5.16 is show the quality factor Q as a function of ζ. The maximization of the functional Q gives $\zeta = 0.50$.

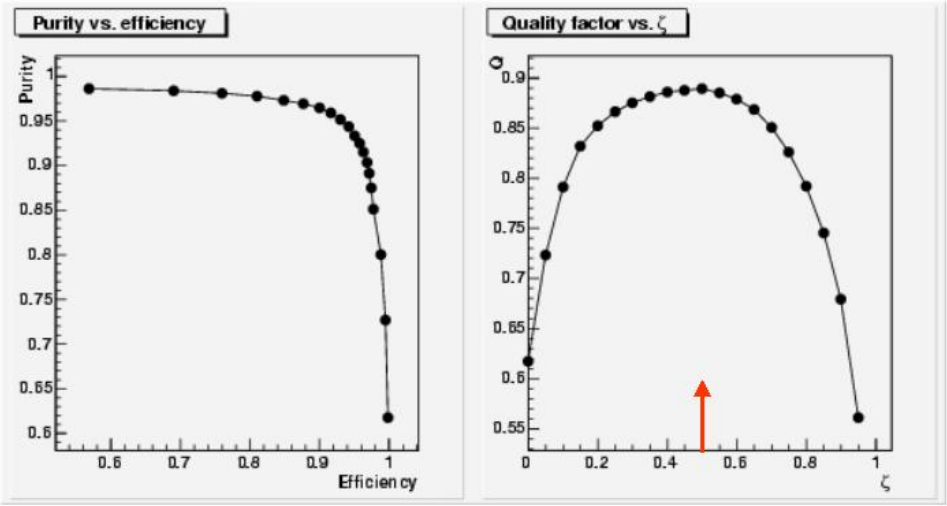

Figure 5.16: Monte Carlo data. Electron purity calculated on the validation data set versus the electron identification probability (left). Quality factor Q as a function of the cut ζ (right). The arrow indicates the cut used to separate the pion-electron distributions.

Once the NN has been trained and tested, electron and pion identification efficiencies have been computed for simulated monochromatic beams. The results are shown in Fig. 5.17. More details are given in Tab. 5.1 and Tab. 5.2, where, besides the identification and mis-identification probabilities, also the normalization and the fraction of "not classified" events are given.

The algorithm has been applied to experimental electron data. Available data are from the scanning of the brick 1, 2 and 4 in Tab. 4.5. We used Monte Carlo simulations in order to correctly take into account background tracks in the signal region (see Fig. 4.13 and 5.8). The particles with less than 4 base-tracks besides the seed have been assigned a correct weight in the normalization factor.The results for electrons are given in Tab. 5.3 and are in good agreement with the simulation.

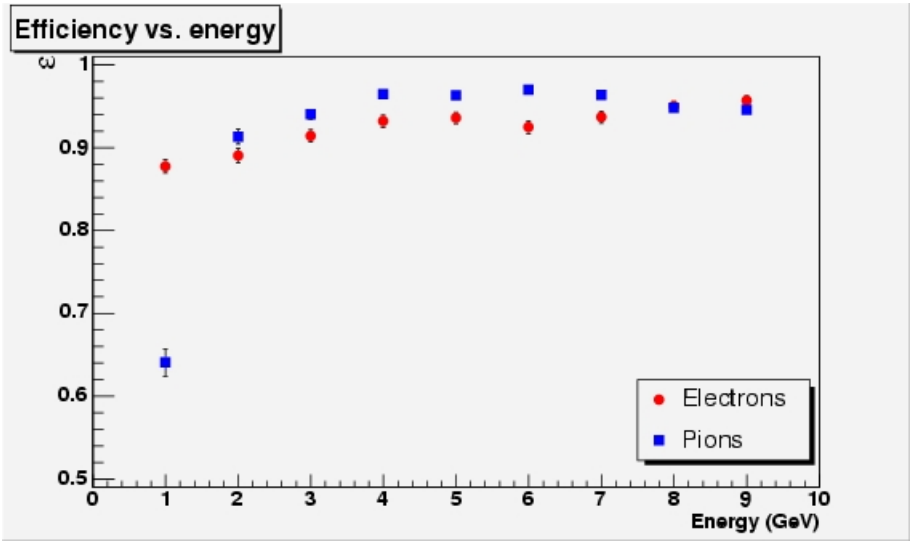

Figure 5.17: Electron and pion identification probabilities for different energies as obtained with the FLUKA Monte Carlo data. The difference between FLUKA and GEANT3 are within few percent (see Tab. 5.1 and 5.2).

Finally, real pion data have been used from two experimental tests performed at the CERN PS in June 2003 [2] and August 2004, where some OPERA brick where exposed to an almost pure and monochromatic pion beam. The beam electron contamination is negligible and the momentum resolution is about 1%. A summary of these exposures is given in Tab. 5.4. Within 400 mrad in both the angular projections and with the usual cut in the (χ, n_c) plane (see Eq. 3.5), the number of estimated background base-tracks is $\sim$6 base-tracks/mm^2 and is approximately the same for all the brick.

Since the NN has 14 input neurons, in the following analysis only the 15 most upstream emulsion sheet have been considered. The main difference is due to the increased fraction of mis-identified pions. This can be explained in the following way. For the high density exposures (brick 1, 2 and 3 in Tab. 5.4), the accordance is poor since the density of primary pions impinging the brick is of the order of 20 base-tracks/cm^2, very high for a shower analysis. Moreover, the average base-track reconstruction efficiency in the scanned emulsion sheets is lower than the one used in the Monte Carlo simulation ($\sim$75%). On the other hand, results for low density exposure (brick 4 in Tab. 5.4) are even worst since, in this case, scanning efficiency are higher

E	FLUKA				GEANT3			
(GeV)	N	$\varepsilon_{e\to e}$	$\eta_{e\to\pi}$	ε_{NC}	N	$\varepsilon_{e\to e}$	$\eta_{e\to\pi}$	ε_{NC}
1	857	0.88	0.05	0.08	854	0.88	0.06	0.06
2	875	0.89	0.07	0.04	865	0.89	0.08	0.03
3	863	0.91	0.05	0.04	855	0.93	0.05	0.03
4	868	0.93	0.04	0.02	868	0.91	0.06	0.03
5	873	0.94	0.04	0.03	873	0.96	0.03	0.01
6	877	0.92	0.05	0.02	882	0.96	0.04	0.01
7	871	0.94	0.04	0.02	871	0.94	0.04	0.01
8	880	0.95	0.04	0.01	875	0.95	0.04	0.02
9	879	0.96	0.03	0.01	881	0.97	0.03	0.00

Table 5.1: Electron identification and mis-identification probabilities for GEANT3 and FLUKA. N is the normalization factor. NC stands for "Not Classified" (refer to text for details).

	FLUKA				GEANT3			
E (GeV)	N	$\varepsilon_{\pi\to\pi}$	$\eta_{\pi\to e}$	ε_{NC}	N	$\varepsilon_{\pi\to\pi}$	$\eta_{\pi\to e}$	ε_{NC}
1	871	0.64	0.33	0.03	884	0.65	0.32	0.03
2	854	0.91	0.07	0.02	856	0.91	0.08	0.01
3	872	0.94	0.03	0.03	871	0.96	0.02	0.02
4	852	0.96	0.02	0.02	871	0.98	0.01	0.01
5	862	0.96	0.02	0.02	881	0.97	0.02	0.01
6	863	0.97	0.01	0.02	880	0.96	0.02	0.01
7	874	0.96	0.01	0.03	876	0.96	0.02	0.02
8	870	0.95	0.02	0.03	880	0.97	0.02	0.01
9	868	0.95	0.03	0.03	864	0.96	0.03	0.01

Table 5.2: Pion identification and mis-identification probabilities for GEANT3 and FLUKA. N is the normalization factor. NC stands for "Not Classified" (refer to text for details).

E (GeV)	N	$\varepsilon_{e\to e}$	$\eta_{e\to\pi}$	ε_{NC}
1	422	0.86	0.07	0.08
3	965	0.92	0.06	0.02
6	666	0.95	0.04	0.01

Table 5.3: Electron identification efficiency for experimental data.

Brick	E (GeV)	Emulsion sheets per brick	Density (pions/mm^2)
1	4	56	20
2	6	56	20
3	2	56	20
4	6	50	0.05

Table 5.4: Summary of the bricks exposed in the experimental test at the CERN PS. The tables gives the pion beam energy, the pion density and the number of emulsion sheets for each brick.

E (GeV)	N	$\varepsilon_{\pi\to\pi}$	$\eta_{\pi\to e}$	ε_{NC}
2	1520	0.75	0.20	0.06
4	1697	0.85	0.08	0.07
6 (HD)	1951	0.80	0.07	0.13
6 (LD)	118	0.75	0.14	0.12

Table 5.5: Pion identification efficiency for experimental data. HD stands for "High Density", LD "Low Density".

than the ones used in this work ($\sim$95%). A summary of the results for the pions is given in Tab. 5.5.

Conclusions

The OPERA experiment, in preparation at the Gran Sasso Underground Laboratory, aims at the confirmation of the $\nu_\mu \rightarrow \nu_\tau$ oscillation hypothesis through the *direct* observation of τ neutrinos in the CNGS initially pure ν_μ beam.

Taking into account the detection efficiency, the expected number of tau interactions in five years of data taking is $\sim$16 at $\Delta m^2 = 2.5 \times 10^{-3}$ eV^2 and with CNGS beam upgrade ($\times$1.5). To claim a final confirmation of $\nu_\mu \rightarrow \nu_\tau$ oscillations is necessary to keep the background as low as possible, to have a good particle identification and to reduce as much as possible the mis-identification probability.

The OPERA physics program will be completed by the $\nu_\mu \rightarrow \nu_e$ oscillation search, looking for an excess of ν_eCC interactions.

OPERA will use large scale *hybrid* apparatus divided in two supermodules, each equipped with electronic detectors, an iron spectrometer and a highly segmented 0.9 kton target section made of "Emulsion Cloud Chamber". The production and the decay of τ leptons will be observed thanks to the excellent position resolution of nuclear emulsions, which, at present, provides the highest spatial resolution.

In order to analyze the required amount of emulsions, an R&D project has been carried out within the OPERA collaboration to develop automatic scanning systems having the required accuracy and scanning speed.

The automatic scanning system presently working in the Bologna laboratory reached the requested scanning speed of 20 cm^2/h with a base-tracks reconstruction efficiency of $\sim$90% for minimum ionizing particles up to 500 mrad.

We measured some OPERA bricks exposed to a pure electron beam at DESY in order to study the development of electromagnetic showers and provide a measurement of the electron identification efficiency.

In the OPERA proposal, a method to identify electrons based on a shower analysis is described. An electron is identified by counting all segments inside a cone with the axis coincident with the direction of the primary track. This analysis requires a low density of background tracks and no shower overlapping, as will be the case in the real OPERA.

However, the bricks analyzed in this work integrated many cosmic ray tracks before and after the exposure and the estimated background tracks is $\sim$35 tracks/mm^2. Moreover, since the density of the electrons impinging on the brick is $\sim$100 electrons/cm^2, we had to consider also the overlapping between different showers.

A dedicated shower reconstruction algorithm has been implemented to collect as many tracks related to the shower as possible while keeping the background track density at a low level. The shower reconstruction algorithm has been developed using Monte Carlo simulation and an iterative comparison with experimental data.

An electron-pion separator based on a Neural Network was implemented. Both the Neural Network training and testing stages were performed with Monte Carlo. We obtained identification efficiencies larger than 90% both for electrons and pions with energy higher that 2 GeV.

The algorithm and the Neural Network separator have been applied to the electrons data of 1, 3 and 6 GeV bricks exposed at DESY. Electron identification efficiencies are 86%, 92% and 95%, respectively, in good agreement with Monte Carlo results.

We also applied this analysis to pions data from two experimental tests performed at the CERN PS. In this case, the data-Monte Carlo agreement is poor since the segment reconstruction efficiency in the scanned emulsion sheets is different from the one used in the Monte Carlo simulation and in the Neural Network training stage.

The results obtained in this work cannot be considered, *per se*, satisfying the OPERA requirements. The mis-identification probability has to be kept at the few percent level, as demanded by the $\nu_\mu \to \nu_\tau$ and the $\nu_\mu \to \nu_e$ oscillation studies. However, the good agreement between electron data and Monte Carlo simulation makes us confident to rely on the Monte Carlo simulation to extrapolate the results in an OPERA-like environment.

Bibliography

[1] K. Kodama *et al.*, Rev. Sci. Instrum. **74** (2003) 53.

[2] M. Cozzi, *Study of pion identification in the Emulsion Cloud Chambers of the OPERA experiment*, Ph.D. Thesis, University of Bologna (2005).

[3] W. Pauli, *Aufsatze und Vortrage uber Physik und Erkenntnistheorie*, ed. W. Westphal, Braunschweig (1961).

[4] F. Reines and C.L. Cowan, Nature **178** (1956) 446.

[5] G. Danby *et al.*, Phys. Rew. Lett. **9** (1962) 36.

[6] K. Kodama *et al.*, Phys. Lett. **B504** (2001) 218.

[7] G. Abbiendi et al., Eur. Phys. J. **C18** (2000) 253.

[8] http://lepewwg.web.cern.ch/LEPEWWG.

[9] C. Kraus *et al.*, hep-ex/0412056 (2004).

[10] K. Assamagan *et al.*, Phys. Rev. **D53** (1996) 6065.

[11] R. Barate *et al.*, Eur. Phys. J. **C2** (1998) 395.

[12] WMAP Collaboration, D. N. Spergel *et al.*, Astrophys. J. Suppl. **148** (2003) 175.

[13] S. Bilenky and S. Petcov, Rev. Mod. Phys. **59** (1987) 671 [Erratumibid. **61** (1987), 169]; B. Kayser, *Neutrino Mass*, eds. G. Altarelli and K. Winter, Springer Tracts in Modern Physics (2003).

[14] H. V. Klapdor-Kleingrothaus *et al.*, Eur. Phys. J. **A12** (2001) 147.

[15] H. V. Klapdor-Kleingrothaus, *et al.*, Mod. Phys. Lett. **A16** (2001) 2409.

[16] V. D. Barger *et al.*, Phys. Rev. Lett. **82** (1999) 2640; Phys. Lett. **B462** (1999) 109.
S. Cecchini *et al.*, Astropart. Phys. **21** (2004) 183.

[17] Y. Grossman and M. P. Worah, hep-ph/9807511 (1998).
E. Lisi, A. Marrone, and D. Montanino, Phys. Rev. Lett. **85** (2000) 1166.

[18] G. Battistoni *et al.*, hep-ex/0503015 (2005).
S. L. Glashow, hep-ph/0407087 (2004).

[19] B. Pontecorvo, Zh. Eksp. Teor. Fiz. **33** (1957) 549; B. Pontecorvo, Zh. Eksp. Teor. Fiz. **34** (1958) 247.

[20] Z. Maki *et al.*, Prog. Theor. Phys. **28** (1962) 870.

[21] R. Barbieri and A. Dolgov, Nucl. Phys. **B349** (1991) 743.

[22] L. Wolfenstein, Phys. Rev. **D17** (1978) 2369.

[23] S. Mikheyev and A. Smirnov, Yad. Fiz. **42** (1985) 1441 [Sov. J. Nucl. Phys. **42** (1986) 913]; Zh. Eksp. Teor. Fiz. **91** (1986) 7 [Sov. Phys. JETP **64** (1986) 4]; Nuovo Cimento **C9** (1986) 17.

[24] CHOOZ Collaboration, M. Apollonio *et al.*, Phys. Lett. **B420** (1998) 397; M. Apollonio *et al.*, Eur. Phys. J. **C27** (2003) 331.

[25] Palo Verde Collaboration, F. Boehm *et al.*, Phys. Rev. Lett. **84** (2000) 3764; F. Boehm *et al.*, Phys. Rev. **D64** (2001) 112001.

[26] J. N. Bahcall *et al.*, Astrophys. J. **555** (2001) 990.

[27] J. N. Bahcall'homepage, http://www.sns.ias.edu/∼jnb.

[28] R. Davis, Prog. Part. Nucl. Phys. **32** (1994) 13.

[29] Gallex Collaboration, W. Hampel *at al.*, Phys. Lett. **B447** (1999) 127.
GNO Collaboration, M. Altmann *at al.*, Phys. Lett. **B490** (2000) 16.
SAGE Collaboration, J. N. Abdurashitov *at al.*, Phys. Rev. Lett. **83** (1999) 4686.

[30] J. N. Bahcall, SLAC Beam Line **31**(1) (2001) 2.

[31] S. Basu *at al.*, Mon. Not. R. Astron. Soc. **292** (1997) 1402.

[32] Kamiokande Collaboration, Y. Fukuda *et al.*, Phys. Rev. Lett. **77** (1996) 1683.

[33] Super-Kamiokande Collaboration, S. Fukuda *et al.*, Phys. Rev. Lett. **86** (2001) 5651.

[34] SNO Collaboration, S. Ahmed *et al.*, Phys. Rev. Lett. **92** (2004) 181301.

[35] KamLAND Collaboration, K. Eguchi *et al.*, Phys. Rev. Lett. **90** (2003) 021802; T. Araki *et al.*, Phys. Rev. Lett. **94** (2005) 081801.

[36] The MACRO Collaboration, M. Ambrosio *et al.*, Phys. Lett. B **434** (1998) 451; M. Ambrosio *et al.*, Eur. Phys. J. **C36** (2004) 323.

[37] Super-Kamiokande Collaboration, Y. Fukuda *et al.*, Phys. Rev. Lett. **81** (1998) 1562; Y. Ashie *et al.*), hep-ex/0501064 (2005) (Submitted to Phys. Rev. **D**).

[38] Soudan 2 Collaboration, W.W. Allison *et al.*, Phys. Lett. **B449** (1999) 137; M. Sanchez *et al.*, Phys. Rev. **D68** (2003) 11304.

[39] T.K. Gaisser, M. Honda, Ann. Rev. Nucl. Part. Sci. **153** (2002) 52.

[40] V. Agrawal *et al.*, Phys. Rev. **D53** (1996) 1314.
M. Honda *et al.*, Phys. Rev. **D52** (1995) 4985.

[41] M. Honda *et al.*, Phys. Rev. **D70** (2004) 043008.
G. Battistoni *et al.*, Astrophys. Phys. **19** (2003) 269.

[42] Super-Kamiokande Collaboration, S. Fukuda *et al.*, Phys. Rev. Lett. **85** (2000) 3999.
MACRO Collaboration, M. Ambrosio *et al.*, Phys. Lett. **B517** (2001) 59.

[43] K2K Collaboration, S. H. Ahn *et al.*, Phys. Lett. **B511** (2001) 178; E. Aliu *et al.*, Phys. Rev. Lett. **94** (2005) 081802.

[44] OPERA Collaboration, *OPERA: An appearance experiment to search for $\nu_\mu \leftrightarrow \nu_\tau$ oscillations in the CNGS beam*, Experimental proposal, CERN-SPSC-2000-028 (2000); *Status report on the OPERA experiment*, CERN/SPSC 2001-025 (2001); http://operaweb.web.cern.ch/operaweb/documents/index.shtml.

[45] G. Acquistapace *et al.*, CERN 98-02, AE-98/05, (1998); http://proj-cngs.web.cern.ch/proj-cngs.

[46] M. Komatsu, P. Migliozzi and F. Terranova, *Sensitivity to θ_{13} of the CERN to Gran Sasso neutrino beam*, J. Phys. G **29** (2003) 443.

[47] A. Ferrari, A. Guglielmi and P. R. Sala, *CNGS neutrino beam systematics for θ_{13}*, hep-ph/0501283 (2004).

[48] E. Barbuto *et al.*, Nucl. Instr. Meth. **A525** (2004) 485.

[49] S. Eidelman *et al.*, Phys. Lett. **B592** (2004).

[50] B. Van de Vyver and P. Zucchelli, Nucl. Instr. Meth. **A385** (1997) 91.

[51] M. C. Gonzalez-Garcia and J.J. Gomez-Cadenas, Phys. Rew. **D55** (1997) 1297.

[52] M. Blau, Nature **142** (1938) 613.

[53] C. Lattes, H. Muirhead, G. Occhialini, C. Powell, *Process involving charged mesons*, Nature **159** (1947) 694.

[54] D. Allasia *et al.*, Nucl. Phys. **B176** (1980) 13.

[55] N. Ushida *et al.*, Nucl. Instr. Meth. **224** (1984) 50.

[56] S. Aoki *et al.*, Nucl. Instr. Meth. **A274** (1989) 64.

[57] CHORUS Collaboration, E. Eskut *et al.*, Nucl. Instr. and Meth. **A401** (1997) 7.

[58] S. Aoki *et al.*, Nucl. Instr. and Meth. **B51** (1990) 466.

[59] T. Nakano, Ph.D. thesis, Nagoya University, Nagoya, Japan, (1997).

[60] N. D'Ambrosio, Nucl. Instr. Meth. **A477** (2002) 431; N. DAmbrosio, Nucl. Instr. and Meth. **A525** (2004) 193; G. Sirri, *Automatic scanning of emulsion films for the OPERA experiment*, Degree Thesis, University of Bologna (2005).

[61] G. Rosa *et al.*, Nucl. Instr. and Meth. **A394** (1997) 357; C. Bozza, *Analysis of results in Nuclear Emulsion in CHORUS and OPERA Experiments*, Ph.D. Thesis, University of Salerno (2000).

[62] http://ntslab01.na.infn.it/fedra.

[63] C. K. Chui and and G. Chen, *Kalman Filtering: With Real-Time Applications*, 2nd ed., Springer-Verlag, Berlin (1991).

[64] L.S.Esposito, *Ricerca di oscillazioni $\nu_\mu \rightarrow \nu_\tau$ nell'esperimento OPERA nel canale $\tau \rightarrow e$: sviluppo di un algoritmo per l'identificazione e la misura dell'energia di sciami elettromagnetici*, Degree Thesis, University Federico II, Napoli (2005), available at http://www.infn.it/thesis.

[65] B. Rossi, *High energy particles*, Prentice Hall, New Jersey (1952).

[66] W.R. Nelson, T.M. Jenkins, R.C. McCall, and J.K. Cobb, Phys. Rev. **149** (1966) 201.

[67] G. Bathow *et al.*, Nucl. Phys. **B20** (1970) 592.

[68] D. Autiero *et al.*, *Characterization of the T24 electron beam-line available at DESY*, OPERA internal note, (2004).

[69] GEANT 3.21, CERN Program Library Long Writeup W5013.

[70] A. Fasso, A. Ferrari, P. R. Sala and J. Ranft, SLAC-REPRINT-2000-117; A. Fasso, A. Ferrari and P. Sala, SLAC-REPRINT-2000-116.

[71] http://people.na.infn.it/∼marotta/ORFEO.

[72] S. Haykin, *Neural networks - A comprehensive foundation*, Macmillan (1994).

[73] M.D. Richard and R.P. Lippmann, Neural Comput. **3** (1991) 461.

[74] http://schwind.home.cern.ch/schwind/MLPfit.html.

[75] D.F. Shanno, J. Opt. Theory Applic. **46** (1985) 87.